
Università
degli Studi
di Ferrara

**Dottorato di ricerca in Fisica, ciclo 34°**

**Coordinatrice: Prof.ssa Eleonora Luppi**

# Design, validation and future perspectives of a setup for *operando* DRIFT spectroscopy measurements on chemiresistive gas sensors

**Settore scientifico disciplinare: FIS/01**

**Tutor:**
**Prof. Vincenzo Guidi**

**Dottorando:**
**Michele Della Ciana**

**Co-tutor:**
**Prof. Vittorio Morandi**

Anni di corso 2018/2021

# Contents


**1 Chemiresistive gas sensor** **14**
- 1.1 Introduction . . . 14
- 1.2 Structure and fabrication . . . 15
  - 1.2.1 Substrate . . . 16
  - 1.2.2 Sensing film . . . 17
- 1.3 Theory and Sensing properties . . . 17
  - 1.3.1 Working principle . . . 18
  - 1.3.2 Sensing properties . . . 23

**2 Infrared Spectroscopy** **27**
- 2.1 Introduction . . . 27
- 2.2 Theory background . . . 28
  - 2.2.1 Infrared Radiation . . . 28
  - 2.2.2 Interaction of infrared radiation with matter . . . 29
  - 2.2.3 Interpretation of the absorption spectrum . . . 32
- 2.3 Instrumentation . . . 34
  - 2.3.1 Fourier-transform spectroscopy . . . 34
  - 2.3.2 Fourier transform infrared spectroscopy (FTIR) setup . . . 38

**3 Design of the *operando* DRIFT setup** **45**
- 3.1 Introduction . . . 45
- 3.2 Logical Design . . . 46
- 3.3 FTIR and DRIFT setup . . . 47
- 3.4 Mechanical design of the measuring chamber . . . 48
  - 3.4.1 Fluid dynamics analysis . . . 50
- 3.5 Gas delivery system . . . 50
- 3.6 Electronics design . . . 51
  - 3.6.1 Introduction . . . 51
  - 3.6.2 Hardware . . . 53
  - 3.6.3 Software implementation . . . 59
  - 3.6.4 Implemented measurements . . . 65

3.6.5 Validation of the electronics . . . 68
3.6.6 Comparison with standard instrumentation . . . 74
3.6.7 Conclusions . . . 78
3.7 Measuring protocol . . . 79
3.7.1 Focus alignment assisted by the heater . . . 79
3.7.2 Compensation of the MCT detector with respect to the sensor temperature . . . 79
3.7.3 Background and spectra processing . . . 81
3.8 Validation of the setup . . . 83
3.8.1 Fluid dynamic and residence time distribution . . . 83
3.8.2 Temperature gradient measurements . . . 85
3.8.3 Operando DRIFT experiment . . . 86
3.9 Conclusions . . . 88

**4 $SO_2$ sensing mechanism of nanostructured $SiC - SiOC$ core shell: an *operando* DRIFT investigation 90**
4.1 Introduction . . . 90
4.2 Materials and Methods . . . 92
4.2.1 Preparation and characterization of silicon carbide nanoparticles . 92
4.2.2 Sensor manufacturing . . . 92
4.2.3 Electrical characterization of chemiresistive gas sensors . . . 94
4.2.4 *Operando* DRIFT characterization setup . . . 95
4.3 Results . . . 97
4.3.1 SiC-nps morphology and composition . . . 97
4.3.2 *In situ* oxidation of SiC-nps . . . 97
4.3.3 Electrical properties: I-V and I-T characteristics . . . 100
4.3.4 Electrical response to $SO_2$ in a dry and wet environment . . . 103
4.4 Proposed sensing mechanism . . . 106
4.4.1 Conduction in dry condition . . . 106
4.4.2 Conduction in wet conditions . . . 107
4.5 Conclusions . . . 110

**Appendix A 3D printing 115**
A.1 Fused deposition modeling: filament 3D printer . . . 115
A.2 Stereolithography (SLA): resin 3D printer . . . 117
A.3 Conclusion . . . 118

**Appendix B In operando DRIFT setup extensions 119**
B.1 Setup for*operando* photoactivated measurements . . . 120
B.1.1 Mechanical design . . . 120

B.1.2 Control system . . . . . 122
B.2 Heater design for DRIFT measurements on heated powders . . . . . 123
B.2.1 Mechanical design . . . . . 123
B.3 Conclusion . . . . . 124

**Appendix C Mechanical drawings** **125**

# Abstract

## Italian version

In questa tesi di dottorato é presentato lo sviluppo di un sistema *operando* per la caratterizzazione di sensori di gas chemiresistivi utilizzando spettroscopia di luce infrarossa (IR) diffusa (DRIFT). L'attivitá di ricerca é stata focalizzata sullo sviluppo parallelo della camera test da implementare nello spettrometro e dell'elettronica associata per l'acquisizione e l'elaborazione dei segnali. La camera di misura é stata progettata per essere compatibile con lo spettrometro a trasformata di Fourier IR Vertex V70 *(Bruker)* dotato di accessorio DRIFT Praying Mantis *(Harrick Scientific)*. Per il *design* meccanico della camera test si é fatto utilizzo sia delle tecnologie di stampa 3D, sia delle tecniche di lavorazione tradizionali di fresatura a controllo numerico. L'elettronica del sistema é stata progettata per caratterizzare elettricamente sensori di gas chemiresistivi in un ampio intervallo dei parametri di misura (i.e., resistenza e temperatura operativa del film sensibile, umiditá e temperatura dell'ambiente di lavoro). Al sistema é associato un software, sviluppato in Java, che semplifica la caratterizzazione elettrica dei sensori, automatizzando alcune procedure di misura, come l'acquisizione della caratteristica corrente-tensione e della caratteristica corrente-temperatura.
Un sensore chemiresistivo é normalmente approssimato ad una resistenza ideale. L'implementazione di queste caratterizzazioni nell'elettronica di misura permette quindi di tenere in considerazione la non linearitá di questa tipologia di dispositivi.
Il *setup* é stato validato sia utilizzando un sensore a base di un ossido metallico ampiamente utilizzato (ossido di stagno), sia caratterizzando un sensore basato su un innovativo semiconduttore non-ossido (carburo di silicio). Nel primo caso il sensore a base di ossido di stagno é stato esposto a monossido di carbonio ($CO$) e idrogeno ($H_2$) in differenti condizioni termodinamiche (e.g. temperatura di lavoro, potenziale applicato al film sensibile e composizione dell'atmosfera) ed é stata studiata la correlazione fra lo spettro DRIFT e le proprietá elettriche del film sensibile. L'analisi ha dimostrato la conformitá del sistema *operando* per studiare l'interazione solido-gas, approfondendo la cinetica sulla superficie del film sensibile. Il successivo studio riguardante dispositivi a base di carburo di silicio ha permesso di investigare il meccanismo di *sensing* nel rilevamento dell'anidride solforosa in condizioni di umiditá controllata, monitorando lo stato di ossidazione che porta alla formazione di una core-shell $SiC - SiO_xC$. Infine sono presentate due estensioni al sistema che permettono rispettivamente di effettuare misure *operando* DRIFT sia direttamente su polveri funzionali nano-strutturate in temperatura e sia su un sensore foto-attivato.

# English version

This Ph.D. thesis presents the development of an *operando* setup for the characterization of chemiresistive gas sensors using diffused infrared light spectroscopy (DRIFT). The research activities were focused on the parallel development of a testing chamber to include in the spectrometer and the coupled electronics for the acquisition and the analysis of the electric signals. The measuring chamber was designed to be compatible with a Fourier transform IR spectrometer Vertex V70 (Bruker) equipped with the DRIFT praying Mantis accessory (Harric scientific). For the mechanical design of the chamber, it was exploited both 3D printing technologies and traditional numerical control manufacturing techniques. The electronics of the system was designed to electrically characterize chemiresistive gas sensors in a wide range of parameters (i.e., resistance and working temperature of the sensing film, relative humidity and temperature of the measuring environment).
The system is managed by a software, written in Java, that simplifies the electrical characterization of the sensors, automating some measurement procedures, such as the acquisition of the current-voltage and current-temperature characteristics of the devices under test.
A chemiresistive gas sensor is usually approximated by an ideal resistor, and the implementation of these characteristics in the measuring electronics allows to consider the non-linearity of this type of devices. The setup was validated both characterizing a metal-oxide based gas sensor (tin dioxide) and investigative a innovative gas sensor based on a non-oxide semiconductor (silicon carbide). In the first case, the sensor based on tin dioxide was exposed to carbon monoxide ($CO$) and hydrogen ($H_2$) in different thermodynamic conditions (e.g., working temperature and potential applied to the sensing film, composition of the atmosphere). It was studied the correlation between the DRIFT spectrum and the electrical properties of the sensing film. This analysis has demonstrated the compliance of the *operando* system to study the gas-solid interactions by deepening the kinetics on the surface of the sensing film. Afterward, the investigation on the devices based on silicon carbide nanoparticles allowed to understand the sensing mechanism of the sulfur dioxide detection under controlled humidity conditions. It was also monitored the oxidation state of the film, which leads to the formation of a $SiC - SiO_xC$ core-shell.
Finally, two extensions to the system are presented, that allow to perform *operando* DRIFT measurements at high temperature directly on powders and on photo-activated sensors, respectively.

# Summary of research activities

During the three years of the Ph.D., various activities were carried out, not only related to the topics covered in the Ph.D. thesis. Overall, these activities led to the publication of the following papers in international journals:

1. M. Della Ciana, M. Valt, B. Fabbri, P. Bernardoni, V. Guidi, and V. Morandi. *"Development of a dedicated instrumentation for electrical and thermal characterization of chemiresistive gas sensors".* Review of Scientific Instruments, 92(7):074702, 2021.

2. Matteo Valt, Michele Della Ciana, Barbara Fabbri, Diego Sali, Andrea Gaiardo, and Vincenzo Guidi. *"Design and validation of a novel operando spectroscopy reaction chamber for chemoresistive gas sensors".* Sensors and Actuators B: Chemical, 341:130012, 2021.

3. A. Gaiardo, B. Fabbri, A. Giberti, M. Valt, S. Gherardi, V. Guidi, C. Malagú, P. Bellutti, G. Pepponi, D. Casotti, M. Della Ciana, et al. *"Tunable formation of nanostructured SiC/SiOC core-shell for selective detection of $SO_2$".* Sensors and Actuators B: Chemical, 305:127485, 2020.

4. Andrea Gaiardo, Giulia Zonta, Sandro Gherardi, Cesare Malagú, Barbara Fabbri, Matteo Valt, Lia Vanzetti, Nicoló Landini, Davide Casotti, Giuseppe Cruciani, Michele Della Ciana, et al. *"Nanostructured $SmFeO_3$ gas sensors: Investigation of the gas sensing performance reproducibility for colorectal cancer screening".* Sensors, 20(20):5910, 2020.

5. Arianna Rivalta ,Cristiano Albonetti, Davide Biancone, Michele Della Ciana, Simone d'Agostino, Laure Biniek, Martin Brinkmann, Andrea Giunchi, Tommaso Salzillo, Aldo Brillante, et al. *"Growth, morphology and molecular orientation of controlled indigo thin films on silicasurfaces".* Surfaces and Interfaces, 24:101058, 2021.

6. E. Spagnoli, S. Krik, B. Fabbri, M. Valt, M. Ardit, A. Gaiardo, L. Vanzetti, M. Della Ciana, V. Cristino, G. Vola, et al. *"Development and characterization of $WO_3$ nanoflakes for selective ethanol sensing".* Sensors and Actuators B: Chemical, 347:130593, 2021.

7. Massimiliano Cavallini, Ilse Manet, Marco Brucale, Laura Favaretto,Manuela Melucci, Lucia Maini, Fabiola Liscio, Michele della Ciana, and Denis Gentili. *"Rubbing induced reversible fluorescence switching in thiophene-based organic semiconductor films by mechanical amorphisation."* Journal of materials Chemistry C, 9(19):6234–6240, 2021.

To these works, a further work entitled "$SO_2$ sensing mechanism of nanostructured $SiC - SiO_xC$ core-shell: an *operando* DRIFT investigation" is awaiting publication, and another paper entitled "Design of a metal oxide solid solution for sub-ppm $H_2$ detection" has just been submitted.
The main research activity involved the development of a setup for the characterization in diffuse infrared light (DRIFT) of chemiresistive gas sensors *in operando*. The system has been developed in three parts: electronics and characterization software, measurement chamber, and FTIR spectrometer suitably configured.
The work on the electronics involved the design and implementation of both the hardware part and the software part. The electronics have been perfected through three successive versions, both as regards the performance and the miniaturization of the system. For practical reasons, only the latest version is described in the Ph.D. thesis, in which most of the design bugs have been solved.
The work on the mechanics involved both the design and construction of the measurement chamber housed inside the FTIR spectrometer. The design of the chamber required considerable effort, due to the limits imposed by the geometry of the spectrometer to which it had to be adapted. In this context, extensive use of 3D printing technologies (FDM, SLA) has been made, in order to iteratively optimize the geometry of the system. The definitive version of the measuring chamber was made of stainless steel, exploiting the mechanical workshops present at the Department of Physics and Earth Sciences of the University of Ferrara.
Once the system as a whole was completed, the setup was validated and a study on the sensing mechanism of gas sensors based on silicon carbide as functional material *in operando* was carried out.
In addition to the topics described within the Ph.D. thesis, other projects were also carried out. The main ones are:

- Setting up and maintenance of the 3D printing laboratory at IMM-CNR in Bologna,
- Study of electron-matter interaction in doped semiconductors through Montecarlo simulations based on the Geant4 framework,
- Creation of a setup for XRD measurements (X-Ray diffraction) *in-situ* in temperature ($[RT - 250]$) °C and controlled atmosphere,
- Creation of a setup for temperature ($[RT - 650]$ °C) and controlled atmosphere measurements on devices mounted on package TO-8 and TO-39,
- Creation of a setup for OCVD measurements (open-circuit voltage decay) for estimating the lifetime of the charge carriers inside a silicon carbide diode.

During the Ph.D. I attended as an auditor or speaker at various conferences and seminars, moreover, during the setting up of the 3D printing laboratory, I held an introduction course lasting 2 months (10 total lessons) inside IMM-CNR about Fusion 360

(3D development CAD) and 3D printing techniques.
I also had the opportunity to participate for a week in an experiment about selective ion transport through graphene oxide membranes at the synchrotron in Trieste (Electra), in which was used an electrochemical setup for XRD measurements *in-situ* that I developed at IMM-CNR in Bologna.

# Riassunto delle attivitá di ricerca

Nel corso dei tre anni di dottorato sono state svolte diverse attivitá, legate e non alle tematiche trattate all'interno della tesi di dottorato, attivitá che hanno portato alla pubblicazione dei seguenti articoli su riviste internazionali:

1. M. Della Ciana, M. Valt, B. Fabbri, P. Bernardoni, V. Guidi, and V. Morandi. *"Development of a dedicated instrumentation for electrical and thermal characterization of chemiresistive gas sensors".* Review of Scientific Instruments, 92(7):074702, 2021.

2. Matteo Valt, Michele Della Ciana, Barbara Fabbri, Diego Sali, Andrea Gaiardo, and Vincenzo Guidi. *"Design and validation of a novel operando spectroscopy reaction chamber for chemoresistive gas sensors".* Sensors and Actuators B: Chemical, 341:130012, 2021.

3. A. Gaiardo, B. Fabbri, A. Giberti, M. Valt, S. Gherardi, V. Guidi, C. Malagú, P. Bellutti, G. Pepponi, D. Casotti, M. Della Ciana, et al. *"Tunable formation of nanostructured SiC/SiOC core-shell for selective detection of $SO_2$".* Sensors and Actuators B: Chemical, 305:127485, 2020.

4. Andrea Gaiardo, Giulia Zonta, Sandro Gherardi, Cesare Malagú, Barbara Fabbri, Matteo Valt, Lia Vanzetti, Nicoló Landini, Davide Casotti, Giuseppe Cruciani, Michele Della Ciana, et al. *"Nanostructured $SmFeO_3$ gas sensors: Investigation of the gas sensing performance reproducibility for colorectal cancer screening".* Sensors, 20(20):5910, 2020.

5. Arianna Rivalta ,Cristiano Albonetti, Davide Biancone, Michele Della Ciana, Simone d'Agostino, Laure Biniek, Martin Brinkmann, Andrea Giunchi, Tommaso Salzillo, Aldo Brillante, et al. *"Growth, morphology and molecular orientation of controlled indigo thin films on silicasurfaces".* Surfaces and Interfaces, 24:101058, 2021.

6. E. Spagnoli, S. Krik, B. Fabbri, M. Valt, M. Ardit, A. Gaiardo, L. Vanzetti, M. Della Ciana, V. Cristino, G. Vola, et al. *"Development and characterization of $WO_3$ nanoflakes for selective ethanol sensing".* Sensors and Actuators B: Chemical, 347:130593, 2021.

7. Massimiliano Cavallini, Ilse Manet, Marco Brucale, Laura Favaretto,Manuela Melucci, Lucia Maini, Fabiola Liscio, Michele della Ciana, and Denis Gentili. *"Rubbing induced reversible fluorescence switching in thiophene-based organic semiconductor films by mechanical amorphisation."* Journal of Materials Chemistry C, 9(19):6234–6240, 2021.

A questi articoli si aggiunge un ulteriore lavoro in attesa di pubblicazione dal titolo "$SO_2$ sensing mechanism of nanostructured $SiC-SiOC$ core shell: an operando DRIFT investigation" e un lavoro appena sottomesso dal titolo "Design of a metal oxide solid solution for sub-ppm $H_2$ detection".
La principale attivitá di ricerca ha riguardato lo sviluppo di un *setup* per la caratterizzazione in luce infrarossa diffusa *(DRIFT)* di sensori di gas chemiresistivi *in operando*. Il sistema é stato sviluppato in tre parti: elettronica e software di caratterizzazione, camera di misura, spettrometro FTIR opportunamente configurato.
Il lavoro sull'elettronica ha riguardato la progettazione e la realizzazione sia della parte *hardware*, sia della parte *software*. L'elettronica é stata perfezionata attraverso tre versioni successive, sia per quanto riguarda le *performance*, sia per quanto riguarda la miniaturizzazione del sistema. Per questioni pratiche nella tesi di dottorato é descritta solo l'ultima versione, nella quale sono stati risolti la maggior parte dei difetti progettuali.
Il lavoro sulla meccanica di misura ha riguardato sia la progettazione, sia la realizzazione della camera di misura alloggiata all'interno dello spettrometro FTIR. Il *design* della camera ha necessitato di un considerevole sforzo, visti i limiti costruttivi imposti dalla geometria dello spettrometro al quale si doveva adattare, limiti che sono in parte descritti all'interno della tesi di dottorato. In questo contesto é stato fatto un largo utilizzo delle tecnologie di stampa 3D (FDM, SLA) in modo da ottimizzare iterativamente la geometria del sistema.
La versione definitiva della camera di misura é stata fabbricata in acciaio INOX sfruttando le officine meccaniche presenti al dipartimento di fisica e scienze della terra dell'Universitá di Ferrara.
Terminato il sistema nel suo complesso, il *setup* é stato validato ed é stato portato avanti uno studio sul meccanismo di *sensing* di sensori di gas basati su carburo di silicio come materiale funzionale *in operando*.
Oltre alle tematiche affrontate all'interno della tesi di dottorato, sono stati portati avanti anche altri progetti. I principali sono:

- Allestimento e mantenimento del laboratorio di stampa 3D presso l'IMM-CNR di Bologna,
- Studio dell'interazione elettrone-materia in semiconduttori drogati attraverso simulazioni Montecarlo basate sul *framework* Geant4,
- Realizzazione di un *setup* per misurazioni XRD *(X-Ray diffraction) in-situ* in temperatura ($[RT - 250]$) °C ed atmosfera controllata,

- Realizzazione di un *setup* per misurazioni in temperatura ($[RT - 650]$ °C) ed atmosfera controllata su dispositivi montati su *package* TO-8 e TO-39,

- Realizzazione di un *setup* per misurazioni OCVD *(open circuit voltage decay)* per la stima del tempo di vita dei portatori di carica all'interno di un diodo in carburo di silicio.

Durante il dottorato ho partecipato come uditore e oratore a varie conferenze e seminari, inoltre, in occasione dell'allestimento del laboratorio di stampa 3D, ho tenuto un corso della durata di 2 mesi (10 lezioni totali) all'IMM-CNR, per introdurre all'utilizzo di Fusion 360 (CAD di sviluppo 3D) e alle tecniche di stampa.
Ho anche avuto modo di partecipare ad un esperimento della durata di una settimana sul trasporto ionico selettivo attraverso membrane di ossido di grafene presso il sincrotrone di Trieste (Electra), nel quale é stato utilizzato un *setup* elettochimico per misurazioni XRD *in-situ* che ho sviluppato presso l'IMM-CNR di Bologna.

# Introduction

A gas sensor measures the concentration of one or more gases present in the atmosphere to which it is exposed or emulates to a certain extent the role of human smell in the digital world. Gas sensors are currently used in various practical situations, including:

- Environmental monitoring, to control the concentration of greenhouse gases in the atmosphere [1].
- Industrial or domestic monitoring, to prevent dangerous situations due to harmful gases released in a closed environment.
- Agri-food and precision farming, to monitor the conservation status of food [2] or to correlate the gaseous emissions of crops with their health conditions [3].
- Medical diagnostics, through the analysis of gases present in the human exhalations to test the presence of respiratory or intestinal diseases in a non-invasive and cost-effective way [4, 5].

Depending on the applications, both for performance and cost restriction, there are different types of gas sensors, which use different technologies and chemical-physical mechanisms [6, 7, 8, 9]: optical, chromatographic, surface acoustic waves, electrochemical, and semiconductor-based gas sensors.
The work here proposed it is focused on solid-state gas sensors. In particular, a chemiresitive gas sensor is a device that transduces a variation of the environmental chemical composition in a variation of the electrical resistance. This sensors are composed of a functional film deposited on an inert substrate, which allows to collect the electrical signal and to heat the sensing layer. Solid-state gas sensors have many advantages over other technologies, mainly related to production processes that allow them to be scalable and joined with integrated circuit technologies (ICT). Indeed, compared to other devices, the performance of a chemiresistive gas sensor are not affected by the size reduction. Then, it is possible to exploit the miniaturization processes developed for micro electromechanical systems (MEMS), consequently reducing the production costs of the single device and improving the performance [10]. Despite these advantages, chemiresistive gas sensors have some unresolved issues. Indeed, although there are sensors that are highly

sensitive even to small concentrations of gas, these devices features poor selectivity and stability. Another limitation of chemiresistive gas sensors is the operating temperature that, for example in the case of metal oxides, exceeds 200 °C. Working continuously at high temperatures limits the implementation in portable gas monitoring equipment due to a considerable energy consumption. However, this problem has been partially solved, leading the research, on one side, towards room-temperature operating or photoactivated materials [11], and on the other side to the miniaturization of the devices.
Nowadays, in order to accomplish the gas sensor market demands, the research studies aim to deeply investigate the adsorption of the gaseous species on the sensing film and/or the catalysis of chemical reactions on the surface. Indeed, these mechanisms modify the electronic properties of the functional materials, which are exploited to measure the type and the concentration of the gas that has interacted.
Experimentally there are many techniques to characterize the chemistry of a surface. However, a family of particularly interesting methods for the characterization of a chemiresistive gas sensor concerns the *operando* methods, which can be used directly on a working sensor. Therefore, characterizing a sensor *in operando* allows to uniquely correlate a stimulus (i.e., the presence of gas) to a modification of the surface chemistry of a sensor and then to an electrical signal.
The most used techniques for the characterization of a *operando* chemiresistive gas sensor are [12]: X-ray-based techniques (XAS, XRD, and XPS), atomic force microscopy (AFM, KPAFM), and optical spectroscopy (visible-ultraviolet absorption, infrared absorption, Raman).
Within these techniques, infrared spectroscopy in the medium infrared (400 - 4000 $cm^{-1}$) allow estimating the concentration of specific molecular chemical bonds in a sample. Then, it is possible to extract its chemical composition and, in the case of the film of a chemiresistive sensor, to evaluate the concentration of adsorbed gaseous species and/or of the reaction products catalyzed on the surface.
Among the infrared spectroscopy techniques, diffuse reflectance infrared Fourier transform (DRIFT) is particularly suitable for the characterization of nanostructured powders since it exploits the intrinsic property of a powder to diffuse light.
This work focuses on developing an experimental setup for DRIFT measurements on *operando* chemiresistive gas sensors. This system requires a performing spectrometer for infrared measurements and a dedicated electronics that allows to characterize various sensing materials. For this purpose, a *Vertex V70 Bruker* Fourier Transform Infrared (FTIR) spectrometer equipped with *Praying Mantis* DRIFT accessory by *Harrick scientific* was used. Moreover, to obtain the maximum flexibility, it is presented a low-powered and minimal dimensions instrumentation, as required by promising applications in gas sensing. Then, the electronics was customized to monitor and to control the measuring parameters in order to optimize the characterization of different chemiresistive gas sensors.

This Ph.D. thesis is organized in four chapters and three appendixes.
Chapter one provides an overview on chemiresistive gas sensors, describing the fabrication of a typical device, its functionality, and the parameters used to estimate the sensing performance.
Chapter two introduces the infrared radiation and its interaction with the matter, then it deepens the instrumentation for spectroscopic analyses and in particular the DRIFT technique.
Chapter three describes the realization and the validation of the *operando* setup. This chapter deepens the mechanical design of the test chamber where the sensors are housed, the electrical implementation of the measuring equipment, and the proof of the system as a whole by testing a tin dioxide based gas sensor as a reference.
Chapter four deals the investigation on the selective $SO_2$ detection mechanism of silicon carbide based sensors. By *operando* DRIFT spectroscopy, it was studied the formation of an oxide layer of silica on the sensing film surface at increasing working temperatures. Moreover, it was highlighted the influence of the $SO_2$ on the infrared spectrum during the gas exposure, both in dry and wet conditions. Finally, it was investigated the possible sensing mechanism of an oxidized silicon carbide film.
Therefore, the conclusions of this work are presented, highlighting the potential future developments.
At the end, the three appendixes presents: the 3D printing techniques employed for the development of the test chamber, the addons for *operando* measurements on heated powders and on photoactivated sensors, and all the mechanical drawings used.

# Chapter 1

# Chemiresistive gas sensor

## 1.1 Introduction

The development of chemiresistive gas sensors based on semiconductor materials dates back to the second half of the '900 when some pioneering publications showed that some materials could discriminate the presence of dilute gases in the atmosphere [13]. From that moment, thanks also to the commercial success of the first chemiresistive sensors introduced on the market [14, 15], the effort to manufacture increasingly performing sensors has continued uninterrupted, both in the research of new sensing materials and for the development of more reliable devices.
Gas sensors currently cover a large slice of the sensors market, being used in different applications daily, including monitoring the safety condition in the workplace, monitoring atmospheric pollutants, or simply monitoring the air quality in domestic environments. In a world where every device needs to interact more and more with the surrounding environment, the possibility of having miniaturized gas sensors is very attractive. For this reason, the market for chemiresistive gas sensors continues to grow up [16].
From the empirical point of view, the operation of a chemiresistive gas sensor is quite simple: a sensor, heated at the proper temperature, detects the presence of a target gas through the modification of the resistance of the sensing material of which it is composed, and under appropriate conditions. From this variation, it is possible also to evaluate the concentration and/or the nature of the gas interacting [17].
Despite the simplicity of operation, several non-ideal effects compromise the ease of use of a chemiresistive gas sensor. A rather significant problem is the interference due to other gases mixed with the target gas to be measured. In particular, it is experimentally verified that chemically similar gases (e.g., oxidizing or reducing gases) tend to interact similarly; furthermore, it has been observed that gases normally present in the air in variable concentrations, such as $CO_2$ and water vapor ($H_2O$), affect the correct operation of a sensor, compromising its reliability [18]. Another important consideration is

the sensor working temperature. Most chemiresistive gas sensors, to perform reliably, need to operate at a high temperature ($150 - 400$ °C) [17]. Maintaining a sensor at a high temperature for long periods of time is very energy consuming, and that is a limiting parameter, especially for portable devices. Nowadays, this problem has been partially solved thanks to Micro-Electro-Mechanical Systems (MEMS) manufacturing technologies. Actually, the miniaturization of chemiresistive gas sensors, together with the on-chip integration of the driving elements, has permitted to drastically reduce the energy consumption and the dimensions, allowing chemiresistive gas sensors to be used also in energetically stand-alone portable system [19, 10].
Among the materials studied, the semiconductors that gave the best results in terms of long-term performance for monitoring the gas concentration were metal oxides (MOX), both in the form of nanoparticles and bulk. Actually, metal oxides such as tin oxide ($SnO_2$), tungsten oxide ($WO_3$), and titanium oxide ($TiO_2$) cover almost all of the devices currently used in the market since they showed that with a proper calibration, it is possible to operate reproducibly for years from their manufacture. Despite the popularity of MOXs in chemiresistive gas sensors, other types of semiconductors have shown promising performances, both inorganic (metal sulphides [20], SiC [21], etc.) and organic materials (2D materials [22, 23], carbon nanotube, etc).
In conclusion, the success of chemiresistive gas sensors is due to a combination of technological efforts and research in new materials. Together, these advancements have made it possible to obtain performing, selective and low-powered devices. In the following paragraphs, the structure and manufacturing techniques of a typical chemiresistive gas sensor will be presented, using as an example the sensors made and studied at the Sensors Laboratory at the University of Ferrara (Unife). Afterward, the different types of sensing materials will be introduced, taking as an example some of the most studied materials to describe the different operating principles. Finally, the sensing properties of a chemiresistive gas sensor will be defined, underlining the most significant parameters used to classify the performance.

## 1.2 Structure and fabrication

Conceptually, a gas sensor can be divided into two parts: the substrate and the sensing material. The last is the element that actually detects the presence of gas and acts as a transducer by correlating the concentration of a target gas to its electrical resistivity [24]. The substrate is the support on which the sensing material is deposited and, depending on the level of complexity of the device, it can be integrated with a series of components that allow its use. As an example, on the left in the Figure 1.1 is shown the structure of a typical chemiresistive gas sensor made in the sensor laboratory at the University of Ferrara [24].

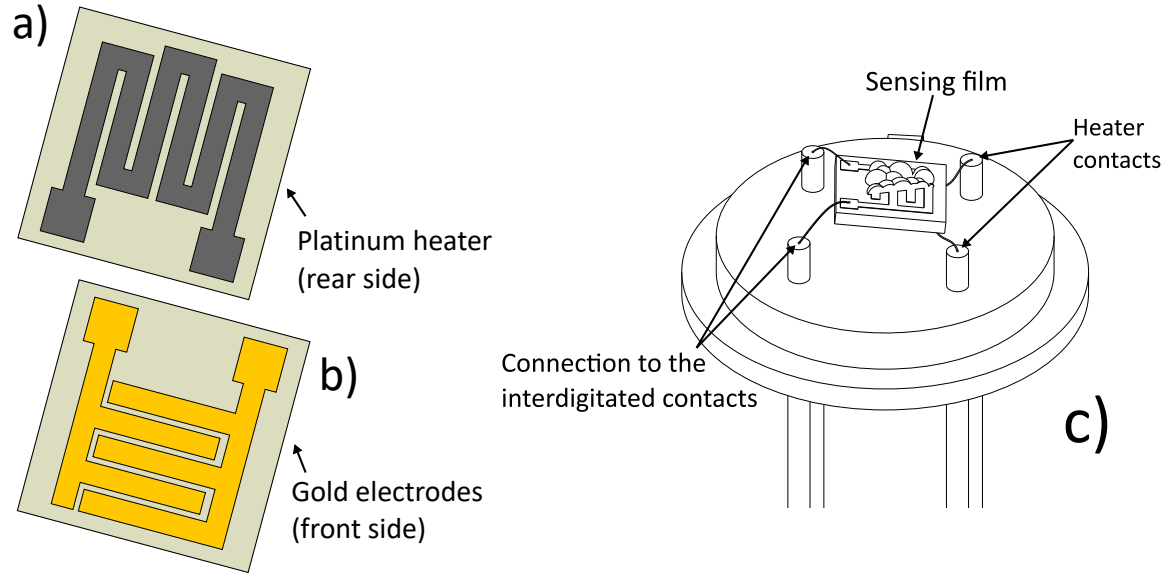


Figure 1.1: The figure on the left shows the structure of the alumina substrates used in Ferrara to fabricate chemiresistive gas sensors. On the front side (b), there are two gold electrodes to form an interdigitated on which the sensing film is deposited, while on the opposite side (a), there is a platinum serpentine used to set the temperature of the device. On the right (c) is displayed a completed chemiresistive gas sensor, mounted suspended on a TO-39.

### 1.2.1 Substrate

The substrate is the support on which the sensing layer is deposited; it includes a heater element and two electrodes. The heater (Figure 1.1 a) is used to apply the optimal working temperature to the sensor, and, to minimize the dimensions of the sensor, it is used both to provide power and to measure the temperature by working as a positive temperature coefficient (PTC) thermistor.
Different materials can be used as substrates, such as ceramic or even plastic materials, depending on the working conditions [10, 25]. The substrates used at the University of Ferrara are made of a square die of alumina, with a side of 2.5 mm and a thickness of 0.3 mm [24]. The heater is made of a platinum serpentine, deposited on the rear side, and it has a resistance of approximately $10 \pm 2\ \Omega$ at RT (room temperature). The electrodes, on which the sensing layer is deposited, are made of two interdigitated gold contacts, 10 $\mu m$ thick and 220 $\mu m$ wide, with a separation between the same contacts of 150 $\mu m$. The sensors are mounted on a standard 4-pin transistor outline package (TO-39), following the configuration in Figure 1.1 b.
To limit the thermal dispersion, sensors are bonded using four gold wires (0.06 mm) that connect and sustain the substrate to the TO-39.

### 1.2.2 Sensing film

The sensing layer is the part of a chemiresistive gas sensor that detects the presence of a target gas by changing its properties (i.e., electrical resistance). Indeed, the interaction of gaseous molecules with the sensing layer activates a chemical reaction that results in an overall modification of the electrical properties of the employed materials. These are usually metal-oxide semiconductors that are referred to as MOX (Metal OXide) [24]. However, many different sensing materials have been investigated to improve the sensors performance, both as pristine or combined with other additives known to act as catalysts, such as noble metals [26, 27]. In particular, the doping/decoration with selected compounds allows optimizing the properties of the devices, such as the selectivity to a specific gas or the overall response of the sensor [28]. Since gas detection in chemiresistive devices is a surface mechanism, nanostructured materials, such as nanoparticles, are usually employed to maximize the surface-active area [29]. Many techniques have been developed to obtain fine powders. The most used for the preparations of MOX nanoparticles are a wet processes, in which the precipitation of a precursor of the oxide is obtained from an aqueous solution of its metal salt(s) [30]. The precursors are then gently washed, dried, and calcinated to obtain the final powder. Many technologies have been developed to deposit the sensing layer of chemiresistive gas sensors, both as thin or thick films. In the sensors Lab. of Unife, sensors are fabricated by screen printing a thick film. In this process, the nanostructured functional powder is loaded with a mix of inert sinterer and then converted into a slurry paste by milling it using water or an organic carrier together with possible additives. The paste is then deposited and sintered to form a sensing layer of approximately $20 - 30\ \mu m$.

## 1.3 Theory and Sensing properties

Parallel to the technological research for the manufacture of increasingly performing chemiresistive gas sensors has continued the effort on understanding the sensing properties of the sensing materials employed, both in the form of nanoparticles deposited as thick films and in the form of compact layers. From a practical point of view, every chemiresistive gas sensor is used similarly, that is, by measuring the conductivity of the sensing film as a function of the composition of the working atmosphere. However, different models have been proposed about the conduction and sensing mechanisms, depending on the materials and morphologies used.
In the field of chemiresistive gas sensors, the materials most studied both from a technological and a theoretical point of view are metal oxides in the form of nanoparticles. For this reason, as an example, their sensing mechanism is proposed, which can also be generalized to other families of materials.

### 1.3.1 Working principle

In a chemiresistive gas sensor based on metal oxides, the detection of a gas is in principle straightforward [31]: in air, at a temperature between 150 and 400 °C, oxygen atom is adsorbed on the surface of the oxide, where it captures an electron, becoming a negative ion. This mechanism has the overall effect of modifying the sensor resistance, increasing it for $n$-type semiconductors, or reducing it for $p$-type semiconductors. When an additional gas is introduced, depending on the type of gas, two mechanisms can be triggered, in which either the pre-adsorbed oxygen reacts with the target gas or the gas itself is adsorbed on the surface. The two effects are opposite to each other, but both result in a relative change in the sensor resistance, whose intensity determines the response of the device.
This explanation highlights the importance that surface reactions play on the sensing mechanism and how they trigger a change in the macroscopic electrical properties. The importance of oxygen is also highlighted since its interaction with the film contribute to determine the sensing properties of a material.

#### The role of oxygen

In MOX, oxygen plays a crucial role in the sensing mechanism since the quantity of oxygen adsorbed at equilibrium contributes to define the electrical properties of a chemiresistive gas sensor [31, 26, 27].
However, it is important to underline that depending on the type of semiconductor, oxygen affects the electrical properties oppositely. Indeed, in an $n$-type semiconductor, the adsorbed oxygen inhibits conduction, while on the contrary, in a $p$-type semiconductor, the adsorbed oxygen increases the conductivity. To understand this effect, we start considering a film of nanoparticles of a metal oxide exposed to atmospheric oxygen. Whether the oxide is $n$-type (e.g., $SnO_2$, $WO_3$) or $p$-type (e.g., $Cr_2O_3$, $CuO$), in working conditions, the oxygen in the atmosphere is partly adsorbed on the surface, becoming a negative ion by capturing an electron from the oxide. The release of an electron by the oxide to the adsorbed oxygen causes a positive charge to remain exposed on the nanoparticle's surface. From the point of view of the energy bands, this positive charge appears as a deep and localized acceptor state. A localized state is a state whose energy is deep within the energy band gap of the material, and once occupied, it requires high energy to be released.
Although the formation of surface states occurs in the same fashion in both types of semiconductors, how the energy bands rearrange depends on whether the metal oxide is of type $n$ or type $p$.
The Figure 1.2 displays the resulting band structure of $n$-type metal oxide when exposed to atmospheric oxygen in working conditions.

In an $n$-type semiconductor, the electrical conduction is given by the electrons in the

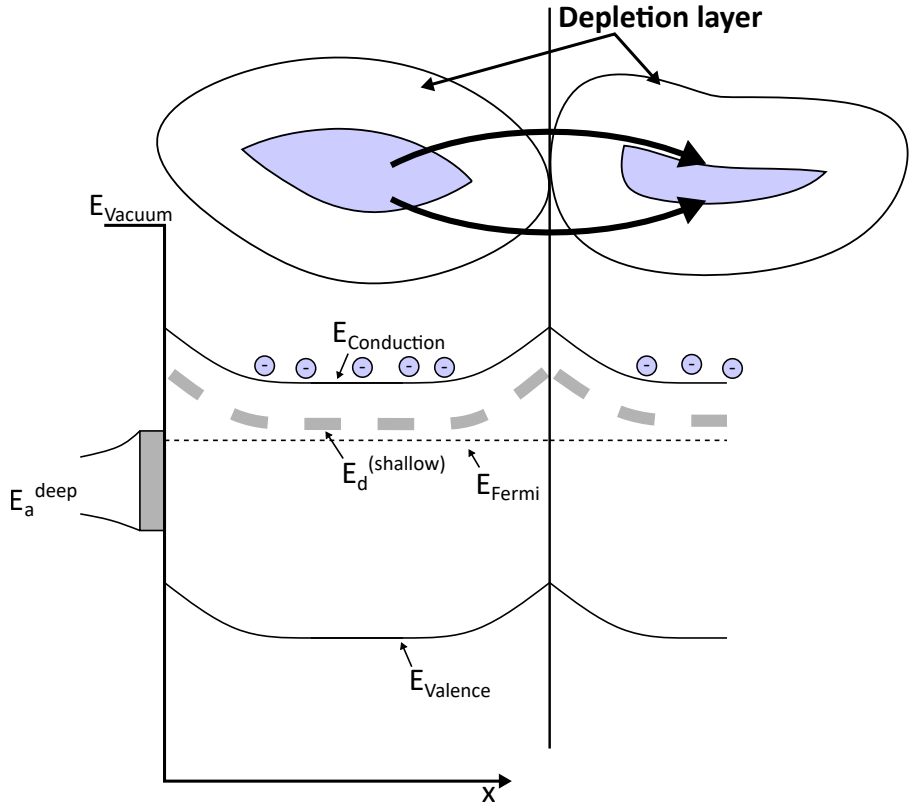


Figure 1.2: The figure shows the reorganization of the band structure of an $n$-type metal-oxide nanoparticle, where the surface is covered by oxygen atoms adsorbed in ionic form. The adsorbed oxygens form a series of deep acceptor states on the surface ($E_a^{deep}$), which are partially occupied by the electrons in the conduction band. This mechanism triggers the formation of an electric field and a depletion layer on the surface that inhibit the transport of electrons between particles.

conduction band, which is partially occupied thanks to the electrons coming from the partially ionized shallow donor states ($E_d^{shallow}$). When oxygen is adsorbed on the surface of the oxide, a series of deep states are formed, localized on the surface, and identified in the Figure 1.2 as $E_a^{deep}$. These states tend to be partly occupied by electrons in the conduction band, resulting in forming an electric field on the surface. This area, therefore, remains stripped of mobile charges since it has distributed its free electrons on the states located on the surface, and for this reason, this zone is called depletion layer. Then the particles are in contact through depleted areas that prevent electrons' transport between the particles. From the point of view the macroscopical electrical characteristics, the overall effect is transduced through a decrease in conductivity and, therefore, an increase in the overall resistance of the sensor with an intensity related to the width of the depletion layer and the height of the potential barrier between particles.

The mechanism by which oxygen present in the atmosphere decreases the conductivity of an $n$-type metal oxide is thus explained. In a semiconductor of the $p$-type, on the other hand, the situation is different and is schematized in Figure 1.3.

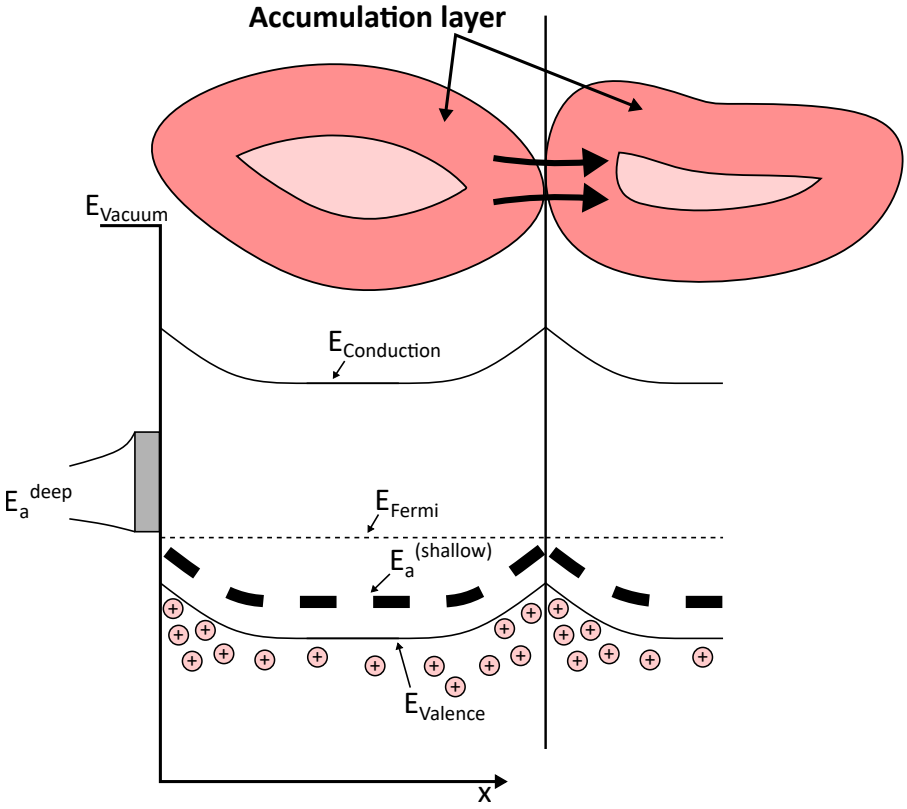


Figure 1.3: The figure shows the reorganization of the band structure of a $p$-type metal-oxide nanoparticle, where the surface is covered by oxygen atoms adsorbed in ionic form. The adsorbed oxygens form a series of deep acceptor states on the $E_a^{deep}$ surface, which is partially occupied by the electrons in the valence band. This mechanism triggers the formation of an electric field and an enrichment region on the surface, which favors the transport of the holes between the particles.

In a semiconductor of the $p$-type, conduction is given by the holes in the valence band, which is partially depleted due to the electrons occupying the shallow acceptor states ($E_a^{shallow}$) partially ionized. In this case, surface states formed by the adsorbed oxygen ($E_a^{deep}$) are partly occupied by electrons in the valence band. This mechanism leads to the formation of an electric field on the surface, however, in this case instead of forming an empty layer, a layer enriched in holes is formed. Indeed, each electron donated by the valence band leaves a hole in its place, which increases the surface electrical conductivity of the material. Contrary to the previous case, the particles are in contact with each other through areas enriched with carriers, which facilitates the transport of charges

across the surface of the particles. From the point of view of its macroscopical electrical characteristics, the overall effect is an increase in electrical conductivity and, therefore, a decrease in the sensor's resistance. In fact, the hole transport from one particle to another is favored.
This model, even qualitatively, demonstrates that despite the same interaction of oxygen in semiconductors of $n$-type and $p$-type, the rearrangement of the band structure depends on the type of semiconductor, and in conclusion, the electrical conductivity is inhibited in one case and favored in the other.

### Reducing gases

Reducing gas is a gas that has a tendency to donate an electron. When a reducing gas comes in contact with the surface of a metal oxide, it tends to oxidize, preferably reacting with the oxygen adsorbed on the surface of the metal oxide itself since it is in ionic form. This reaction decreases the concentration of oxygen adsorbed at equilibrium on the surface of the metal oxide, which acts as a catalyst for the oxidation of the target gas (Figure 1.4, left) [31]. As seen in the previous paragraph, a variation in the adsorbed oxygen triggers a variation in the resistivity of the sensing film, which increases or decreases depending on whether the metal oxide is $n$-type or $p$-type, respectively. Exploiting this effect, from the measurement of the resistance of the chemiresistive gas sensor, it is possible to obtain information on the concentration of the target gas in the interacting atmosphere. In the field of gas sensing, the most studied reducing gases are $H_2$, $CO$, $CH_4$, $NO$ and more in general $VOCs$ (Volatile Organic Compounds). These gases are of great interest from an application point of view since they are flammable gases. Therefore, the monitoring of their concentration in closed environments is essential for the prevention of accidents.

### Oxidizing gases

An oxidizing gas is a gas that has a tendency to capture an electron. When an oxidizing gas comes into contact with the surface of a metal oxide, it behaves like oxygen and it is partially adsorbed by capturing an electron and, in turn, forming a negative ion on the surface of the sensing film (Figure 1.4, left). Depending on the type of gas, the type of metal oxide, and the working conditions, the adsorption can be more or less competitive with oxygen and triggers the formation of further acceptor states on the surface, as described in the previous paragraph. The increase of these states leads to an enlargement of the depletion or enrichment region on the metal oxide surface, depending on whether this is an $n$-type or a $p$-type semiconductor. Therefore, the overall effect is a variation of the resistivity of the sensing film, which increases or decreases depending on whether the metal oxide is of the $p$ or $n$-type, respectively. In the field of gas sensing, the most studied reducing gases are $NO_2$, $SO_2$, $O_3$, $CO_2$, etc., as they are toxic gases

for humans even at small concentrations.

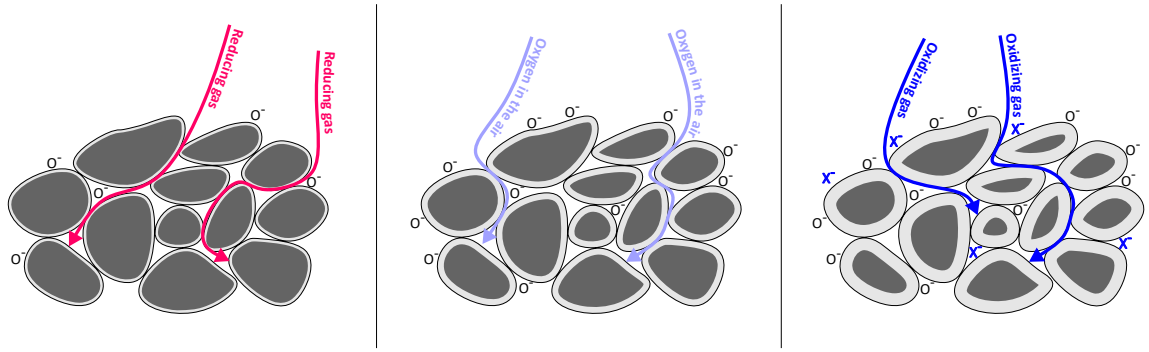


Figure 1.4: The figure shows the standard mechanism by which a reducing gas (left) or an oxidizing gas (right) interacts with a metal oxide in a chemiresistive gas sensor with pre-adsorbed oxygen (center). An oxidizing gas increases the number of surface states by interacting with the surface competitively with oxygen. On the other hand, a reducing gas is favored to oxidize by capturing pre-adsorbed oxygen on the surface, decreasing its surface concentration. In conclusion, an oxidizing gas improves the enrichment/depletion region on the surface of the particles while reducing gas contracts it.

### Conclusions

The qualitatively described model of the metal-oxide sensing mechanism distinguishes four distinct situations in relation to the variation of the resistance of a chemiresistive gas sensor:

- $n$-type semiconductor metal oxide and reducing gas $\longrightarrow$ the resistance decreases.
- $n$-type semiconductor metal oxide and oxidizing gas $\longrightarrow$ the resistance increase.
- $p$-type semiconductor metal oxide and reducing gas $\longrightarrow$ the resistance increase.
- $p$-type semiconductor metal oxide and oxidizing gas $\longrightarrow$ the resistance decreases.

These simple conclusions allow a chemiresistive gas sensor with a known composition of the sensing film to discriminate oxidizing gas from a reducing gas but not distinguish gases belonging to the same family.
However, as mentioned in the previous paragraphs, the response of the chemiresistive gas sensors is also influenced by other gases that do not belong to these two families, including water vapor ($H_2O$) and carbon dioxide ($CO_2$), which are normally present in the atmosphere. The sensitivity to gases that are not oxidants or reductants underlines the fact that different sensing mechanisms compete in real conditions. In order to provide

the correct interpretation of these mechanisms, it is essential to investigate the surface species present on the surface of a gas sensor in working conditions. To reach this goal, we developed a setup to perform *DRIFT* measurements on *operando* chemiresistive gas sensors, to have an experimental feedback on the catalyzed reactions on the sensors surface, and hopefully the development of more accurate theoretical models.

### 1.3.2 Sensing properties

The sensing properties of a chemiresistive gas sensor are extracted by monitoring the current or the electrical resistance of the sensor's sensing film during the exposure to a target gas. The Figure 1.5 shows the typical trend of the current during this type of measurement [31].

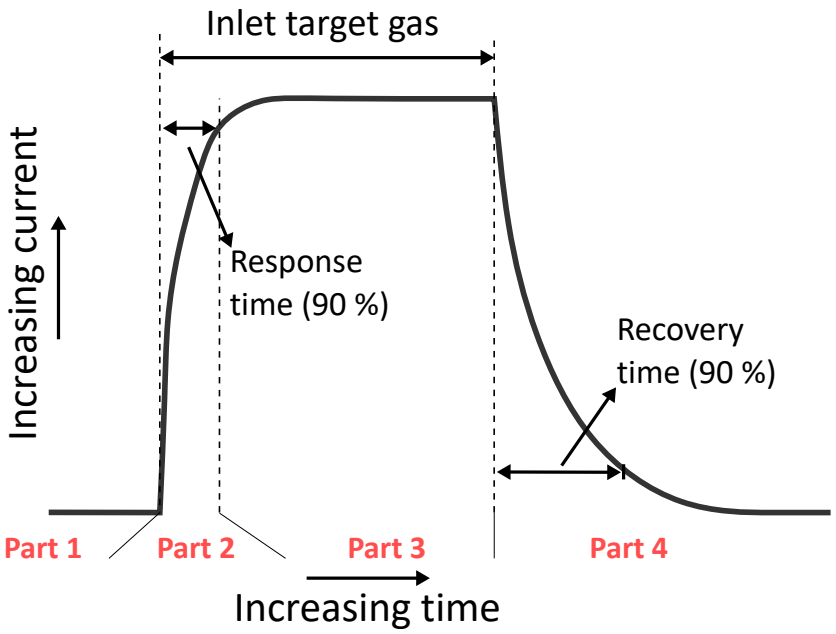


Figure 1.5: The graph represents the ideal raw signal (e.g., current) of a chemiresistive gas sensor while injecting a target gas. From this curve, it is possible to calculate the intensity of the response and the response and recovery times.

The curve is divided into 4 areas:

1. **Baseline in synthetic air**. Before the insertion of the target gas, the sensor is left in working conditions (i.e., in synthetic air and at the operating temperature) for the time necessary for the current to reach a stable plate over time.

2. **Target gas injection**. When the current reaches equilibrium, the atmosphere to which the sensor is exposed is changed with the addition of the target gas. The gas modifies the electrical resistance of the sensing film by increasing or decreasing it according to the type of interaction.

3. **Signal stabilization**. The target gas is held until the current stabilizes at a new stable value.

4. **Return to the initial state**. The target gas is removed, and the sensor is returned to the initial conditions. This condition is maintained until the current stabilizes again.

Each curve zone in the Figure 1.5 allows extracting different parameters, such as response, reactivity, and recovery time. Other fundamental properties that define the performance of a chemiresistive gas sensor are selectivity, detection limit, stability/reproducibility, operating temperature, and linearity of the current-voltage (I-V) characteristic [27]. These sensor parameters are used to characterize a sensing material or, more generally, a device. An ideal sensor should be highly sensitive, stable, possessing good selectivity, low recovery and response time, and linear current-voltage characteristic. Moreover, it is better that sensors could be operated at a low temperature, since it require less power to operate.

### Sensor Response

The response of chemiresistive gas sensors is defined as the relative variation of an appropriate physical quantity (e.g., resistance, conductance, circulating current, etc.) with respect to the exposure to an analyte (i.e., tested gas) [32]. Indicating this physical quantity as $X$, the response can be defined by the formula:

$$Response = \left| \frac{(X_{Air} - X)}{X_{Air}} \right| \tag{1.1}$$

where $X$ and $X_{Air}$ are the values of the selected quantity when the sensor is exposed or not to the analyte, respectively. Usually, resistance or the current through the sensing film is used to calculate the response, depending on the linearity of the current-voltage characteristic of the sensor [32, 21]. The response is undoubtedly one of the most important parameters that define the sensitivity of a sensor, as it is used to calibrate the sensor *vs.* the concentration of a target gas. The response depends on the the working condition and the type of the sensing film.

### Response Time

The physical parameters of sensors do not stabilize immediately after the target gas exposure. It requires a certain time, which is called response time. Response time is

the time that a sensor requires to change its signal (e.g., current or resistance) from the initial state (equilibrium) to a final one (in general taken as 90% of the final value) after the exposure to target molecules. A typical evaluation of the response time in a gas sensor is shown in the second part of the curve in Figure 1.5. The response time of a practical sensor ranges between tens of seconds and 20 min.

### Recovery Time

In order to work repeatedly in practical application, sensors should recover their values (initial baseline) when the target gas is evacuated. Recovery time is the time to return the measured signal to the baseline value after the target gas is removed (to 90% of the original baseline signal). Most chemiresistive gas sensors can be used repeatedly, with a recovery time ranging from few seconds to tens of minutes. Both response and recovery times are related to the adsorption and desorption kinetics of the analyte. So they depend on the temperature and the pressure/concentration of the target gases.

### Operating temperature

Most chemiresistive gas sensors to operate reliably require to work at high temperatures. Tuning the right temperature is crucial to maximize the sensors' sensitivity and reducing response and recovery time. Typical working temperature goes from 100 °C up to 600 °C, depending on the material and the target gas to detect. Indeed, it has been verified that also selectivity can be improved by tuning the working temperature. A useful tool to investigate the behavior of a sensor at different temperatures is the current-temperature (I-T) curve, also known as the Arrhenius plot. Indeed, by increasing and decreasing the temperature, it is possible to observe the absorption and desorption of the molecules bound on the surface and, at the same time, to obtain information on the conduction mechanism of the sensing material.

### Selectivity

The selectivity of sensors refers to the characteristics that define whether the sensor can respond selectively to a particular target analyte in the presence of other analytes under similar operating conditions. The selectivity of a sensor can be expressed as:

$$Selectivity = \frac{S_i}{S_g} \tag{1.2}$$

where $S_i$ is the sensor's sensitivity toward interface species, and $S_g$ is the sensor's sensitivity toward target species.

### Detection Limit

A sensor must be capable of detecting very low concentrations of the target gas. The detection limit is the minimum concentration of the target gas, which a sensor can detect under certain conditions. One way to determine the limit of detection is based on the signal-to-noise approach: the ratio of signal to noise is performed by comparing measured signals at low concentrations with the noise of the measurement. Also, the driving circuit affects the detection limit since both the stability of thermodynamic conditions, and the resolution of the measuring system affect the measures.

### Stability and Repeatability

One of the most frequent problems of any sensor is the drift of the signal. The stability/repeatability of the sensor material determines the possibility of multiple recoveries of its parameters after many cycles of sensor performance.

### Linearity of the current-voltage characteristic

The current-voltage characteristic is the current measurement through the sensing film as a function of the applied potential. In an ideal chemiresistive gas sensor, the I-V characteristic is a straight line passing through the origin in every thermodynamic condition. In this situation, the sensor is completely described by its electrical resistance. However, especially on sensors obtained from powders of semiconductor materials, the characteristic also for potentials of the order of a few volts shows a non-linear trend. This means that the performance of a sensor depends in turn on the potential applied. A more detailed discussion on the subject will be described in the following chapters.

# Chapter 2

# Infrared Spectroscopy

## 2.1 Introduction

Infrared (IR) spectroscopy concerns the study of the interaction of infrared radiation with matter and is, without a doubt, one of the most used spectroscopic techniques employed for studying the chemistry of new materials [33]. Choosing the most suitable analysis technique makes it possible to investigate both qualitatively and quantitatively samples virtually in any state, such as solids, powders, pastes, liquids, or gases [34]. Therefore, the infrared spectroscopy is a technique applicable to many different research fields [35, 36, 37].
The success of infrared spectroscopy in recent decades is certainly also due to the development of new instruments based on Fourier transform spectroscopy. The first studies on infrared radiation date back to the beginning of the last century, when dispersive elements, such as prisms and subsequently suitable diffraction gratings, were used to measure the interaction of matter with the single components of a continuous light spectrum. Nowadays, almost all of the equipment used is instead composed of Fourier transform spectrometers [33], which have drastically improved the quality of the acquired spectra, leading the way for different applications.
The most direct way to characterize a material in IR radiation is to measure the absorption spectrum that conceptually indicates the ability of a sample to absorb light at a given wavelength. There are various ways of representing the absorption spectrum; the simplest is in transmission, in which the spectrum of a sample is defined as the ratio between the intensity of the transmitted light and the intensity of the incident light at a given wavelength.
From a phenomenological point of view, the spectrum of a substance appears as a continuous function in which peaks are corresponding to certain frequencies. Microscopically, these peaks are interpreted as the excitation of the ground state of the vibrational modes of atoms and molecules and are therefore characteristic of the structure and composition

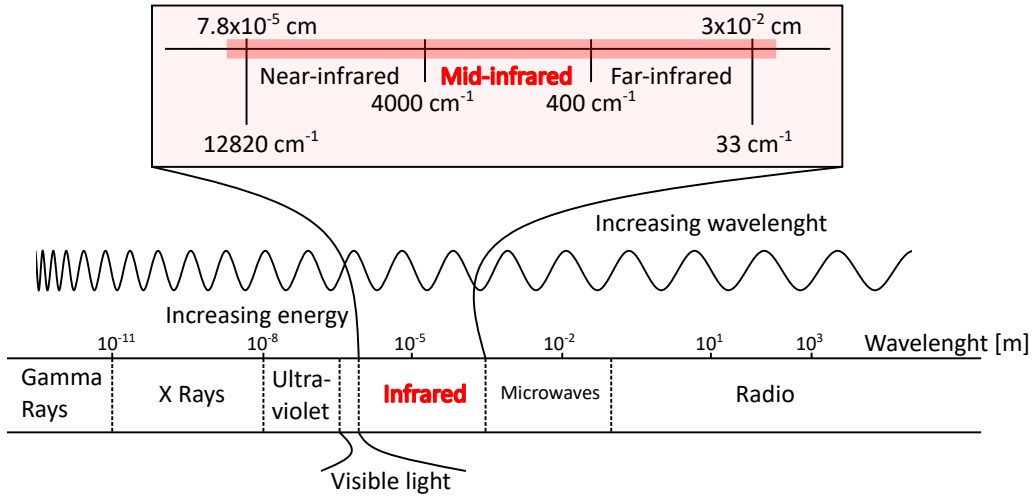


Figure 2.1: Infrared radiation is the radiation whose wavelength is between visible light and radio waves. In infrared spectroscopy, the infrared spectrum is divided into near-infrared (NIR), mid-infrared (MIR), and far-infrared (FIR). In material characterization, the study of vibrational states is mainly done in the MIR range.

of a material [33].
Now it is explaned how the atomic structure of a molecule is correlated with its infrared spectrum to understand how it is possible to extract some information about the composition of a sample from the absorption spectrum.

## 2.2 Theory background

### 2.2.1 Infrared Radiation

The infrared radiation indicates the portion of the electromagnetic radiation whose frequency is lower than visible light and higher than radio waves. In terms of wavenumber, the infrared radiation is located between 12820 and 33 $cm^{-1}$, while in energy terms the single photons have an energy between 1.6 $eV$ and 4 $meV$. Infrared spectra are generally associated with the radiated heat, indeed many of its uses concern applications in thermometry. However, in the field of material characterization, the study of infrared interaction with matter is a powerful tool used to investigate the composition of a sample. Since infrared covers an extensive portion of the spectrum in terms of frequencies, the spectrum has been further divided into sub-bands according to the areas of use (figure 2.1). In infrared spectroscopy, the IR spectrum is divided into three bands: far-infrared (FIR), mid-infrared (MIR), and near-infrared (NIR).

In the field of material characterization, the most studied band is the mid-infrared,

which includes wave numbers between 4000 and 400 $cm^{-1}$. This band is particularly interesting since it includes most of the fundamental energy levels of the vibrational modes of the molecules and, therefore, can be used to probe the presence of certain chemical bonds.
Recently, the NIR band is also starting to find its field of interest in materials science, especially for those applications where a deeper penetration depth than the mid-infrared is required. However, the absorption spectra in this region present characteristics that are much more complicated to interpret since they are related to the excitation of combined fundamentals states, so special deconvolution algorithms are required.

### 2.2.2 Interaction of infrared radiation with matter

Before Maxwell's theory of electromagnetism, not much was known about the physical nature of light, to the point that optics was considered a discipline unrelated to other areas of classical physics. Only some properties of light were known due to experimental evidence, among which the speed and the wave nature, without however knowing what the physical dimension of the oscillating field was.
Towards the end of the 19th century, in an attempt to unify the laws of electromagnetism under a single model, Maxwell predicted the existence of a new type of wave, the electromagnetic wave, whose velocity coincided with the velocity of light waves in vacuum. In a short time, it was understood that electromagnetic waves and light waves were de facto the same thing, finally reconnecting optics to the other areas of classical physics. However, several experimental observations continued to be misinterpreted even using Maxwell's theory.
One of the unsolved problems concerned the interaction of light with matter, which showed inconsistent behaviors with the classical theory. In this context, quantum theory was born, which sees the light composed of quasi-particles called photons. A photon is a quantum of electromagnetic radiation whose energy is proportional to the frequency of the corresponding electromagnetic wave.
In quantum theory, the light-matter interaction occurs through the absorption or emission of a photon which, depending on its energy, can involve different elements of matter, including atoms, molecules, or the whole crystal.
The infrared radiation energy depends on the wavenumber and mainly involves the vibrational states of matter, which can be single in isolated molecules (gas or liquids) or collective in the case of crystals (phonons).
The first step to understanding the origin of vibrational states is to see the atomic bonds within matter as a set of harmonic oscillators. In quantum theory, an oscillator has a discrete energy spectrum, whose energy levels have an energy proportional to the natural oscillation frequency of the oscillator. In this approximation, a molecule is then composed of a set of oscillators whose energy states define the vibrational spectrum of the molecule. Therefore, it is evident that, depending on the composition and structure

of a molecule, there will be an energetic spectrum of vibrational states that is more or less articulated, but in any case, composed of a finite number of states [33, 38].

### Vibration modes and selection rules

The vibrational states of a molecule can be calculated exactly using more or less sophisticated numerical methods; however, the number of vibrational modes can be derived simply from some considerations regarding the degrees of freedom of a molecule.
An atom can be approximated by a material point. In this approximation, each atom has three degrees of freedom. Then, a molecule composed of $N$ atoms in general terms will have a total of $3 \cdot N$ degrees of freedom [39]. To calculate the number of degrees of freedom corresponding to the number of vibrational modes, we consider the molecule as a whole. Like any three-dimensional object, a molecule can translate and rotate on itself. These movements constrain a certain number of degrees of freedom of the system, which will not be associated with oscillations. Since the total degrees of freedom of a molecule depend only on the number of atoms that compose it, the number of oscillation modes in a molecule is given by $N_{Vib.Modes} = 3N - T - R$, where $T$ and $R$ are the translational and rotational degrees of freedom of the molecule, respectively. The translational degrees of freedom of an isolated molecule are always three, while the rotational degrees of freedom depend on the molecule's structure. For example, we consider two different molecules: the molecular oxygen $O_2$ and the water molecule $H_2O$. A molecule of oxygen is a linear molecule made up of two atoms, so it has a total of 6 degrees of freedom. Three are translational, and 2 are rotational since $O_2$ has a linear structure. According to the calculation seen above, only one degree of vibrational freedom remains, indeed the only possible oscillation is made by the two oxygen atoms moving around the center of mass. On the other hand, a water molecule has 9 degrees of freedom, of which 3 are translational and 3 rotational. In this case, there are 3 degrees of freedom that are associated with independent oscillations, represented in Figure 2.2. At this point, we note that, although each oscillator has its own energy spectrum, not all oscillators can be excited by electromagnetic radiation, or more specifically, by infrared radiation.
In fact, electromagnetic radiation can interact only with states that have an electric dipole (permanent or momentary) other than zero, and in particular, a vibrational mode can be excited only if the displacement of the atoms modifies the intensity of the involved electric dipole [33]. This mechanism is due to the electrical nature of infrared radiation and defines the selection rules of a molecule for the absorption of infrared radiation.
In electrostatics, an electric dipole is composed of two equal and opposite electric charges, separated by a constant distance. The intensity of an electric dipole is defined by the dipole moment, a vector whose absolute value is given by the product of the module of the separated charge and the distance between the charges. There is a dipole moment in a molecule when it is composed of atoms with very different electronegativities, which tend to polarize the charges present in a certain direction. In these molecules, at least

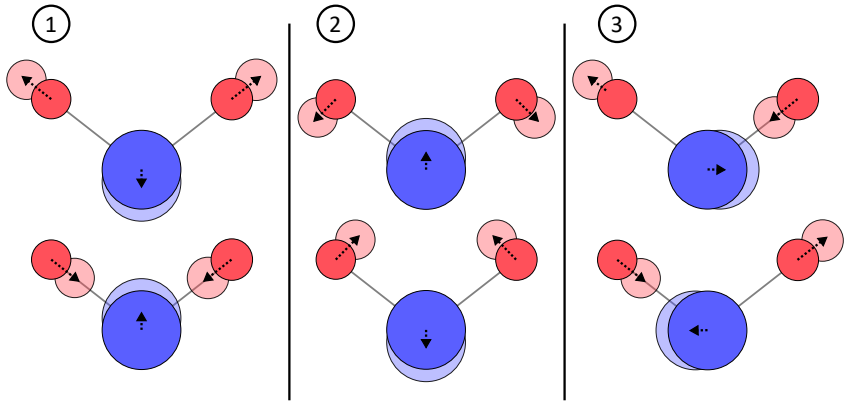


Figure 2.2: The figure shows the three independent vibrational modes of the water molecule. The arrows indicate for each oscillation the direction in which the different atoms move. Each vibrational mode has an independent energy spectrum, and as a whole, the set of all oscillation states and their linear combinations form the vibrational spectrum of the molecule. It is important to underline that each mode of vibration does not move the center of mass of the system, therefore in the water molecule, it is the hydrogen atoms that move with respect to the oxygen atom since it contains most of the mass of the molecule.

part of the vibrational modes will interact with the electromagnetic radiation, with an intensity depending on the strength of the electric dipole. For example, we consider again the molecules $O_2$, $H_2O$, and $CO_2$, understanding which of their vibrational modes interact with infrared radiation. Molecular oxygen has only one degree of vibrational freedom, which consists of the oscillation of the two oxygen atoms around the center of mass of the molecule. However, this type of oscillation, common to all homoatomic diatomic molecules, does not possess any dipole moment. Indeed the electric charge is equally distributed between the two oscillating atoms, and consequently, the molecular oxygen appears transparent to infrared radiation. The water molecule, on the other hand, is a polar molecule. In water, oxygen is negatively charged, while the two hydrogen atoms are positively charged. To understand the interaction of infrared radiation with water, one can analyze the three vibrational modes of water displayed in Figure 2.2. Every vibrational mode has an electrical dipole, therefore each mode can absorb photons at the frequency characteristic of their bonds, making water opaque to infrared radiation. Finally, we consider the carbon dioxide molecule ($CO_2$). Carbon dioxide is a linear molecule formed by two oxygens placed around a central carbon atom at a flat angle. Carbon dioxide has a null electric dipole, however, it is not transparent to infrared radiation.
To explain this apparent contradiction, we consider the four oscillation modes of the $CO_2$ molecule shown in Figure 2.3.

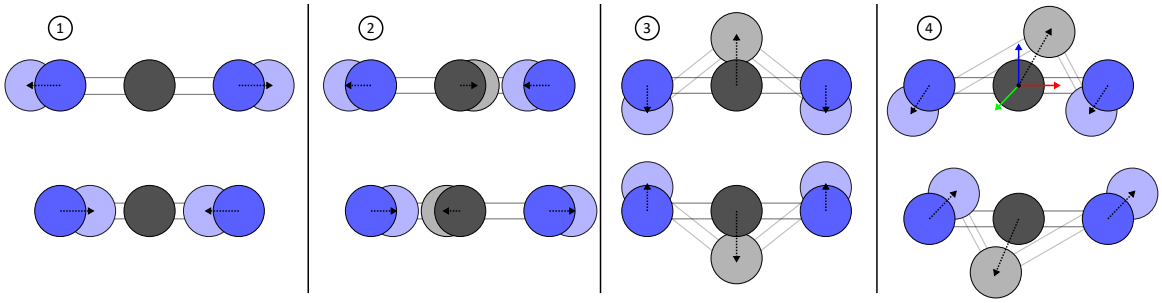


Figure 2.3: The figure shows the four modes of oscillation of the carbon dioxide molecule. Although at equilibrium, the $CO_2$ molecule has a null electric dipole, not all its oscillation modes are transparent to infrared radiation; we note indeed that the oscillation modes 2, 3, and 4 forms momentary electric dipoles during the oscillation and are therefore able to absorb the photons corresponding to their characteristic energy levels.

In the first case, the vibration of the oxygen atoms is symmetrical with respect to the central carbon atom. In this case, the dipole of the oscillator is always zero, then the first oscillation mode is inactive in the infrared. On the other hand, the other modes of vibration, although at equilibrium they have a null dipole, they form a momentary electric dipole during the oscillation. A momentary dipole can interact with infrared radiation, absorbing the energy of its characteristic oscillation state, and therefore the vibration modes 2, 3, and 4 are active in the infrared.
These systems are quite simple, however, as the complexity of a molecule increases, the complexity of its infrared absorption spectrum increases accordingly. Furthermore, a sample is generally composed of a mixture of several substances, consequently, the resulting spectrum will be the superposition of all the characteristic spectra of the molecules present.

### 2.2.3 Interpretation of the absorption spectrum

Once an infrared spectrum has been acquired, the next step is interpretation. Although the spectrum of a sample can also be very complex, there are some simplifications that simplify the assignment of bands to certain bonds, through known frequency groups [40, 33]. These groups are present in each range of the infrared spectrum (i.e., near, medium and far infrared), however the main ones, which correspond to the fundamental absorption frequencies, are in the medium infrared. This region is roughly divided into four ranges: the X−H stretching region ($4000 - 2500\ cm^{-1}$), the trible-bond region ($2500 - 2000\ cm^{-1}$) ), the double-bond region ($2000 - 1500\ cm^{-1}$) and the fingerprint region ($1500 - 600\ cm^{-}1$). The fundamental vibrations in the region $4000 - 2500\ cm^{-1}$ are typically due to the stretching of X−H bonds, in which $X$ can be an oxygen, carbon or nitrogen atom forming the bonds O−H, C−H and N−H respectively. These bonds

show characteristic features, and therefore allow to discriminate their type. An example are O−H bonds and N−H bonds, which respectively produce a broadband between $3500 - 3600\ cm^{-1}$ and a sharp band beethween $3400 - 3300\ cm^{-1}$.
Absorption due to triple bond stretching falls in the region between $2500 - 2000\ cm^{-1}$. The main bonds that can be discriminated in this region are C≡C and C≡N, but generally there are no particularly intense absorption peaks.
In the range $2000 - 1500\ cm^{-1}$ we find the bands associated with the double bonds, of which the principal is the streatchig carbonyle (C=O), which falls between $1830 - 1650\ cm^{-1}$ and forms one of most opaque bands of the entire infrared spectrum.
Finally we find the fingerprint region, compressed in the wavelength range between 1500−600 $cm^{-1}$. In this region there are many peaks, more or less intense depending on the structure and composition of a molecule. Compared to the other zones, in which is the single bonds that characterize an absorption bands, in this region, virtually equal bonds can lead to different absorption energies due to the influence of the molecular structure on the bond energies. The spectrum in this region is therefore characteristic of a molecule and for this reason it is known as its IR fingerprint.
Another factor affecting the absorption spectrum of a molecule is the type of solvent used (in the case of measurements in solution) which, through the formation of hydrogen bonds, modifies the absorption energy of a molecule . In conclusion, from a practical point of view, the steps to follow to approach the interpretation of a spectrum are:

1. Look for high wave number peaks $> 1500\ cm^{-1}$, focusing on the strongest bands.
2. Make a list of the possible bonds to the most intense bands.
3. Use the lower wavenumbers of the spectrum to confirm or discard some possibilities.
4. Don't expect to assign every band of a spectrum.
5. If possible, find confirmation of the experimental data in the spectra present in the literature.
6. Take advantage of both the presence and absence of specific peaks to accept or reject a hypothesis.
7. Carefully consider the relative strength of the bands as this can change considerably depending on the circumstances.
8. Take care when using small wavenumber changes. These can be influenced by whether the spectrum was run as a solid or liquid, or in solution. If in solution, some bands are very 'solvent-sensitive'.

## 2.3 Instrumentation

Traditionally the absorption spectrum of materials was obtained by measuring the absorption at single wavelengths in a spectral range of interest.
The first instruments that allowed these measurements were based on prisms or diffraction gratings, which decompose the individual spectral components coming from a light source with a continuous spectrum. In this way, it was possible to measure the absorption due to the single wavelength by rotating the grating or the prism with respect to the sample [41].
Despite the conceptual simplicity, these instruments presented a series of problems, first of all, the slowness of acquisition. Indeed, the intensity of the single component was only a minimal part of the overall intensity of the light source. Therefore, it was necessary to illuminate a sample for long periods to reduce the signal-to-noise ratio of every single measurement that composed the spectra. Furthermore, since each frequency was selected by physically moving a dispersive element, basically, the accuracy of the system depended on the precision of the positioning mechanism of the instrumentation.
Nowadays, almost every instrument measuring the absorption spectrum uses Fourier transform spectrometers, and instruments based on dispersive elements have almost completely disappeared. Fourier transform spectroscopy does not select the single wavelength but uses the entire incident light, appropriately modulating each frequency and then decomposes the individual components only later. From the experimental point of view, this approach has a series of advantages. Indeed, the effective intensity is much higher than in the previous case and increases the acquisition speed without decreasing the signal-to-noise ratio of the measurements (Jacquinot [42] and Fellgett [43] advantage). These properties have made Fourier transform spectroscopy one of the most popular techniques in optical spectroscopy, almost entirely replacing instrumentation based on dispersive elements.

### 2.3.1 Fourier-transform spectroscopy

Fourier transform spectroscopy is an optical spectroscopy technique that allows obtaining the absorption spectrum of a sample over a given spectral range by exploiting the properties of the Fourier transform applied to a particular experimental setup.
Depending on the range of the spectrum being analyzed, the parts that make up a spectrometer are different, however, the heart of all Fourier transform spectrometers is always an interferometer. There are different types of interferometers, however, currently the most used both for its reliability and for the performance it allows to obtain, is the Michelson interferometer.
Figure 2.4 shows the main elements that compose a Michelson interferometer in a Fourier transform spectrometer.

With reference to the Figure 2.4 the main elements are:

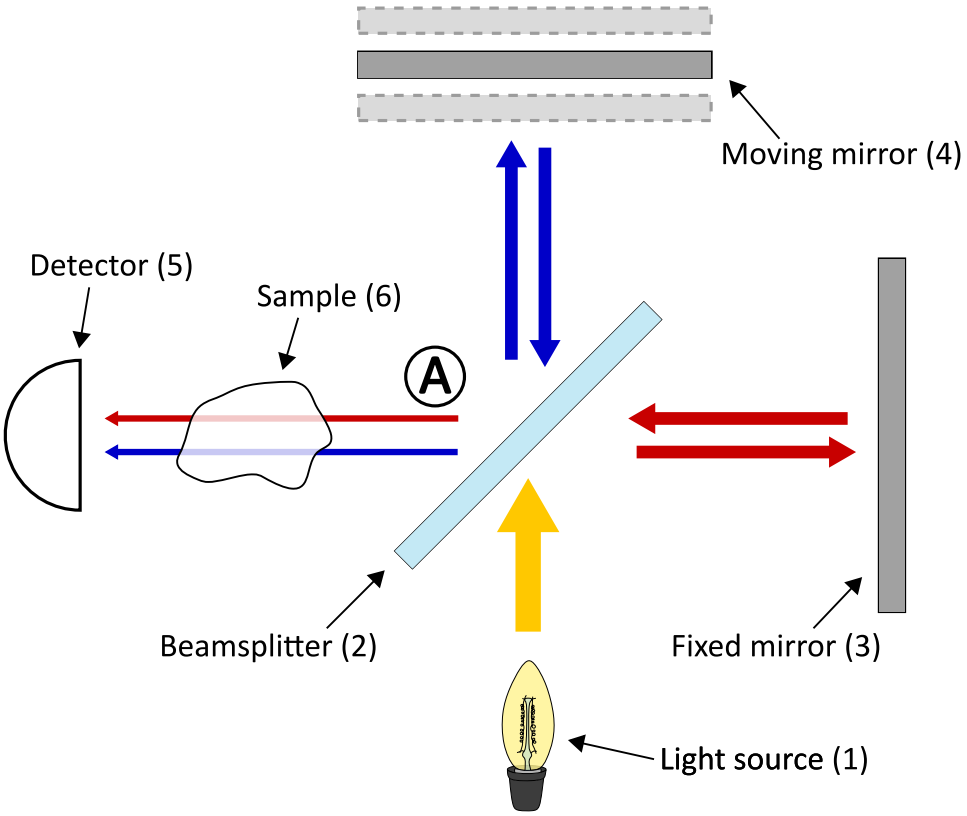


Figure 2.4: The figure resumes the working principle of a Michelson interferometer. The light from a source with continuous spectra is broken down and recomposed into a single beam using a beamsplitter. This beam is given by the sum of two components out of phase due to the different optical paths given by the moving mirror. When the beam leaves the interferometer, it is partially absorbed by the sample and measured by a detector. The signal collected by the detector, with the position of the moving mirror, allows the calculation of the interferogram, whose Fourier transform is shown to be proportional to the absorption spectrum of the sample.

1. A continuous spectrum light source that defines the testing spectral region.
2. A beamsplitter, which divides the light coming from the source in two beams of transmitted and reflected light, respectively.
3. A fixed mirror, which reflects the beam reflected by the beamsplitter.
4. A moving mirror, which reflects the beam transmitted by the beamsplitter.
5. A detector, chosen to be responsive in the spectral region emitted by the light source.
6. A specimen that is partially transparent to incident light.

Experimentally, the raw data extracted is the detector signal as a function of the position of the moving mirror.
Except for a constant, this curve is called the interferogram and has the remarkable property of being proportional to the Fourier transform of the absorption spectrum of the various elements that constitute the optical path of the light source.
At this point, it is possible to obtain the absorption spectrum of a sample, observing that the contribution of the elements that compose the optical path is constant and therefore can be compensated by measuring the spectrum at an empty instrument (background).
One can analyze in detail the operation of a Fourier transform spectrometer, demonstrating analytically that the interferogram matches the Fourier transform of the absorption spectrum.
First, we consider the light source: in a Fourier transform spectrometer, the source is composed of a continuous spectrum containing all the frequencies used to test a sample. To simplify the problem, we consider the single monochromatic plane wave emitted by the source. In general terms, a plane wave in space is described by the following expression:

$$E(\vec{x}, \vec{k}, \omega, t) = E_0(\omega) \exp\Big\{ i(\vec{k} \cdot \vec{x} - \omega t) \Big\} \tag{2.1}$$

where $E_0(\omega)$ is the amplitude of the wave, $\vec{k}$ is the wave vector, $\vec{x}$ is the vector position referred to the source, $\omega$ is the angular velocity, and $t$ is the time. The expression 2.1 describes a plane wave in the three-dimensional space. However, in the configuration in Figure 2.4, we are interested only in the positions along the optical path where the vector $\vec{x}$ is always parallel to the wave vector $\vec{k}$. On these points, remembering the relationship that links the modulus of the wave vector to the wave number ($k = 2\pi\bar{\nu}$), it is possible to simplify the expression 2.1, that becomes:

$$E(x, \bar{\nu}, \omega, t) = E_0(\bar{\nu}) \exp\{ i(2\pi\bar{\nu}d - \omega t) \} \tag{2.2}$$

where $d$ is the length of the optical path referred to the distances from the light source. We note that the expression 2.2 no longer contains vector quantities, indeed, since the

optical path can be parameterized along a straight line, the position vector can be written as a scalar where the zero corresponds to the position of the source.
Starting from the source, the single light component hits the beamsplitter as soon as it is emitted, dividing the beam into two components of transmitted light and reflected light, respectively.
These two components are addressed respectively to the fixed mirror and to the moving mirror in Figure 2.4, which in turn redirect them in the opposite direction towards the beamsplitter.
The light that comes from the mirrors, also in this case, is divided by the beamsplitter into two components. However, the useful light for the measurement is only that directed towards the sample, which in the case of an ideal beamsplitter is at most $\frac{1}{4}$ of the light emitted by the source.
One can consider the analytic expression that describes a monochromatic wave at the point $A$ in Figure 2.4. For the superposition principle, the wave of wave number $\bar{\nu}$ at this point is the overlap of the two waves coming from the mirrors:

$$E_A(\bar{\nu}, d_1, d_2, t) = E_0(\bar{\nu}) \cdot r(\bar{\nu}) \cdot t(\bar{\nu}) \cdot (\exp\{i(2\pi\bar{\nu}d_1 - \omega t)\} + \exp\{i(2\pi\bar{\nu}d_2 - \omega t)\}) \quad (2.3)$$

where $d_1$ and $d_2$ are the lengths of the optical paths traveled by the two waves and $t(\bar{\nu})$ and $r(\bar{\nu})$ are the transmission and reflection coefficients of the beamsplitter, respectively.
At this point, we consider that from the experimental point of view, it is not possible to directly measure the amplitude of a wave, while it is possible to measure its intensity. The intensity of a wave is given by its modulus squared, therefore in point A, the intensity is calculated as $I_A = E_A \cdot E_A^*$, where $E_A^*$ is the reciprocal complex of $E_A$. By making the appropriate simplifications, we thus obtain that the intensity at the point $A$ is given by the following expression:

$$I_A(\bar{\nu}, d_1, d_2, t) = 2E_0^2(\bar{\nu}) \cdot r(\bar{\nu}) \cdot t(\bar{\nu}) \cdot (1 + \cos 2\pi(d_2 - d_1)) \quad (2.4)$$

which, replacing $x = (d_2 - d_1)$ reduces to:

$$I_A(\bar{\nu}, x, t) = 2E_0^2(\bar{\nu}) \cdot r(\bar{\nu}) \cdot t(\bar{\nu}) \cdot (1 + \cos 2\pi x) \quad (2.5)$$

The substitution $x = (d_2 - d_1)$ is not a random simplification, indeed it corresponds to the displacement of the moving mirror with respect to the point where the two arms of the interferometer are identical.
Continuing along the optical path, from point $A$ the light first passes through the sample and then is collected by the detector. At this point the intensity corresponding to the single monochromatic wave measured by the detector becomes:

$$I(\bar{\nu}, x) = 2S(\bar{\nu}) \cdot D(\bar{\nu}) \cdot E_0^2(\bar{\nu}) \cdot r(\bar{\nu}) \cdot t(\bar{\nu}) \cdot (1 + \cos 2\pi\bar{\nu}x) \quad (2.6)$$

where $D(\nu)$ and $S(\nu)$ are respectively the detector's spectral response and the absorption of the sample.

However, the detector does not measure the single spectral component, but integrates the intensity over the entire spectrum, thus the measured signal is:

$$I(x) = \int_0^{+\infty} I_{det}(\bar{\nu}, x)d\bar{\nu} = \int_0^{+\infty} f(\bar{\nu}) \cdot (1 + \cos 2\pi\bar{\nu} \cdot x)d\bar{\nu} = \\ = \int_0^{+\infty} f(\bar{\nu})d\bar{\nu} + \int_0^{+\infty} f(\bar{\nu}) \cos 2\pi\bar{\nu}x \ d\bar{\nu} \quad (2.7)$$

where, to simplify the expression, we replaced $f(\bar{\nu}) = 2S(\bar{\nu}) \cdot D(\bar{\nu}) \cdot E_0^2(\bar{\nu}) \cdot r(\bar{\nu}) \cdot t(\bar{\nu})$.
In the equation 2.7 we observe that the integral $\int_0^{+\infty} f(\nu)d\bar{\nu}$ is equivalent to $\frac{I_0}{2}$, where $I_0$ is the intensity measured by the detector when the interference on all frequencies is constructive, that corresponds to the null displacement of the mirror.
By making this substitution the equation 2.7 simplifies further, becoming:

$$I(x) - \frac{I_0}{2} = \int_0^{+\infty} f(\bar{\nu}) \cos 2\pi\bar{\nu}x \ d\bar{\nu} \quad (2.8)$$

In Fourier transform spectroscopy, $I(x) - \frac{I_0}{2}$ is called interferogram and corresponds to the raw data obtained directly from the instrument. From the expression 2.8 it is easy to prove that the interferogram is an even function with respect to $x$. This observation is quite significant since even functions has the Fourier transform and the Fourier antitraform identical and given by:

$$\mathcal{F}_x f(t) = \frac{1}{\sqrt{2\pi}} \int_{\mathrm{Re}} f(t) \cdot \cos xt \ dt \quad (2.9)$$

$$\mathcal{F}_t^{-1} f(x) = \frac{1}{\sqrt{2\pi}} \int_{\mathrm{Re}} f(x) \cdot \cos xt \ dx \quad (2.10)$$

We now replace the expression $\nu = \frac{\bar{\nu}}{2\pi}$ in the 2.8 equation. The resulting equation is exactly the Fourier transform of the function $f(\nu)$, and this, therefore, demonstrates that the Fourier antitransform of the interferogram actually corresponds to the absorption spectrum of the elements along the optical path.

### 2.3.2 Fourier transform infrared spectroscopy (FTIR) setup

Fourier transform infrared spectroscopy (FTIR) is a specific Fourier transform spectroscopy technique for measuring measurements in the infrared spectrum. In FTIR spectrometer, we find all the elements of a Fourier transform spectrometer described in the previous paragraph, optimized to work in the infrared radiation range (i.e., 12820 e 33 $cm^{-1}$).
The Figure 2.5 shows the typical structure of an FTIR spectrometer, highlighting the main elements.

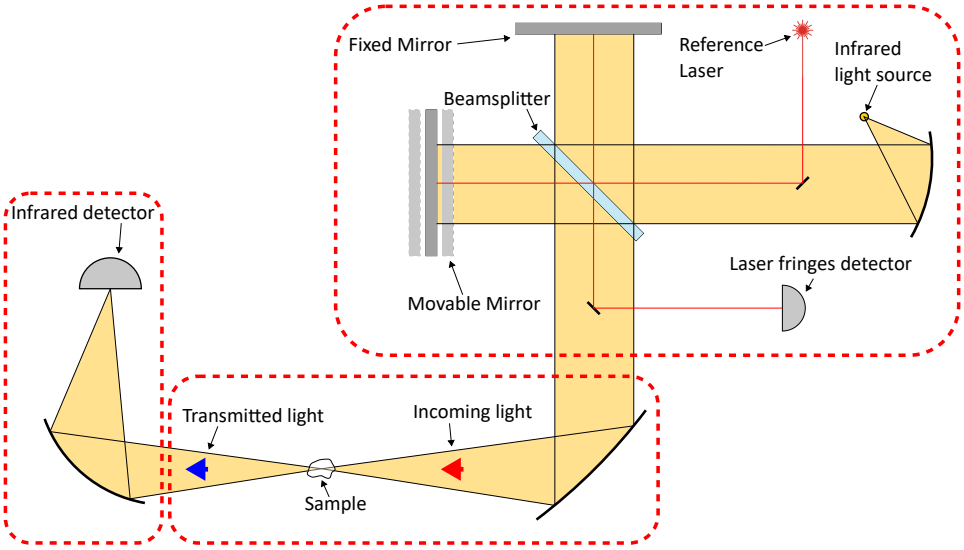


Figure 2.5: The figure shows the structure of a modern FTIR instrumentation. Generally, the instrument is divided into three separated environments: Michelson's interferometer, measurement chamber, and detector. Compared to the scheme in Figure 2.4, it is also the highlighted the laser and the photodiode used to measure the displacement of the moving mirror.

The instrument's heart is a Michelson interferometer, whose operation has been fully described in the previous paragraph. In addition to the elements already described in figure 2.4 we can observe a laser and a photodiode positioned at the input and output of the interferometer, respectively. These two elements are used to measure the relative displacement of the moving mirror with respect to the fixed mirror since this quantity is fundamental for calculating the interferogram.
According to the equation 2.8, the intensity of a monochromatic wave is modulated at the interferometer's output by a cosine, whose periodicity with respect to the distance between the mirrors is inversely proportional to the wavelength of the laser.
By exploiting this relationship, it is possible to correlate the relative position of the moving mirror to the maximum and minimum intensity measured by the photodiode. In this way, a very accurate measurement of the distance between the mirrors is obtained, known as Connes advantage [44], with absolute precision in the case of a $He - Ne$ laser of $\lambda/4 = 0.16\mu m$.
In a FTIR setup, the first element that defines the measurement range is the source. Generally, an incandescent filament is used, whose temperature is modulated according to the range of interest. The factor that most influences the choice of the source, besides the absolute intensity, is the stability of the emitted light. Indeed, all the considerations made in the previous paragraphs require that the intensity of the light source is constant

over time so that the contribution due to the amplitude of the incident wave does not interfere with the modulation made by the movement of the interferometer mirror. However, it is not sufficient for the source to be constant during the time af a single spectrum acquisistion: the source must remain constant even between consecutive measurements. Indeed, remember that the absorption spectrum of a material is always referred to the measurement of the background of the instrument; consequently, the intensity of the source during the acquisition of the background must be the same as that used for subsequent measurements, otherwise, the absorption of material will be distorted by the change in intensity of the source itself.
The sources most used in infrared spectroscopy are made of $SiC$ or in incandescent tungsten filament.
The second thing to consider is the beamsplitter. The beamsplitter divides the beam into two components that are ideally identical to each other over the entire spectral range. Generally, the beamsplitters used in an infrared setup consist of a material transparent to infrared radiation (e.g., Potassium Bromide ($KBr$), Zinc Selenide ($ZnSe$), etc.) on whose surface a partially reflective coating is deposited (e.g., iron oxide $Fe_2O_3$, silicon (Si), germanium (Ge), etc.). By doing this, the refractive indices are optimized so that the incident radiation is divided into two orthogonal beams of approximately identical intensity.
The third element to define the measurement range in a FTIR setup is the detector [33]. In addition to being very sensitive over the entire measuring range, an ideal detector needs to be very responsive. Indeed, as in the case of the source, the response of the detector in the theoretical treatment described in the previous section was considered independent of time. However, there is always a delay in the response of the detector that, depending on the technology used, is more or less important. Consequently, in addition to sensitivity, it is important to consider the response time, which eventually limits the scanning speed of the interferometer. The main detectors used are of three types: thermal, pyroelectric, and photoelectric. Thermal detectors (i.e., bolometers and thermopiles) are conceptually quite simple devices, indeed they correlate the temperature of a metal element (e.g., an extremely thin wire or a thermocouple) to the intensity of the incident light. This type of approach has several advantages, including a very high and flat sensitivity over a wide range of frequencies, but it has the drawback of having a rather long response time, and for this reason, thermal detectors are almost no longer used in modern instrumentation.
Pyroelectric detectors exploit the pyroelectricity of some materials (e.g., triglycerine sulphate) to measure the intensity of the incident light. A pyroelectric material is an electrical insulator that has the property of accumulating surface charges when heated or cooled. Experimentally this effect is observed through a rapid variation of electric potential at the ends of a suitable circuit, proportional to the intensity of the incident light. Ultimately, as thermal detectors, a pyroelectric exploits the temperature variation induced by the incident light. However, it has the advantage of having a much faster

response. Indeed, a pyroelectric sensor is intrinsically dependent on the time derivative of the temperature and not on its absolute value. This property means that pyroelectric sensors are widely used, especially for those applications where very high sensitivity is not required.
Compared to thermal and pyroelectric sensors, photoelectric detectors exploit the property of some semiconductor materials to change resistivity when illuminated. Photoelectric detectors, such as mercury-cadimo-tellurium (MCT), consist of a film of semiconductor material deposited on a glass surface when a photon hits the detector, its conductivity changes, which is monitored by an appropriate measuring circuit. in addition to not having a flat response on the whole spectrum, one of the main disadvantages of these detectors, is that they require to be cooled at very low temperatures. For this reason, they are generally provided encapsulated in high vacuum to avoid condensation during the cooling and coupled with a liquid nitrogen dewar. Despite these problems, photoelectric are among the most used detectors in modern instrumentation, in fact they have an extremely high sensitivity over a wide range of infrared radiation and extremely fast response times that allow very rapid scans of the interferometer.

### Diffuse reflectance infrared Fourier Transform (DRIFT)

There are different configurations with which FTIR measurements can be carried out. The simplest from the conceptual point of view is the transmission configuration, in which the light of the light source completely crosses the sample to characterize. This configuration can be used in liquid, gas, and solid phase and is one of the most used techniques since it allows to obtain quantitative measurements on the composition of a sample [45]. Despite the versatility of this technique, there are other configurations developed specifically to analyze some types of samples. One of these techniques is diffuse infrared reflectance Fourier transform (DRIFT), in which instead of measuring the transmitted light, it is acquired the light scattered from a sample [33]. This technique exploits the same instrumentation described in the previous section and is particularly suitable for the characterization of powders since, in this case, the diffused light is maximized. Furthermore, it is a technique particularly sensitive to the surface composition of a material and suitable for measuring the concentration of molecules adsorbed on the surface of nanoparticles.
The Figure 2.6 shows the interaction mechanism of light with a powders sample in a DRIFT configuration. Scattered light can be decomposed into two components: specularly reflected light and diffused light. The diffuse light component is related, for the most part, to multiple reflections within the sample and along its path and is partially absorbed by the surface layer of the particles. The light reflected specularly instead is due for the most part to direct reflections on the surface, and therefore, its spectrum substantially coincides with the spectrum of the incident light.
The specularly reflected light component is generally very bright. However, it appears

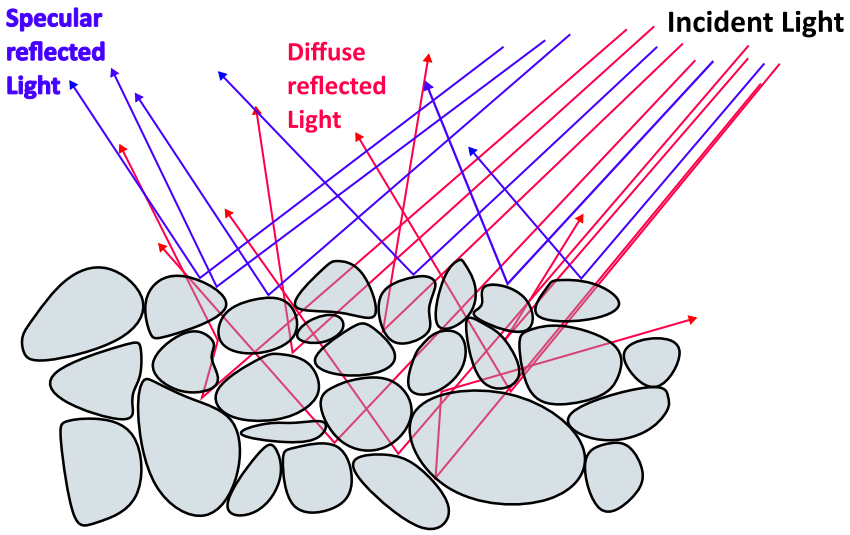


Figure 2.6: In a DRIFT measurement, light is focused on the surface of a sample made of powders. The re-emitted light is divided into specularly reflected light and diffused light that is addressed in every direction. The scattered light has been partially absorbed and therefore contains information about the absorption spectrum of the sample.

evident that the absorption spectrum of a material is contained only in the diffused light since it is the light that has interacted. The Figure 2.7 shows the optical scheme, seen from above, of the DRIFT Praying Mantis accessory, designed to interface directly to a FTIR instrumentation organized according to the scheme in Figure 2.5. The accessory is composed of two elliptical mirrors arranged so that one of the two foci coincides on the sample surface. The elliptical mirrors have the purpose of translating the focus of the instrument, focusing the light of the source on the sample, and at the same time collecting the diffused light to be directed to the detector.
Compared to other DRIFT accessories, this configuration has the advantage of discarding the specularly reflected component simply using the geometry with which the mirrors are arranged. In this way, only the diffused light is collected by the detector, which carries information about the absorption spectrum of the tested sample.
There are other types of accessories for carrying out DRIFT measurements, in which the specular component is rejected with the use of mechanical shutters. However, the described configuration offers the advantage of having the sample mechanically isolated. This feature is handy if it is necessary to couple a DRIFT measurement with other *in-situ* measurements, requiring the addition of external components. An example is a setup for *operando* measurements on chemiresistive gas sensors described in the next chapters.

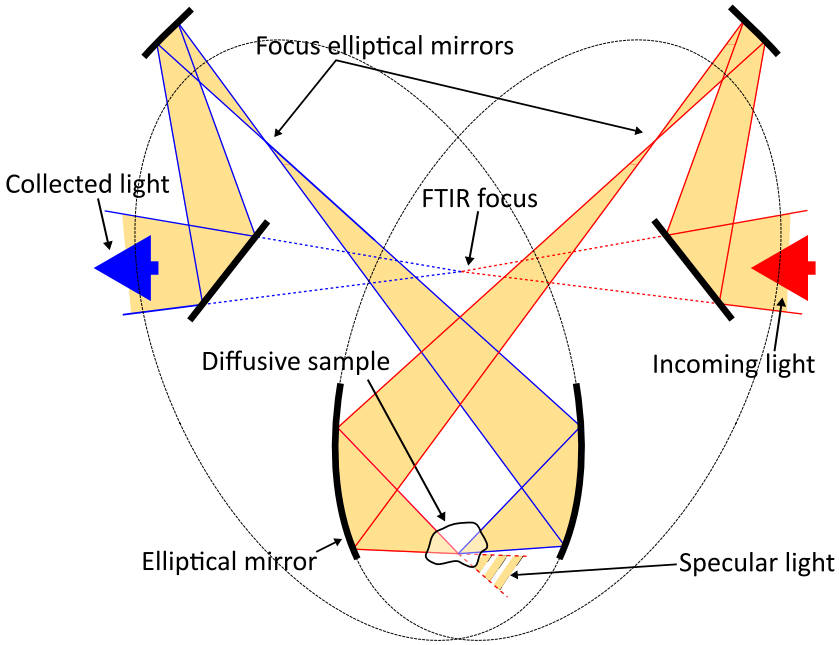


Figure 2.7: The figure shows the arrangement of the optics of a DRIFT accessory that can be integrated with an FTIR instrumentation of the type shown in Figure 2.5. Two elliptical mirrors are arranged to focus the input beam on the sample surface and refocus the scattered light on the detector, discarding at the same time the specular reflected light.

### DRIFT measurement on chemiresistive gas sensor *in operando*

As seen in section 1.3.1, a chemoresistive gas sensor changes its conductivity when the atmosphere's composition to which it is exposed changes. From the chemical point of view, the modification of the electrical properties is given by the absorption or desorption of certain species, caused by chemical-physical reactions catalyzed on the surface of the sensing material on which the sensor is based.
In a bulk material, the effects induced by a variation of the adsorbed species are generally negligible, however, in nanostructured materials, the situation changes. Porous materials are an example, such as silica gel, in which the surface area is sufficiently large to adsorb macroscopic quantities of water vapor. In the nanostructured powders used for the fabrication of chemiresistive gas sensors, a similar mechanism occurs on a smaller scale, in which the area-volume ratio of the particles amplifies the macroscopic effects of the surface-gas interaction. The concentration of the adsorbed species on the sensing film of a gas sensor is then much higher than in the bulk material, and with a sufficiently sensitive system, it is possible to estimate it through infrared spectroscopy.
The most suitable spectroscopic technique for this type of measurement is DRIFT spectroscopy, having been specially developed to characterize powders and being particularly sensitive to the surface composition of a sample.
Using the DRIFT spectroscopy, it is possible to measure the concentration of the adsorbed species experimentally and at the same time investigate the reaction mechanisms catalyzed on the surface. On the surface, reactions are often favored through a series of sub-reactions that make the kinetics of a process faster, and through infrared spectroscopy, it is possible to demonstrate every step by measuring the presence of the absorption peaks corresponding to the intermediate reaction products.
As an example, we can consider the sensing mechanism of metal oxides, which was summarized in section 1.3.1, focusing on the sensing mechanism of tin oxide for carbon monoxide. This is a reducing gas and is prone to oxidize into carbon dioxide ($CO_2$), consuming the oxygen adsorbed on the tin oxide surface. By acquiring the absorption spectrum of a working $SnO_2$ sensor in a DRIFT setup, it was possible to observe the carbon dioxide peaks growing at the expense of the absorption peaks of the oxygen bounded on the surface. These measurements allow us to demonstrate the oxidation reaction catalyzed on the tin oxide surface due to the presence of the adsorbed oxygen.
Other relevant examples concern thermo-desorption measures, in which the desorption of adsorbed species is measured as a function of the temperature or thermo-activated reaction, such as the *in-situ* oxidation of silicon carbide reported in chapter 4. In conclusion, measuring the absorption spectrum of *operando* gas sensor, although qualitatively, provides a further tool to investigate the surface chemistry of new material in working conditions, which is fundamental for the development of a solid theory on the sensing mechanism of new materials.

# Chapter 3

# Design of the *operando* DRIFT setup

## 3.1 Introduction

In the previous chapters, the fundamental role played by surface reactions in modeling the sensing mechanisms of a chemiresistive gas sensor was introduced. Specifically, it has been described the gas detection mechanism that takes place on sensors based on metal oxides, in which the concentration of the different adsorbed species causes a rearrangement of the energy bands that can be measured through a conductivity measurement. Therefore, the direct measurement of the concentration and nature of the adsorbed species in a chemiresistive gas sensor is a fundamental step to experimentally demonstrate the gas sensing properties of a material, thanks to which, by making the appropriate modifications, it is possible to improve the overall performance of a device rationally. Among the characterization tools available to evaluate adsorbed species, FTIR spectroscopy and DRIFT setups have been known for a long time to investigate surface chemistry and surface reactivity of submicron-sized particles. This technique is particularly well-suited to studying nanosized particles, either as loose powders or deposited as a film, because their high surface-to-bulk ratio contributes to the surface species quite significant in infrared adsorption. For these reasons, FTIR spectroscopy equipped with DRIFT setups has become particularly attractive to monitor the chemical reactions at the surface of a semiconducting chemical sensor under different environmental conditions (temperature, atmosphere, etc.) [46]. However, to perform *operando* measurements on chemiresistive gas sensors, a FTIR setup has to consider many issues. Indeed, the testing chamber itself influences most chemical/physical processes occurring at the sensor film surface, modifying the device's behavior in terms of stability, sensitivity, and reliability [47]. Furthermore, one has to consider that the amount of sensing material in a sensor is minimal. For example, a porous sensing layer produced in our laboratory has an active

area of $\sim 1\ mm^2$ and about $20 - 30\ \mu m$ thick, and these limited dimensions require high-performance spectroscopic methods coupled with a precision alignment system to obtain reliable and repeatable measurements. Various cells for *in situ* and *operando* spectroscopy have been developed over the years, however, efforts from a few research groups have been devoted to developing an optimized chemiresistive gas sensor testing chamber [48, 49, 50, 51]. Thus, a reliable sensing chamber must meet some basic requirements: it must be able to read out the sensor as well as to heat the film, the electrical connections for the sensing electrodes and the heating element should not interfere with the simultaneous spectroscopic characterization, and the cell must allow *in situ* treatments and high-temperature spectroscopy measurements in controllable gas atmospheres. This section reports the design, fabrication, modeling, and validation of a new low void-volume gas sensing system that is easy to use and maintain. The system is fully compatible with Harrick Scientific's mirror optics, can be employed with solid-state gas sensors with an operating temperature of up to 800 °C and it is equipped with a precision stage for the alignment of the sample.

## 3.2 Logical Design

In Figure 3.1 is described the overall logic structure of the setup designed to perform *operando* DRIFT measurements on chemiresistive gas sensors.

The setup couples two separate systems dedicated to carry out spectroscopic measurements on the sensing film and electrically characterizing the devices in controlled thermodynamic conditions. The point of union between the two systems is the chamber in which the measurements take place. Indeed, the measuring chamber is structured to interface both the DRIFT setup for infrared spectroscopy measurements and at the same time electrically characterize the sensor mounted on TO-39.
Going into detail, with reference to the Figure 3.1, the main elements that compose the setup are:

1. FTIR instrumentation, equipped with DRIFT accessory for the analysis of the infrared spectrum.

2. System for controlling the atmosphere inside the measurement chamber, consisting of an array of programmable mass-flow controllers (MFC) linked with gas cylinders and a controller.

3. Instrumentation to characterize a gas sensor and at the same time set the thermodynamic conditions of measurement.

4. Measurement chamber for the physical positioning of the sensor, equipped with devices for controlling the working atmosphere.

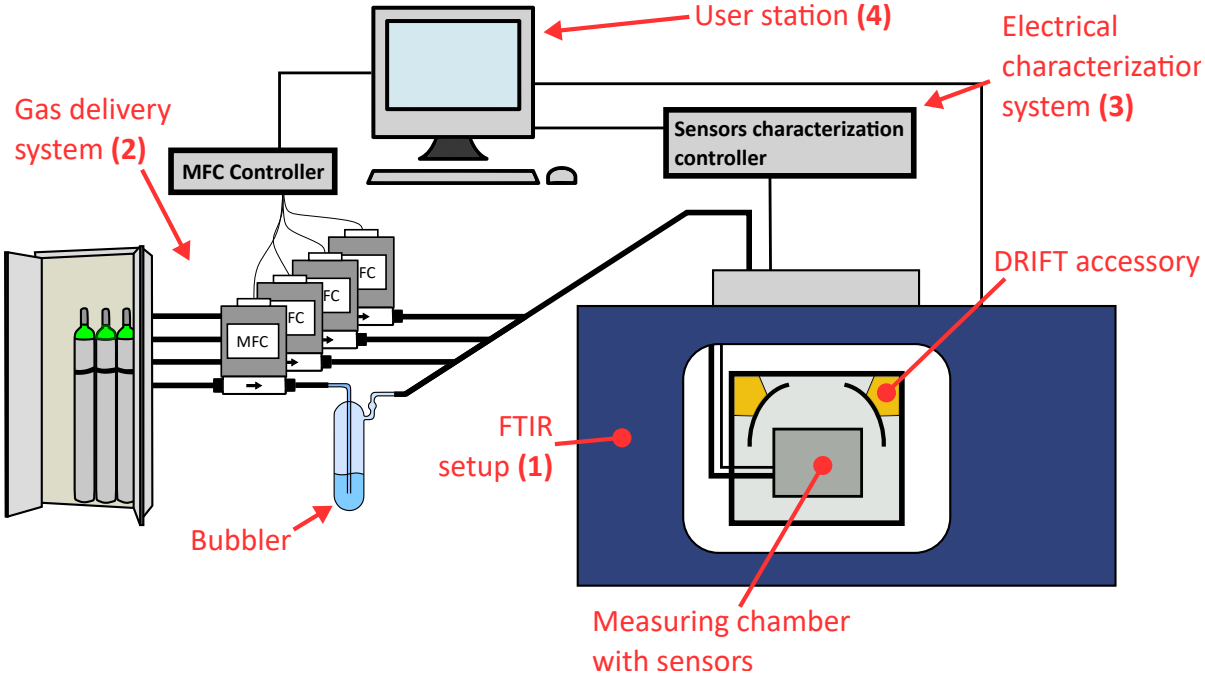


Figure 3.1: The figure shows the main elements of the *in operando* DRIFT setup. The system integrates the elements to electrically characterize a gas sensor under controlled thermodynamic conditions (i.e., known atmosphere and working temperature) and monitor its DRIFT spectrum.

5. Computer (user station), which coordinates the various modules and allows to use the system as a whole.

Each of these elements is divided into other parts, which will be described in detail in the following paragraphs, focusing on the strategies used to solve the various issues.

## 3.3 FTIR and DRIFT setup

The setup described in Figure 3.1 uses a *FTIR Vertex V70* infrared spectrometer from *Brucker* equipped with a mercury-cadmium-telluride (MCT) detector. The system includes the *DRIFT praying Mantis* accessory by *Harrick Scientific*, and the choice of all elements (e.g., source, detector, etc.) and all optics (e.g., mirrors, windows, etc.) was fitted to work in the wavelength range between $800 - 4000\ cm^{-1}$ (MIR). The structure of the spectrometer is similar to that described in Figure 2.5, in which the various environments are organized into three areas, separated and sealed from each other:

- the optical bench, which contains the Michelson interferometer, the light source, and the acquisition and calculation unit,

- the detector chamber, which contains the detector with the dewar for liquid nitrogen cooling and the respective focusing optics,
- the measurement chamber, where the DRIFT accessory is included, whose optical scheme is described in Figure 2.7, inside which the measurement chamber of the gas sensors is housed.

All three zones are kept in a dynamic vacuum of $\sim 10^{-3}$ *mbar* during the measurements to minimize the interference in the absorption spectra due to carbon dioxide $CO_2$ and water vapor $H_2O$ normally present in the atmosphere.

## 3.4 Mechanical design of the measuring chamber

The measurement chamber is the union point between spectroscopic measurements and the electrical characterization of chemiresistive gas sensors. From a practical point of view, the design of the measuring chamber mechanics was constrained above all by the geometry of the optics of the DRIFT Praying Mantis accessory, which allows a limited free space and on which the entire project is adapted.
Another design constraint was given by the need to include a system for alignment on the three axes of the sensor under test. In fact, since the measurement area on the sensor is minimal, an accurate centering system is crucial. Figure 3.2 shows the drawing (left) and the explosion view of the measuring chamber designed for *operando* experiments.

The equipment is divided into six main parts. Starting from the bottom,:

1. a vacuum compatible precision XY micro-stage (Standa),
2. a bracket, to mount the system on the micrometric positioning axis of the DRIFT accessory,
3. an electrical board, used both for mounting the temperature and humidity sensor inside the chamber and for extracting the electrical signals from the gas sensor under test, keeping the environment sealed,
4. the main body of the chamber, on which the connectors for the inlet of the gases are mounted laterally,
5. an adapter that allows correct sizing and positioning of the dome to the part 4,
6. a dome, equipped with two monolithic ZnSe windows for the passage of the IR beam and a window in $SiO_2$ for visual alignment,

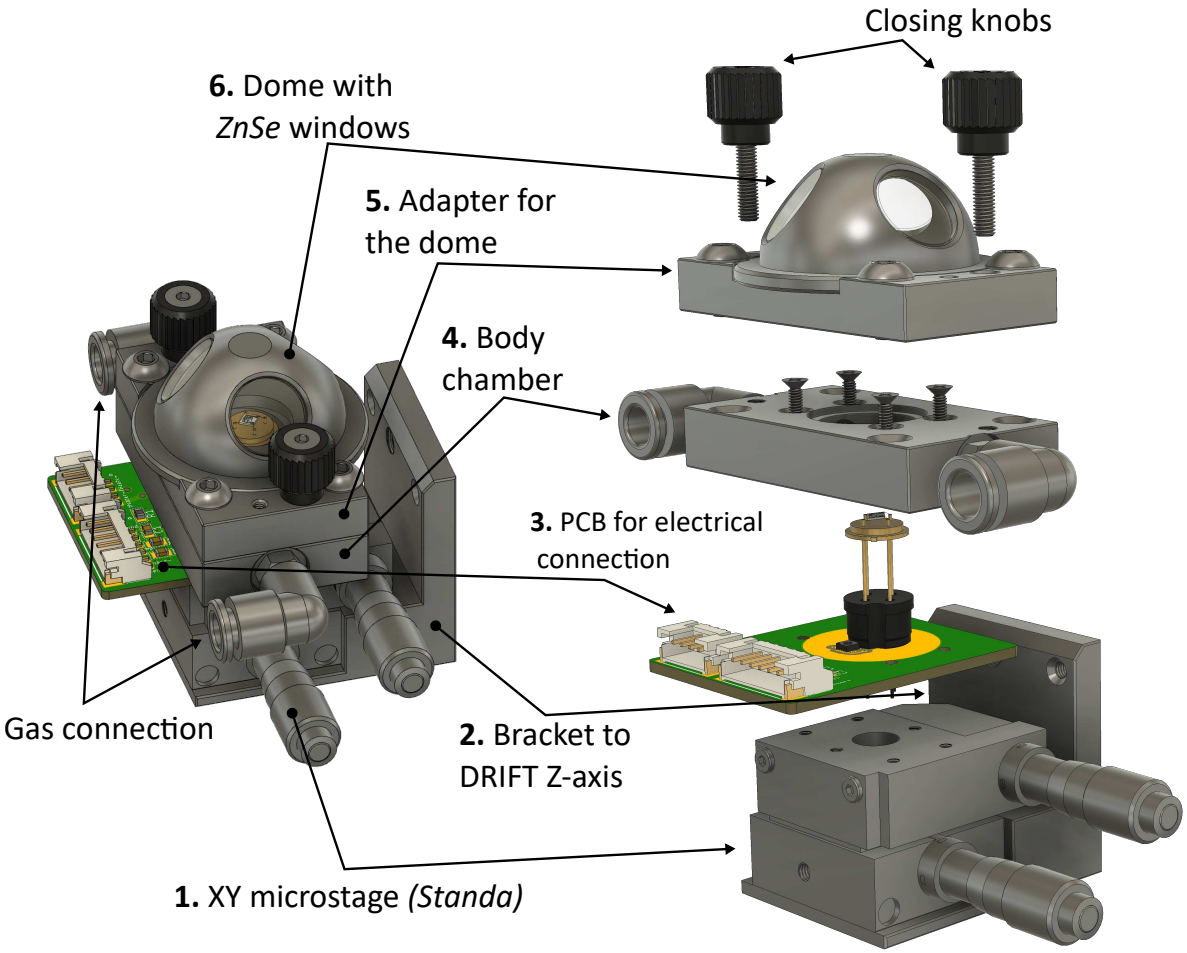


Figure 3.2: Drawing (left) and exploded view (right) of the measuring chamber. In the exploded view, the dome with the windows in $ZnSe$ (transparent in the infrared) is kept mounted together with piece *5* since together, they form the "lid" of the chamber.

All components inside the chamber that are in contact with the testing atmosphere are made of corrosion-resistant 316L stainless steel (SS) to avoid interactions with the gases being analyzed, while the metal parts of the electronic board inside the chamber are covered with a standard gold finish (ENIG finish).
The seal is made using three *Viton* o-rings placed respectively between the PCB (3) and the main body (4), between the main body and the adapter (5), and between the adapter and the dome (6). The chamber is mounted on the XY micro-stage (1), which coupled with the already present Z-axis in the Harrick's Praying Mantis, complete a precise 3 axes alignment stage with a range of 4 millimeters on all axes. The chamber has been developed in two successive versions, which differ mainly in the ease of use and assembly.

Additional information and the schematics can be found in Appendix C. The prototyping and optimization of the geometry of the various components of the measuring chamber were done using 3D printing, detailed in the Appendix A.

### 3.4.1 Fluid dynamics analysis

To evaluate the fluid dynamic characteristics within the operando chamber, a Computational Fluid Dynamic (CFD) simulation with airflow under isothermal conditions (25 °C) was performed based on Navier-Stokes equations [52]. These equations were solved using a finite element approach with a segregated solver by setting a specific flow rate at the chamber's inlet. The numerical simulations were performed with *Autodesk CFD* using the previously described *3D* model shown in Figure 3.2.
Moreover, evaluation of the chamber's Residence Time Distribution (RTD) was performed using a tracer stepped response technique, reported by [53, 54]. In this technique, humid air mixed with synthetic air is used as a tracer, which is injected in the chamber, and then the monitoring of $RH\%$ is carried out by using a humidity sensor inside the chamber. From the monitor of the humidity, it is possible to extract a concentration profile $C(t)$ that is proportional of the cumulative distribution function (CDF), $F(t)$. To evaluate the CDF, the concentration profile needs to be normalized to 1:

$$F(t) = \frac{C(t) - C_{initial}}{C_{final}} \tag{3.1}$$

where $C_{initial}$ and $C_{final}$ are the initial and final tracer concentrations. Since in our case, the initial tracer concentration is 0 $RH\%$ in pure dry air, the equation is simplified in:

$$F(t) = \frac{C(t)}{C_{final}} \tag{3.2}$$

At this point, it is possible to evaluate the variation of the CDF ($E(t)$) from experimental data as follows:

$$E(t) = \frac{dF(t)}{dt} \tag{3.3}$$

## 3.5 Gas delivery system

The gas feed system consists of four calibrated mass-flow controllers (MFC) (Brooks, SLA5800) and a secondary electronics control module (Brooks, 0260) for the delivery of constant gas flow to the measurement chamber through 6 mm PTFE tubing. Humidity control inside the chamber is obtained by a dedicated MFC fluxing certified synthetic air (20% $O_2$ and 80% $N_2$) through a bubbler filled with deionized water. All the system

is controlled by a custom LabView software and can work as a stand-alone system, operating both in manual and in programmed mode [55]. In manual mode, the user directly sets the working atmosphere in the measuring chamber, controlling gases flowing from every MFC. In programmed mode, the software runs a macro that sets different atmospheres at times specified by the user. To prevent any leakage from the MFC that could interfere with very low concentration measurement, every flowmeter is connected in series with an electro valve that closes the mass-flow controllers when they are set to zero. The control of the electro valves is integrated with the LabVIEW program that controls the MFC, so that their operation is synchronized with the user input.

## 3.6 Electronics design

This section presents the design and the validation of the measuring instrumentation developed to characterize chemiresistive *operando* gas sensors in the DRIFT setup. The equipment, described in depth both as hardware and as software, was designed to monitor the electrical behavior of gas sensors in controlled thermodynamic conditions. The main goal of this setup is to synchronize the electrical characterization with different measuring conditions, i.e., operating temperature, relative humidity, and gas target concentration. This operation allows automating various measurement protocols, otherwise impossible to obtain manually. In particular, this instrumentation permits to correlate the response of a chemiresistive gas sensor to the applied voltage, to its working temperature, and the gas concentration, automating the acquisition of the current-voltage (I-V) characteristic and the current-temperature (I-T) characteristic (Arrhenius plot) of sensing films. The experimental setup was validated by reporting the electrical characterization of a standard metal-oxide-based gas sensing material, such as $SnO_2$, working in different thermodynamic conditions.

### 3.6.1 Introduction

Despite the great attention dedicated to the study of new materials for gas sensing, no particular effort has been made to develop dedicated instrumentation to perform an effective electrical characterization of chemiresistive sensors. The current instrumentation developments mainly focus on decreasing energy consumption, as required by promising fields of application, such as the Internet of Things (IoT), where low-powered and minimal electronics are mandatory [56, 57]. For this reason, the performance of a chemiresistive gas sensor is usually evaluated using compact solutions, such as a generic ohmmeter, calibrated to operate in the resistance range of the used sensor [58]. However, depending on the employed sensing materials, various adjustments are required to perform accurate measurements. First of all, most semiconductor-based gas sensors do not operate properly at room temperature (RT). Indeed, these sensing materials have to be thermally

activated to make the gas detection process at the surface reversible [26]. Then, it is necessary to develop a system that provides optimal control of the working temperature of the sensors. It is also important to consider that chemiresistive gas sensors do not behave as ideal resistors. Specifically, it is observed that the applied potential influences the resistance value of the sensing film, then a configuration that fixes the voltage drop on the sensor has to be employed. These needs are usually accomplished using at least two programmable Source Measure Units (SMU): one to control the working temperature of the sensor and one to carry out the resistance measurement of the sensing film [59].
The usage of certified instrumentation represents the standard solution regarding the electrical characterizations of new devices. However, a more flexible, portable, and cost-effective solution has to be developed in the perspective of any practical usage of semiconducting gas sensors. For this reason, we have designed a dedicated instrumentation that joins all the necessary electronics in single hardware, maintaining a measurement accuracy and a dynamic range comparable to certified instruments. The presented hardware is controlled with custom software developed in Java that allows the user to set every measuring parameter (i.e., a sensor working temperature and its applied voltage) and to monitor any relevant quantity, such as the current working temperature, the applied voltage, the current passing through the sensing film, the resistance of the sensing film, and the measuring chamber parameters, i.e., temperature and relative humidity (RH%).
Moreover, some articulated characterizations are difficult to be directly managed by the user, especially because these require many days to be carried out. Then, one of the goals of this work was to develop instrumentation that allows automating these characterizations, reducing the measurement time and improving the accuracy, simultaneously. In particular, we provided a system that allows performing both electrical and thermoelectric measurements automatically employing the current-voltage (I-V) and current-temperature (I-T) characteristics.
To validate the instrumentation, we report the characterization of thick-film tin oxide ($SnO_2$) based sensor exposed to different conditions in a variable atmosphere of carbon monoxide. $SnO_2$ is a long and deeply studied material, then it was considered particularly suitable to evaluate the performance of such new instrumentation [26].
Figure 3.3 reports the scheme of the measurement setup, composed of hardware and software.

The hardware is divided into three main parts:

1. Gas delivery system, already described in section 3.5.
2. Temperature control, to set the temperature of the sensors.
3. Electrical characterization system, to monitor the electrical properties of the sensors.

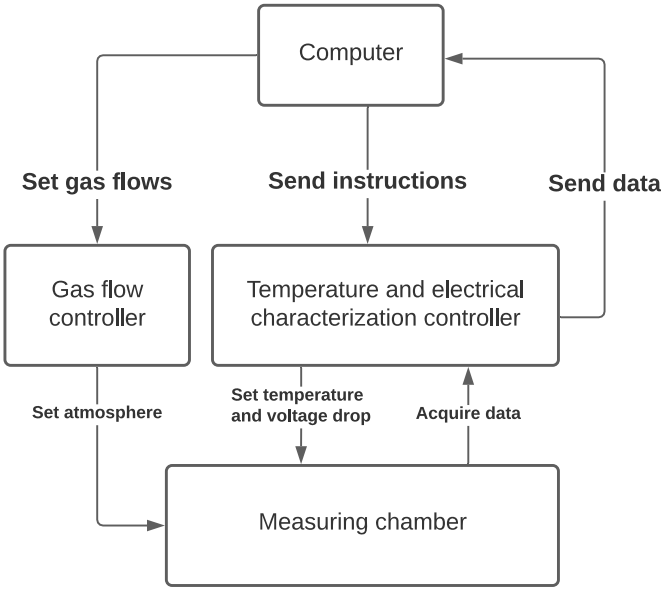


Figure 3.3: The schematization of the main modules of the measurement setup.

The temperature control and the electrical characterization system were developed in custom electronics, and the entire system is interfaced with a custom graphical user interface (GUI) written in Java.

Every module works independently, and the control software carries out the synchronization between the instructions and the data acquisition.

### 3.6.2 Hardware

#### Temperature control

The block diagram in Figure 3.4 summarizes the circuit of the heater driver.

This circuit is designed both to provide power and to measure the temperature of the platinum heater printed on the rear of the sensor's substrate. Usually, heating and temperature measurements are performed using different circuit elements [60]. However, to decrease the total size of the device, it is possible to use a single element. This goal is achieved using the self-heating effect of a thermistor, exploiting the heating caused by the current used to measure the resistance. In standard conditions, self-heating is generally avoided because it affects the temperature to be measured. However, as previously discussed, the majority of chemiresistive gas sensors based on semiconducting materials usually do not operate at RT, then self-heating can be exploited both to supply and to measure the temperature of a sensor.

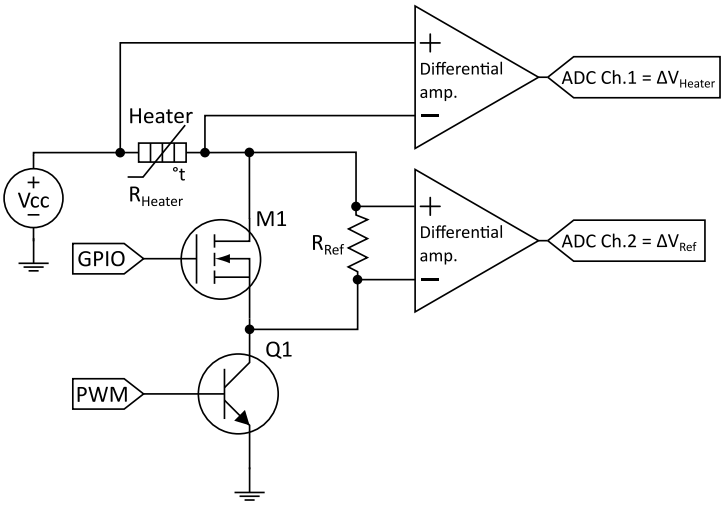


Figure 3.4: Structure of the heater driver. Depending on the state of N-MOSFET M1, the circuit can both provide power to the sensor or measure its resistance.

The electrical scheme in Figure 3.4 is thought to operate in two regimes:

- supply regime that provides energy to the heater,
- measurement regime that acquires the temperature of the heater (measuring the resistance).

In the supply regime, the purpose of the circuit is to provide power to the heater avoiding potential drops on other elements. In this configuration (see Figure 3.4), the MOSFET *M1* is switched ON, and the power control is made using the Pulse Width Modulation (PWM) output connected to the base of the transistor *Q1*. Following the current path in this state, it is easy to notice that the voltage drop is principally on the heater and the transistor *Q1* because the resistance of the MOSFET *M1* is less than 200 $m\Omega$ when $V_{GS}$ equals 3.3 $V$. Since the voltage drop on the transistor is less than 0.3 $V$ if the current is between $20 - 200$ $mA$, in this configuration, the power is for the most part, delivered on the heater.
In measurement conditions, the purpose of the circuit is to evaluate the resistance of the heater. In this configuration, the MOSFET *M1* is switched OFF, and the PWM output is set to its maximum value (the transistor *Q1* is switched ON continuously). Following the current path, in this case, the current circulating through the heater also passes through the calibrated resistance $R_{ref}$ because MOSFET *M1* now behaves as an open circuit. In this way, to obtain the resistance of the heater, it is required to measure the voltage drop on the heater itself and $R_{ref}$. Using Ohm's law, it is possible to calculate $R_{Heater}$ as:

$$R_{Heater} = \frac{\Delta V_{Heater} \times R_{Ref}}{\Delta V_{Ref}} \tag{3.4}$$

where $\Delta V_{Heater}$ and $\Delta V_{Ref}$ are the voltage drop across the heater and the reference resistance $R_{Ref}$, respectively. Both supply and measurement modes involve a variable power provided to the heater since the first one operates in pulsed current, while the second one modifies the load to the main supply. To minimize any oscillation of the temperature, every operation that involves a power modification is carried out in less than one millisecond so that the thermal inertia of the device averages the heat provided to the sensor. In this way, it is just detected the average power and any oscillation of the temperature is almost negligible.
Under operating conditions, the heater driver is set most of the time in supply mode, and it is switched in measurement mode just to measure the temperature of the device. Then, the power provided to the sensor is primarily due to the duty cycle of the PWM input. The main advantage of using the duty cycle of a PWM signal to heat a sensor is that it reduces power dissipation, however, operating in pulsed current always increases the electrical noise of the entire system.
When the power dissipation is not of concern (i.e., laboratory condition), this problem can be avoided by modulating the voltage provided to the heater using a buffered Digital to Analog Converter (DAC). In this configuration, the system works in DC, so *M1* and *Q1* are not actively involved, but they are set *closed* and *open*, respectively. To prevent any interference with the calculation of the interferogram using the Michelson interferometer, the system coupled with the FTIR uses this approach, avoiding fast power transient.
Finally, this circuit is controlled via software using a standard Proportional Integral Differential (PID) algorithm that adjusts the power provided to the heater to obtain the target value set by the user.

### Calibration of the heater

The used substrate has an integrated platinum serpentine screen printed on the rear side of the alumina die. The heater is used both to heat and to measure the temperature of the sensor. The temperature value is derived by measuring the resistance of the serpentine, which can be calibrated as a function of the temperature of the sensor.
To ensure that the heating and the cooling are reversible processes, also at very high temperature, the platinum serpentine is encapsulated in a high temperature resistant ceramic layer. In this way, the calibration of the heater is almost insensitive to the history of the device since any modification in the heater itself is prevented. The calibration is made by using the quadratic form of the Callendar–Van Dusen equation, which correlates the resistance $R$ and the temperature $T$ of a resistance temperature detector (RTD) [61]. This relation states that the resistance can be written as a function of the quantities $\alpha$

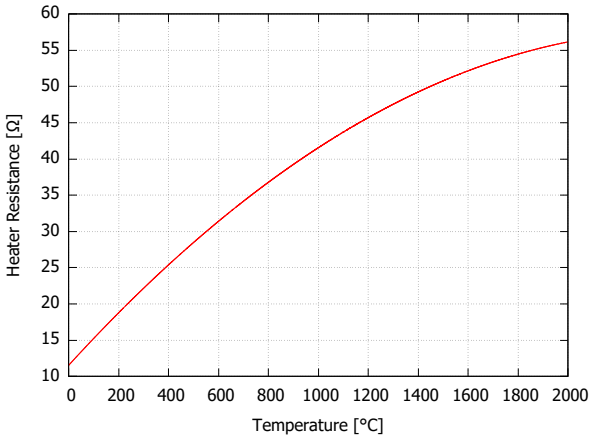


Figure 3.5: Typical calibration of the platinum sensor heater.

and $\beta$ and the resistance at 0 °C:

$$R(T) = R_0 \times (1 + \alpha \times T + \beta \times T^2) \tag{3.5}$$

and referred to a generic temperature $T_0$, equation 3.5 can be rewritten as:

$$R(T) = R(T_0) \times \frac{(1 + \alpha \times T + \beta \times T^2)}{(1 + \alpha \times T_0 + \beta \times T_0^2)} \tag{3.6}$$

For the sensor substrates used, the calibration curve in Figure 3.5 was calculated using the estimated values of $\alpha = 0.0032 \ \frac{\Omega}{°C}$ and $\beta = -6.67 \cdot 10^{-7} \ \frac{\Omega}{°C^2}$.

To measure the device's temperature, the heater driver exploits the average effect of the thermal inertia of the alumina substrate. To estimate the error introduced using this approximation, the resistance variation was measured during the time required by the system to complete a resistance measurement.

To measure the resistance of the heater, it was monitored simultaneously the voltage drop on the heater and $R_{Ref}$ for the time that the driver was set in measuring mode at a temperature of 450 °C.

From $V_{heater}$ and $V_{ref}$, it is possible to extrapolate the resistance of the heater instantly using Ohm's law:

$$R_{heater} = \frac{V_{heater} \times R_{ref}}{V_{ref}} \tag{3.7}$$

Figure 3.6 reports the resistance of the heater during the transient in which the measurement was performed. The entire measurement takes approximately 60 $\mu s$, and ignoring the first spike principally due to the switching of the electronics, during this time, the resistance has a maximum variation of 0.1 Ω that corresponds to a maximum error in the temperature estimation of 3 °C, that can be further reduced by averaging.

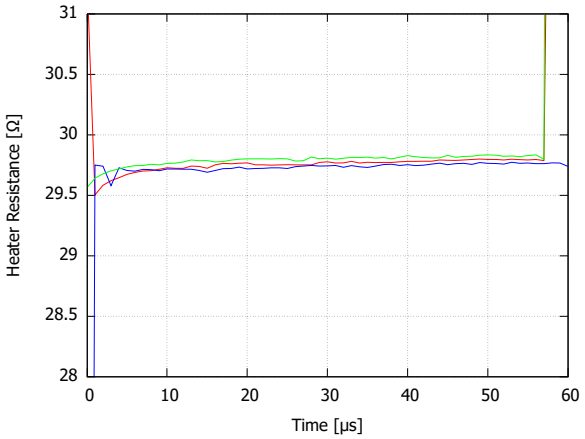


Figure 3.6: Resistance of the heater at 450 °C when the heater driver was set in measurement mode (repeated 3 consecutive times). The resistance was measured sampling with an oscilloscope of the voltage drop at the heater and at R_REF (Figure 3.4).

### Implementation of the electrical characterization hardware

This section describes the hardware developed to perform the electrical characterization on chemiresistive gas sensors. The block diagram in Figure 3.7 summarizes the main components of the measuring circuit in which the sensor is represented as a resistance grounded from one side ($R_{Sens.}$).

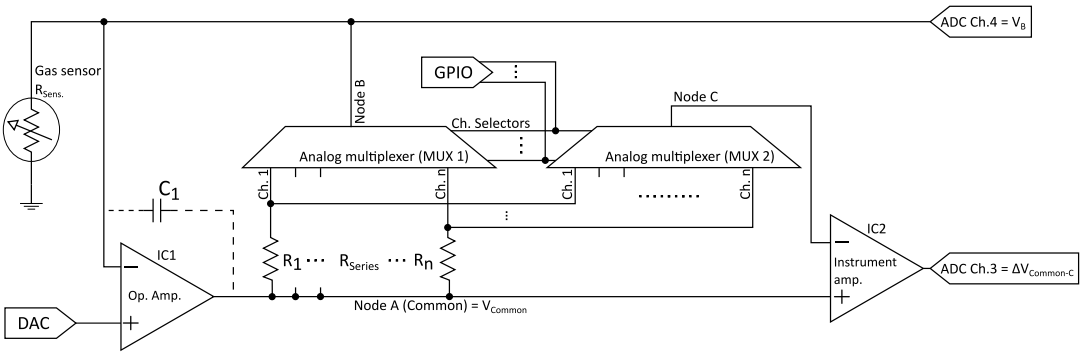


Figure 3.7: Structure of the measurement circuit. The system behaves as a trans-impedance amplifier with programmable gain, where multiplexer MUX1 sets the amplification. MUX2 is used to perform a four wires measurement on $R_i$.

The main goal of the circuit is to set the voltage drop on the sensor and measure the current across it. These measurements are achieved using a circuit similar to a trans-impedance amplifier, where the gain is set using one of the resistance in series with the multiplexer *MUX1*, and the voltage is set using a 12 bits resolution DAC in

the range $\pm 10\ V$. This range was selected to avoid an excessive drop in potential on the sensor electrodes, which can trigger irreversible reactions between the sensing film and the gas to be detected. The trans-impedance configuration is arranged, connecting one end of the sensor and the DAC output to the inverting and the non-inverting inputs of the operational amplifier *IC1*, respectively. With this arrangement, *IC1* tries to increase its output voltage until the voltage difference between the inverting and the non-inverting inputs equals zero (virtual ground). Considering no current passing through the multiplexer *MUX2*, $\Delta V_{Common-B}$ can be written as a function of the internal resistance of the multiplexer *MUX1* and the resistance connected in series with the sensor:

$$\Delta V_{Common-B} = V_{Common} - V_B = R_{channel} \times I + R_{series} \times I \tag{3.8}$$

where $R_{channel}$ is the internal resistance of the multiplexer, $R_{series}$ is the resistance in series with the selected channel, and $I$ is the current through *MUX1*. If $R_{series}$ are chosen in a way that $\frac{R_{channel}}{R_{series}}$ is always small, the voltage drop due to $R_{channel}$ is almost negligible. However, for less resistive sensors, this ratio becomes important, compromising the accuracy of the measurement. Moreover, $R_{channel}$ depends on many unpredictable factors, as the aging of the component or the different conditions of use, so it cannot be exactly deleted with a software correction.

To reject this issue and achieve accurate measurements, it is mandatory to discard the voltage drop due to the internal resistance of the multiplexer *MUX1*. This correction is obtained using the multiplexer *MUX2*, connected in parallel with the multiplexer *MUX1*. These share every pin, except the output pin (node $C$) connected to an input of the instrumentation amplifier $IC2$. Since selection pins are shared, *MUX1* and *MUX2* always select the same channels, so node $C$ is always connected to the resistance $R_{series}$ selected by the multiplexer *MUX1*. Since node $C$ is connected to one of the inputs of an instrumentation amplifier ($IC2$), there is no significant current flowing through *MUX2*, so there is no voltage drop due to its internal resistance, and $\Delta V_{Common/C}$ is just the voltage on the selected resistance in series with the sensor. Therefore, it is possible to write the current through the sensor as:

$$I = \frac{\Delta V_{Common-C}}{R_{series}} = \frac{V_{Common} - V_C}{R_{series}} \tag{3.9}$$

where $R_{series}$ is the resistance selected by *MUX1*. Operationally, this configuration is equivalent to a four-wire measurement, where the right node is automatically selected by the multiplexer *MUX2*. Every resistance connected to the multiplexer *MUX1* determines a specific dynamic range of the instrumentation. The selection of the more appropriate combination is obtained via software, limiting the maximum voltage drop on $R_{series}$ (see Figure 3.9). By now, the circuit in the Figure 3.7 was treated as ideal, even if there are situations in which some corrections are necessary.
One frequent issue, especially working with very low currents, is stability. The last

depends on the chosen hardware, however if necessary, adding a small ceramic capacitor (*C1*) between node *Common* and node *B* contributes to solving this issue. A suitable value for *C1* is between 50 $pF$ and 10 $nF$. Particularly important is also the choice of $R_{series}$ connected to *MUX1*. Indeed, very high resistance can cause systematic errors due to the leakage currents of the multiplexers, while very low resistance has to take into account the limited current that *IC* components can supply and the not negligible resistance of the Printed Circuit Board (PCB) traces. Generally, optimal values for $R_n$ are $R_i = 10^i$, where $i$ goes from 1 to 8. In this way, the largest resistance is $R_8 = 100$ $M\Omega$ while the lowest is $R_1 = 10\ \Omega$. From this consideration, it is possible to calculate the minimum and maximum current measurable with that system. The lower limit is obtained connecting the highest resistance that is 100 $M\Omega$, while the upper limit is obtained connecting the lower resistance that is 10 $\Omega$. Using an effective 13 bits resolution ADC with a range of $\pm 1.67\ V$, an overall dynamic range of 4 $pA$ to 170 $mA$ is obtained, so ultimately, the reliable dynamic range is restricted by the specifications of the mounted components.

### 3.6.3 Software implementation

The software implementation of the measuring system is divided into two parts:

- Firmware, for direct control of electronics and low-level functions.
- Graphical User Interface (GUI), to interact with the user, which allows both the acquisition and display of data and the control of high-level functions.

#### Firmware

The firmware was written in *C++* and loaded on a *Teensy 3.6* development board. The board is programmable in the Arduino development environment and is equipped with an *MK66FX1M0* chip manufactured by *Freescale*. The *Teensy 3.6* board was chosen since it integrates the necessary analog modules, including two 16-bit ADC (Analog to Digital Converter), two 12-bit DAC (Digital to Analog Converter) many buses to expand the system with additional modules and enough memory to load programs with many functionalities.
Conceptually, the firmware is designed to work as a data logger but can also interact with the instrument to modify the working parameters (e.g., working temperature) and the measurement conditions (e.g., voltage drop applied to the sensitive film). The firmware, therefore, acts as an intermediary between the user interface (computer) and the analog hardware, which carries out the measurements on the gas sensor. The firmware structure is divided into three main parts:

- A communication protocol to communicate with the computer.

- The functions to acquire the single data that sets the hardware correctly according to the measurement to be acquired.
- A mechanism that emulates a timed multithreading environment to simplify the expandability of the code.

The operation of the firmware is schematized in Figure 3.8.

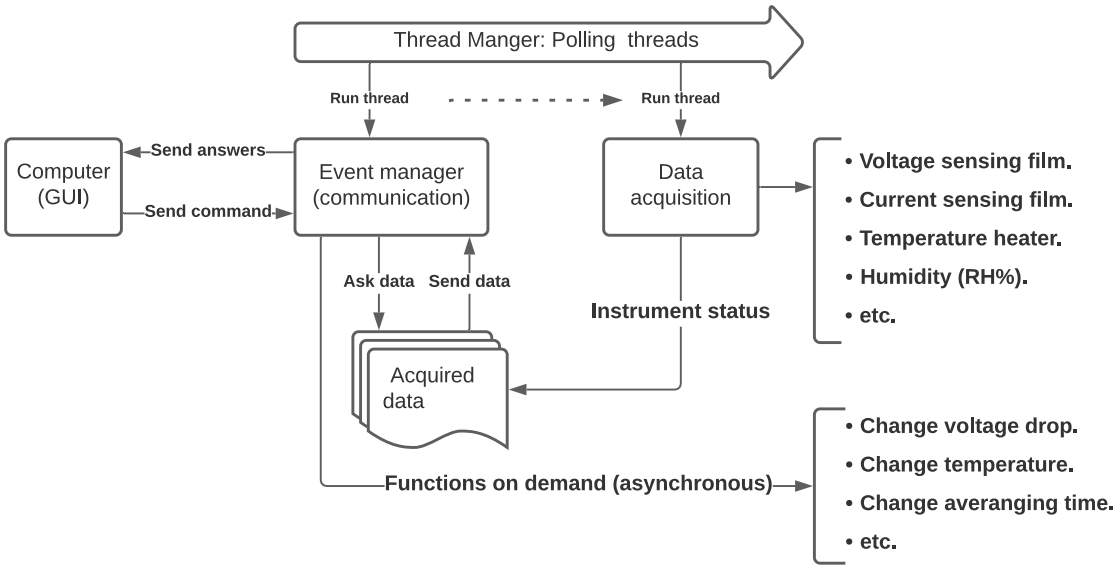


Figure 3.8: Operation of the firmware loaded on the instrument. The program flow is controlled by an emulator of a multithreading environment that sequentially launches the execution of the threads that compose the firmware. The main threads are those dedicated to communicating with the computer and those dedicated to acquiring the various possible measurements.

The data transfer to the computer takes place through a virtual serial port, simulated on a USB port. The communication protocol consists of the reciprocal exchange between the computer and the microcontroller of strings of character separated by a divider (by default, the *newline* character '$\backslash n$' is used). The protocol emulated a master and slave approach, where the computer is the master, and the microcontroller is the slave. Each string corresponds to a command that identifies a precise function to be executed, with one or more arguments and a more or less complex answer, depending on the situation. Therefore, the microcontroller is always in the background listening for the commands to be executed, which can be the request for a specific measurement or the modification of an acquisition parameter (e.g., the current supplied to the heater, the averaging time,

etc.). To clarify this step, one can consider, for example, how two different commands are interpreted: the reading of the potential on the sensing film of a gas sensor and the setting of the current value through the platinum heater. In the first case, as happens for the acquisition of all the numerical values, the computer sends a string that identifies the value to transfer, which in the case of the potential on the sensing film is *"ReadVoltageSensor \n"*. At this point, the string is received and decoded, and the requested value is sent to the computer, which is waiting to receive a reply. In the second case, the computer sends a command with an argument that is not answered. In the case of the platinum heater current, the strings *"Setcurrentheater \n"* $+ VALUE\backslash n$ are sent, which are interpreted by the microcontroller by setting the current through the heater to the value $VALUE$.
Once a correct communication protocol has been established between the computer and the microcontroller, it is essential to correctly use the modules that allow the acquisition of the different measurements. The most significant example is the module that manages the mpere meter auto range, described in paragraph 3.6.2. This module allows to automatically choose the optimal measurement range to measure the current through the sensing film. When a current measurement is required, the system decides whether to amplify or de-amplify the measurement based on the value read, increasing or decreasing the load resistance $R_n$ in the trans-impedance operational (Figure 3.7). Although this procedure may seem intuitive, it is important to consider some sort of hysteresis in the amplification change to prevent any oscillations between different amplification stages for measurements over adjacent measurement ranges (Figure 3.9).

Finally, the last conceptual component that composes the firmware is a timed multithreading system. In a microcontroller, multithreading is not native to hardware. However, its software implementation is very convenient from the firmware architecture's point of view since it simplifies the drafting and reduces development times. Each thread is simulated by a *setup()* code and a *loop()* code, executed repeatedly at regular intervals. The set of all threads is managed by the mainstream of the program, which calls their execution according to their execution intervals (*polling*). In this way, all the parameters are controlled using separate threads to emulate a parallel execution, although a precise execution order is respected. Each part of the firmware exploits this approach. For example, the reading and the decoding of the strings described by the communication protocol is managed by a thread whose task is to check for incoming events. In the same way, the measurements are acquired using another independent thread, and the instrument is always in the correct measurement range regardless of the instructions received from the computer. Another advantage of this approach is the ability to easily expand the firmware by adding other hardware components, which can be controlled by a dedicated thread that runs cyclically together with the other parts of the firmware.

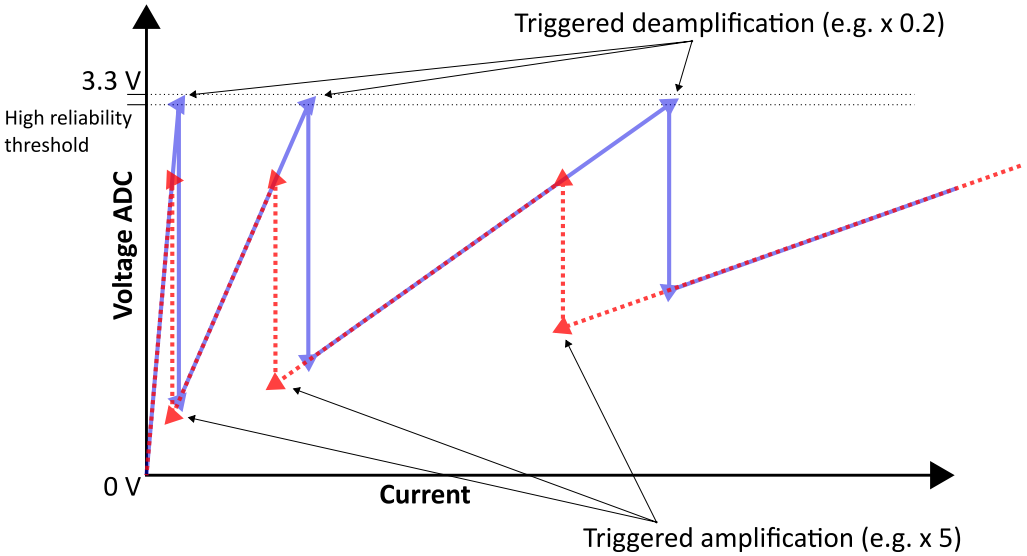


Figure 3.9: Operation of the auto-range of the transconductance amplifier described in Figure 3.7. It is observed that the relationship between the potential read at the textit ADC Ch. 3 channel, and the current through the sensitive film depends on the direction of the current. Indeed, the amplification and the de-amplification is made in such a way that hysteresis is formed between increasing and decreasing current, to avoid that the auto range enters into resonance and ensure that the current is always read using the optimal amplification.

### User interface

The instrument is controlled by a dedicated program written in Java that allows the user to control all the parts composing the instrument and visualize, export, and pre-process the acquired data.
Since the device is designed to be used not only standalone but also together with other instruments, controlled with the corresponding programs (e.g., *OPUS* by *Bruker* for controlling the FTIR in the *operando* system), the graphical interface (GUI) has been designed to be expandable, to modify the number of open windows and the graphics of the program according to the type of experiment.
When the program is launched, communication with the instrument is established, and afterward, the software starts polling the data from the instrument in the background. Indeed, every raw data are always acquired, and the user decides just which data view or exported. The main window consists of a bar menu and a graphic window in which the measurement is monitored and visualized. From the implementation point of view, however, it is not the data to be assigned to a graph, but is a dataset that is associated with graphical windows. In this way, the simultaneous monitoring of different quantities

(e.g., the current through the sensing film, the temperature, etc.,) can be done simply by creating multiple windows that point to the same dataset (Figure 3.10). Therefore, the program follows a multi-window approach, acquiring all the data in the background but leaving the user the possibility to expand or not the complexity of the graphics that display them.

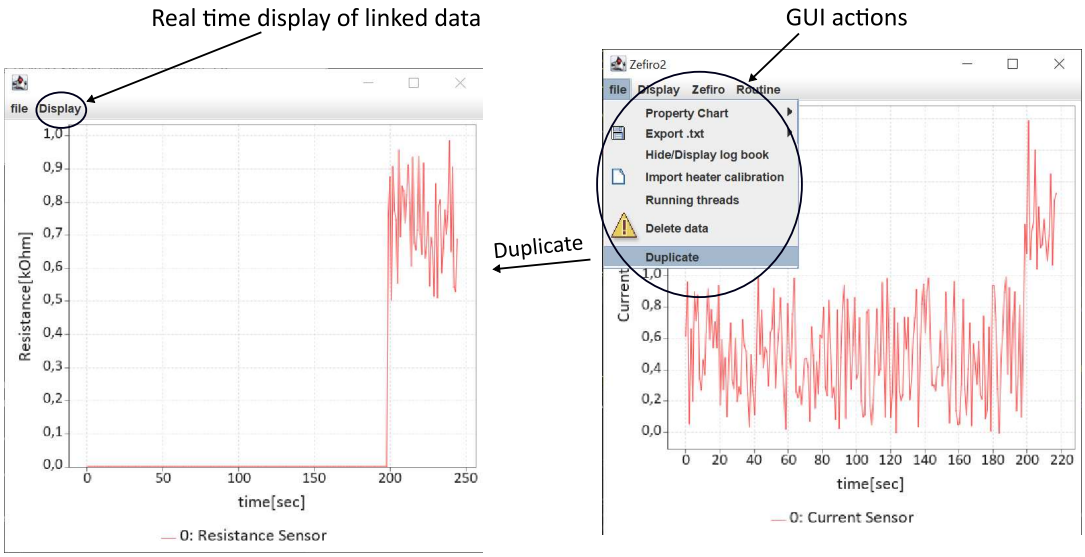


Figure 3.10: The main window of GUI. By default, the single graph can only be represented by data with the same units of measurement at the same time. However, multiple graphical windows can be associated to the same dataset (duplicating the windows) to monitor together and in real-time all the acquired data. (Plotted data are simulated to test the GUI)

In addition to monitoring the raw data, each data can be associated in real-time with a series of conditional analyzes or procedures, which may include real-time denoising of the acquired data or the calculation of the resistance of the sensitive film by combining the measurement of current and potential.
However, the user interface is not only a data logger but also works as a controller to set the instrument outputs or synchronize the measurements. In this way, it is possible to automate the acquisition of high-level measurements such as the I-V and I-T characteristics.
All high-level procedures are organized in the form of procedures (*routine*) that are launched setting some parameters. As an example, one can see how the measurement of the I-V characteristic is made. The user is asked to indicate a series of parameters, which configure the acquisition of the characteristic: the measurement range, the step and the advance delay, how many times to repeat the measurement, and the shape of the potential sweep (triangular or sawtooth). Once the measurement parameters have

been set, the *routine* starts displaying the data in real-time in an independent graphic window. This window collects all the data acquired by the procedure, which are the acquired curves in the case of the I-V characteristic. In addition to the raw acquisition of the curves, also in this case it is possible to associate an analysis to each characteristic, such as a linear or polynomial fitting of which it is possible to monitor the parameters extracted over time (Figure 3.11).

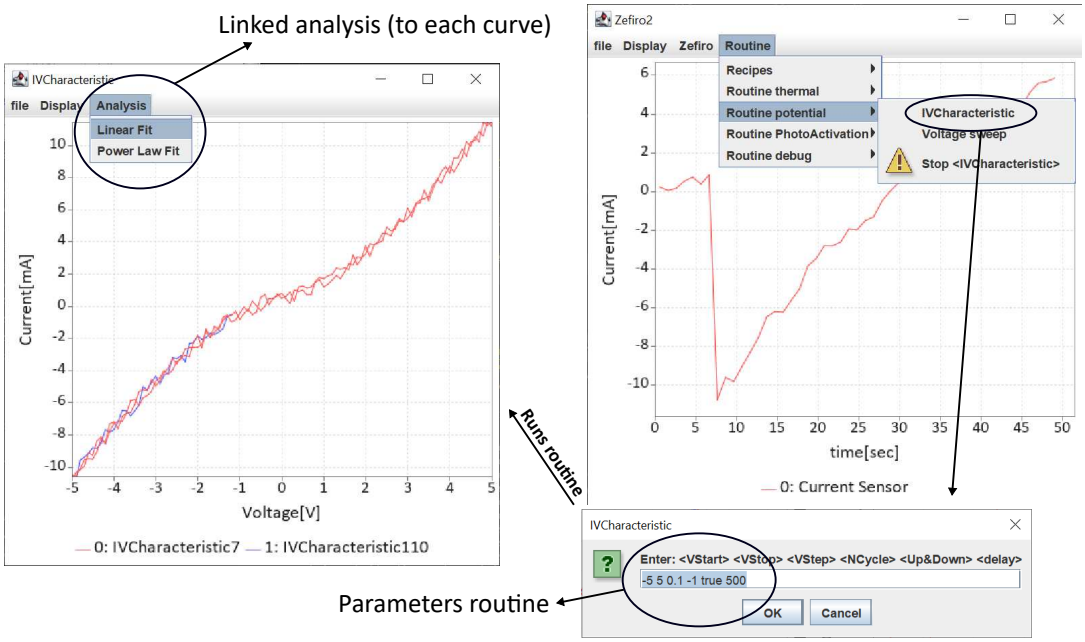


Figure 3.11: Steps for launching the routine for the automatic acquisition of the I-V characteristic. Once the acquisition parameters have been defined, the procedure is launched in parallel with the other procedures. The acquired data are displayed in real-time in a dedicated window from which it is possible in turn to trigger a series of automatic analyzes (e.g., a linear fit) (Plotted data are simulated to test the GUI).

*Routines* are collected in groups independent of each other, and routines belonging to different groups can be overlapped. Furthermore, control is always on the user that can stop any time running routine without data loss. Independent threads control each routine; consequently, the normal program flow is not interrupted when a *routine* is executed. For this reason, the logging of raw data in the background continues, monitoring any changes made by the execution of the *routines*. With this approach, it is always possible to reconstruct the steps taken, identifying any unexpected crosstalking from the direct monitor of the raw data.
With the high-level procedures, all commands can also be sent to the firmware manually, using the appropriate menu in the main window (Figure 3.12). In addition to the normally active threads described above, other processes are also performed in the back-end,

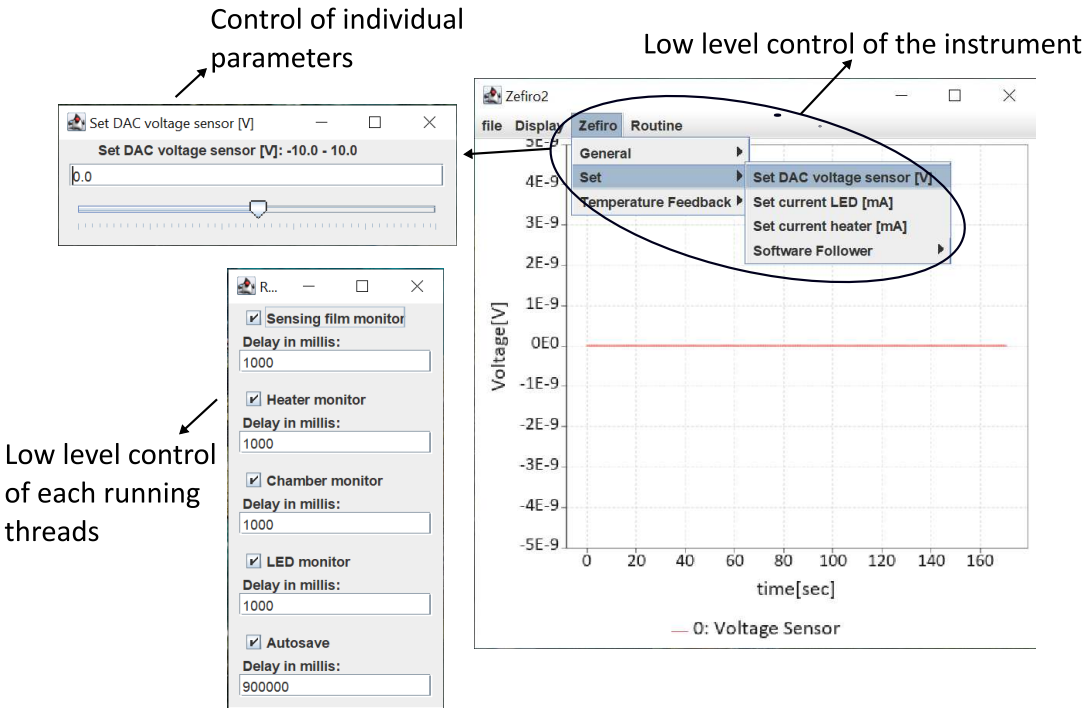


Figure 3.12: The figure shows how the acquisition variables are accessed manually and how to enable/disable the execution of the single threads of the GUI.

which simplifies the use of the instrument, for example, the PID (proportional, integral, derivative) control of the sensor temperature, the self-saving of the acquired data, the self-filling of the history book, and watchdogs that prevent incorrect use of the instrument (e.g., overheating of the measuring chamber or an accidental short circuit).
The program also has a procedure dedicated to the calibration of the resistance of the heater of a sensor to the temperature and the possibility to load *"recipes"* in the form of a text file to synchronize the execution of commands with procedures performed by third-party programs (e.g., programmable temperature sequences) (Figure 3.13).

In conclusion, since the control software and the user interface are functional to the use of an instrument, we tried to create a tool that was both simple to use and easily expandable to be able to customize the acquisition mechanism depending on the experiment to be set up.

### 3.6.4 Implemented measurements

Two types of measurements are managed by the system: low-level and high-level measurements.
Low level refers to the measures that monitor just a single physical quantity associated

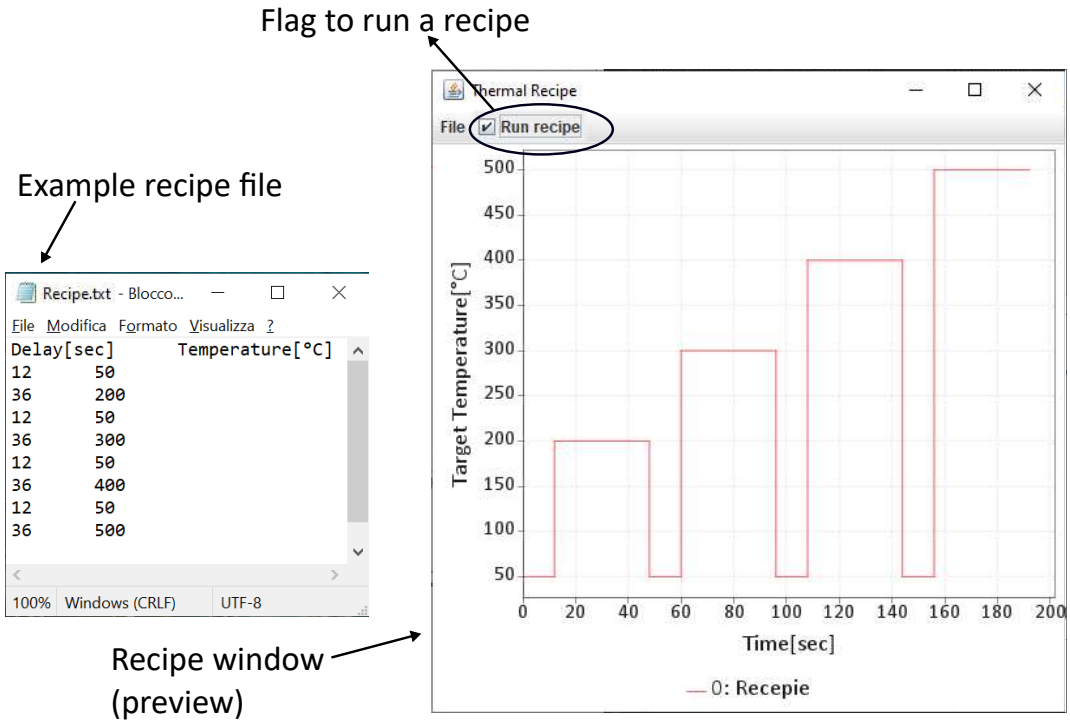


Figure 3.13: The window for launching the *recipes*. A recipe is a text file that encodes a series of low-level commands. In the graph on the right, we see, for example, a recipe for timed heating of a sensor. This type of control is advantageous if you want to synchronize the instrument with third-party instrument programs (e.g., the FTIR control program in the *operando* system). (Plotted data are simulated to test the GUI).

with a sensor. The system is designed to monitor:

1. Voltage and current through a sensor.
2. Resistance of a sensor, calculated as the ratio of the applied voltage vs. the current.
3. Resistance, temperature, and power provided to the heater.
4. Temperature and relative humidity of the measuring chamber during operation.

These measurements are useful to evaluate fast phenomena, for example, the response of the gas sensor to an abrupt modification of the working condition, such as the atmosphere composition or the temperature. Low-level measurements are also helpful as a control variable to detect malfunction during more complex measurements.

High-level measurements consist of more complex operations that synchronize instructions (i.e., voltage and temperature settings) with the data acquisition. These

types of measurements are the *routines* described above, started by the user by fixing some parameters.

Currently, the main implemented *routines* are of two types:

1. Current-Voltage characterization.

2. Current-Temperature characterization (or Arrhenius plot).

### Current-voltage characteristic

The current-voltage characterization is the study of the current through a sensor as a function of the applied potential. For chemiresistive gas sensors, it is expected a linear characteristic since they behave ideally as resistors. However, depending on the sensing material and the measurement conditions, different behaviors are observed. A well-known example concerns metal-oxide gas sensors, which show a behavior analogous to that of varistors [62, 63]. In particular, it is verified that the I-V characteristic is well described, from a phenomenological point of view, by a power law:

$$I = k \times V^{\alpha} \tag{3.10}$$

where $I$ is current, $V$ is the applied potential, and $k$ and $\alpha$ are constants to the applied potential. Equation 3.10 reduces to the *Ohm*'s law for $\alpha = 1$, then $\alpha$ is the linearity factor of a sensor.
By measuring the I-V characteristic, it is also possible to understand anomalous behavior in chemiresistive gas sensors, as the loss in symmetry depends on applied polarity or the damaging of the devices after long periods of operation. These latter considerations highlight the importance of the I-V characteristic, both as a testing tool and for modeling the conduction mechanism of a new type of material [64, 62, 26]. For this reason, to evaluate the evolution of the I-V characteristic systematically at different thermodynamic conditions, the acquisition procedure of the I-V characteristic has been automated so that it can be programmed with the use of some significant values (i.e., starting voltage, finishing voltage, incremental step, number of cycle and delay between sampling).

### Current-temperature characteristic

Like the I-V characteristic, the current-temperature characterization is the study of the current through a sensor at a fixed applied potential as a function of the temperature. In semiconductor materials, the I-T characteristic is usually well described by an exponential behavior [65]:

$$I \propto \exp\left\{\frac{-E_a}{k_B T}\right\} \tag{3.11}$$

Where $I$ is the current through the sensor, $T$ is the absolute temperature, $E_a$ is the activation energy, and $K_B$ is the Boltzmann constant. The equation 3.11 is linearized, plotting the logarithm of the current as a function of the inverse of the absolute temperature. These coordinates are referred to the Arrhenius plot, and this representation is useful to highlight deviations of the I-T characteristic from the eq. 3.11. Since chemiresistive gas sensors are usually based on semiconductor materials, the eq. 3.11 generally fits the I-T characteristic of a sensor, however, some deviation from eq. 3.11 could be observed if other thermally activated mechanisms are involved. A typical example in chemiresistive gas sensors is the adsorption/desorption of gaseous species on the sensor surface, which is dependent on the temperature. In this case, the eq. 3.11 is verified in the range of temperatures for which every surface reaction is negligible. From a qualitative point of view, the adsorption/desorption modifies the I-T characteristic by displaying the mismatch of the same obtained by increasing or decreasing the temperature. Indeed, adsorption and desorption usually have different kinetics, so a mismatch is observed at a fixed rate of temperature increase.
The above-mentioned considerations highlight that the I-T characteristic has an important role in understanding the thermoelectric behavior of a chemiresistive gas sensor. Therefore, measuring its evolution in different conditions is fundamental. For this reason, the acquisition of the I-T characteristic has been automated as for the I-V characteristic, and it is performed just by setting some parameters (i.e., starting temperature, finishing temperature, incremental step, number of cycles, the delay between sampling).

### 3.6.5 Validation of the electronics

As a case of interest for validating the presented instrumentation, an $SnO_2$-based gas sensor was electrically characterized. The sensor's response was acquired at different conditions, i.e., applying different polarization voltage, working temperature, and working atmosphere. In particular, the sensor performance was studied when it was exposed to increasing $CO$ concentrations in dry conditions, with a voltage ranging from $-10$ to $10\ V$, at a temperature ranging from $RT$ to 600 °C. These ranges were chosen both, considering the instrument's characteristics and the limits of the material under test. $SnO_2$ is a well-established material for gas detection, so the goal of these analyses was to replicate the behaviors observed in literature for this sensing material to validate the entire system [66, 66]. To maximize the reliability between different characterizations, all measurements were carried out using the same sensor. The analyses performed were the following:

1. Monitoring of the sensor signal when exposed to increasing $CO$ concentrations.
2. The I-V characteristic at different temperatures and $CO$ concentrations.
3. The Arrhenius plot at different polarization voltages and $CO$ concentrations.

Current through the sensing film in place of the standard sensor response is reported to highlight the data acquired from the instrumentation.

### Direct monitoring of the sensor signal

The current through the sensing layer of the sensor in different conditions was acquired, gradually increasing the $CO$ concentration from 0 to 100 $ppm$ with steps of 25 $ppm$. Due to the desorption of chemical species on the $SnO_2$ sensor surface, the signal usually drifts for almost two hours after every modification of working temperature [67]. To avoid this situation, before acquiring any data, a stable signal baseline was achieved. Figure 3.14 shows the current passing through the sensor at 300 °C at different applied voltages.

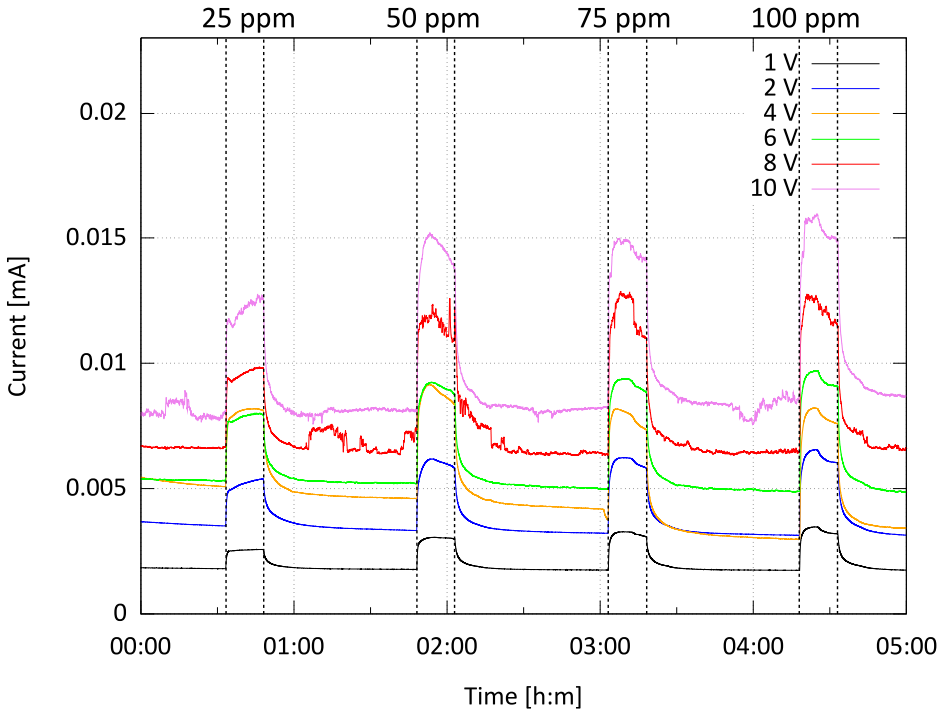


Figure 3.14: Current through the $SnO_2$ sensor at 300 °C exposed to increasing $CO$ concentrations at different applied voltages.

As expected, the current increases with the applied voltage, but it is significant to highlight that the noise also increases with the voltage. In particular, for voltages higher than 6 $V$, the current is unstable highlighting a possible modification in the sensing film induced by the measuring potential. Moreover, one can observe that the current increases with the gas concentration, which corresponds to a decrease in the sensing film's resistance, as expected for the $SnO_2$ sensor exposed to $CO$ atmosphere. Figure

3.15 shows the current passing through the sensing film at 1 $V$ at different working temperatures.

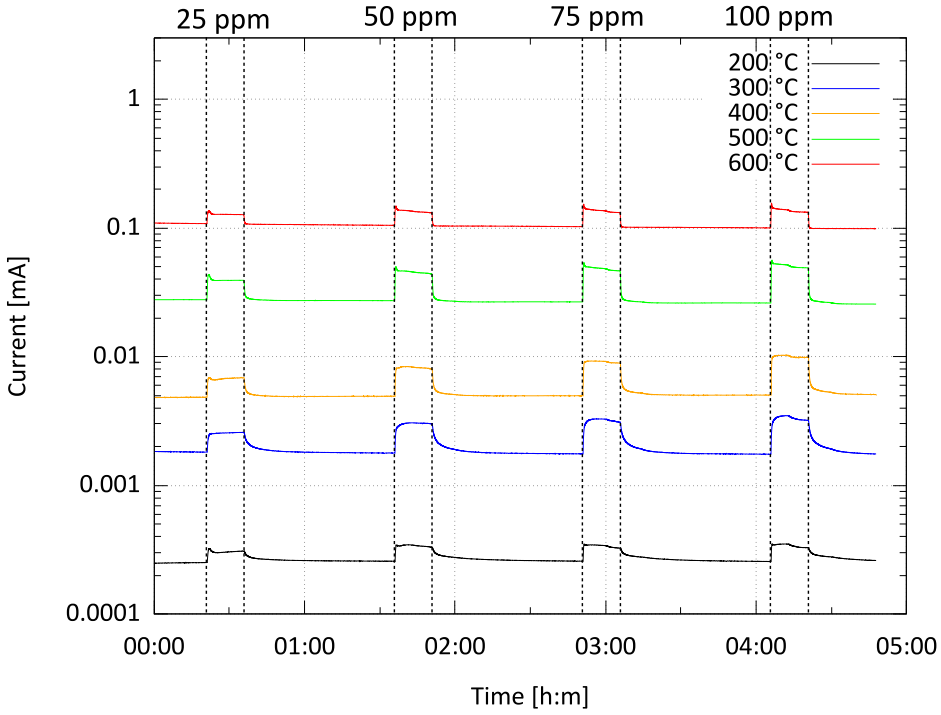


Figure 3.15: Current through the $SnO_2$ sensor at 1 V exposed increasing $CO$ concentrations at different working temperatures. The current is displayed as a logarithmic scale.

As expected, the current increases with the temperature, but it can also be observed that the response pattern and recovery time change.

### Current-voltage characterization

The current-voltage characteristic of the $SnO_2$ sensor was evaluated at different working temperatures and $CO$ concentrations. The characteristic was acquired from $-10$ to 10 $V$, increasing and decreasing the voltage with steps of 0.1 $V$ and applying a measurements delay of 1 second. In Figure 3.16 the current-voltage characteristic in dry air (0 *ppm* $CO$) at different working temperatures is reported.

As expected, at each applied potential, the current increases with the temperature, but temperature also changes the shape of the curves. In particular, for low temperatures (Figure 3.16, top), the characteristic is not linear but fits with the power-law described by eq. 3.10. Therefore, one can observe that $SnO_2$ gas sensors at low working temperatures behave as varistors, with which they have many constructive analogies, whereas, at

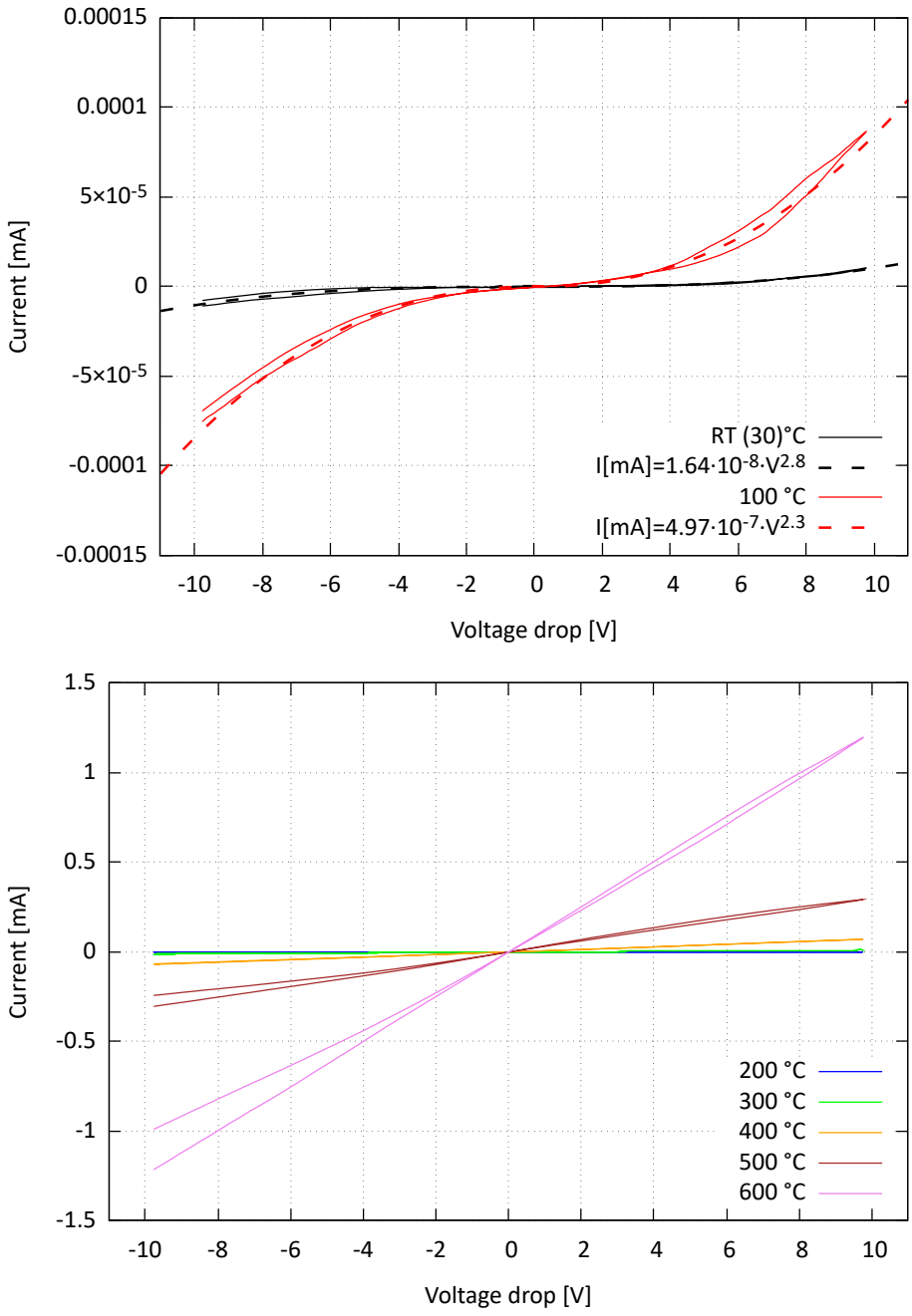


Figure 3.16: Current-voltage characteristic in dry air of the $SnO_2$ sensor at different working temperatures. At low temperatures (top), the sensor behaves like a varistor, and at high temperatures (bottom), the sensor behaves like a resistor. Dashed curves on the top are the fit of low-temperature characteristics using eq. 3.10.

higher working temperatures (Figure 3.16, bottom), they behave like resistors [68, 62, 63]. From an operational point of view, it is crucial to know the voltage for which the I-V characteristic of a sensor deviates from linearity since, to operate in reliable mode, the response of a chemiresistive sensor has to be independent of the applied potential.
Figure 3.17 shows the current-voltage characteristic of $SnO_2$ sensor at 300 °C exposed to different $CO$ concentrations.

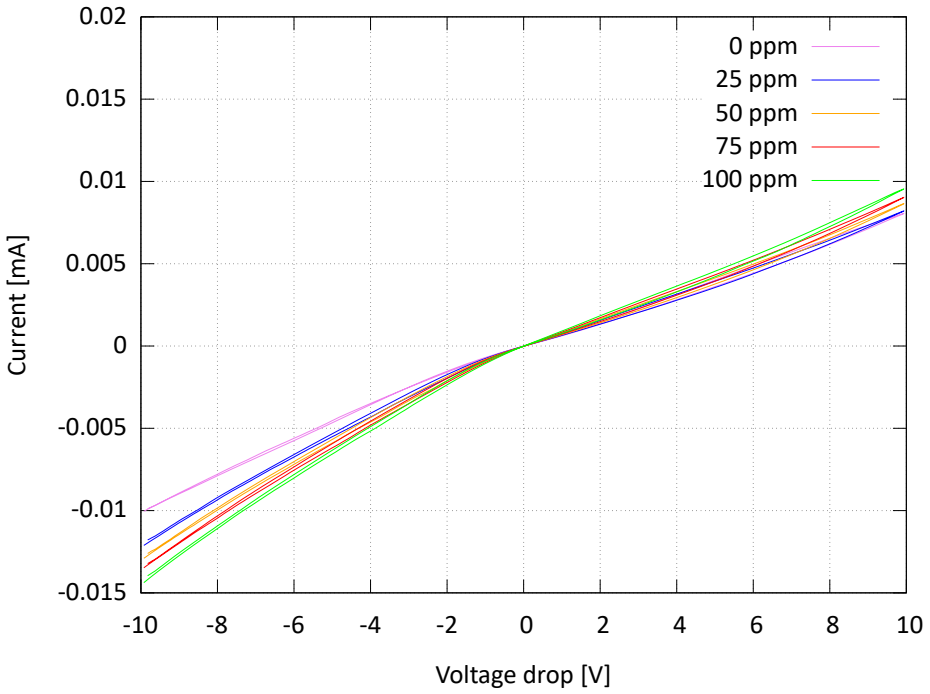


Figure 3.17: Current-voltage characteristic of the $SnO_2$ sensor at 300 °C at different $CO$ concentrations.

As previously observed in Figure 3.14, the current increases with the $CO$ concentration, but in this case the shape of the I-V characteristic is almost insensitive to the gas exposure.

### Current-temperature characterization

The current-temperature characterization of the $SnO_2$ sensor was evaluated at different applied potentials and different $CO$ concentrations. The temperature was varied from 100 to 600°C, both increasing and decreasing the values, with a rate of 1°C every 10 second. Figure 3.18 shows the Arrhenius plots acquired in dry air (0 *ppm* $CO$) at different applied voltages.

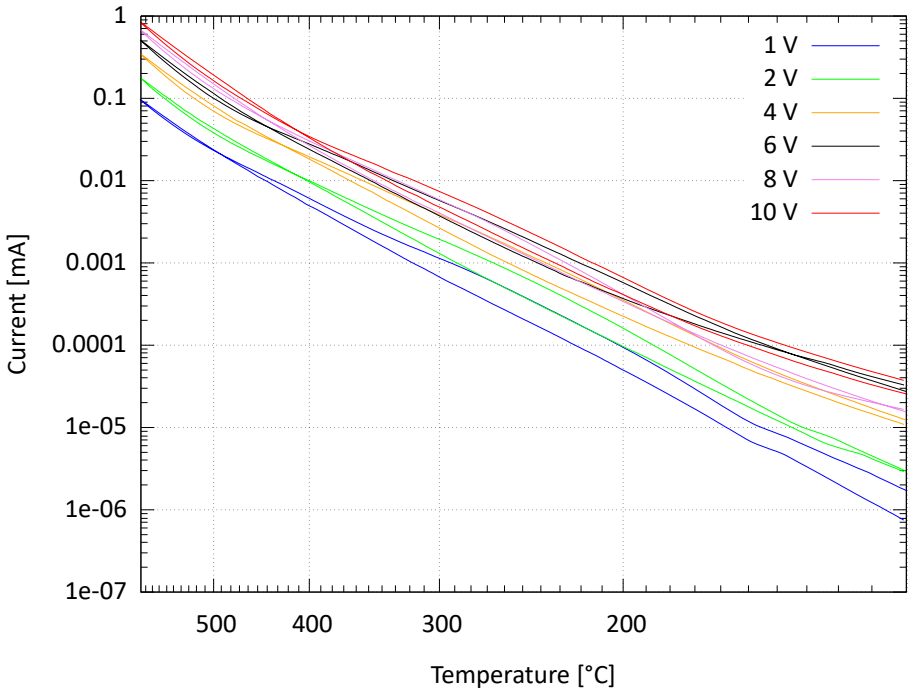


Figure 3.18: Current-temperature characteristic of the $SnO_2$ sensor in dry air at different applied voltages. The curves are displayed as Arrhenius plot scaling the y-axis as logarithmic and the x-axis as the inverse of the absolute temperature.

The current *vs.* temperature follows approximately an exponential behavior for each applied potential, as described by the equation 3.11. Each curve in Figure 3.18 is almost parallel to each other, then in the examined range the activation energy $E_a$ is almost insensitive to the applied voltage with values ranging from 0.6 to 0.8 $eV$, as reported in previous studies [69].
Figure 3.19 shows the current-temperature characteristic at 1 $V$, at different $CO$ concentrations of $SnO_2$ sensor.

As previously highlighted in Figure 3.18, each curve appears as a parallel straight line, so the activation energy $E_a$ is almost constant also respect to the $CO$ concentration. An increase in current can be observed with the gas concentration, as arisen in the previous analysis.
Both in Figure 3.18 and in Figure 3.19, it is shown that the heating and cooling process is not completely reversible. In particular, for temperatures under 400 °C, one can observe a hysteresis that overlaps every curve. This is particularly important for identifying the best operating temperature of the sensor since low hysteresis is mandatory to obtain reproducible measurements.

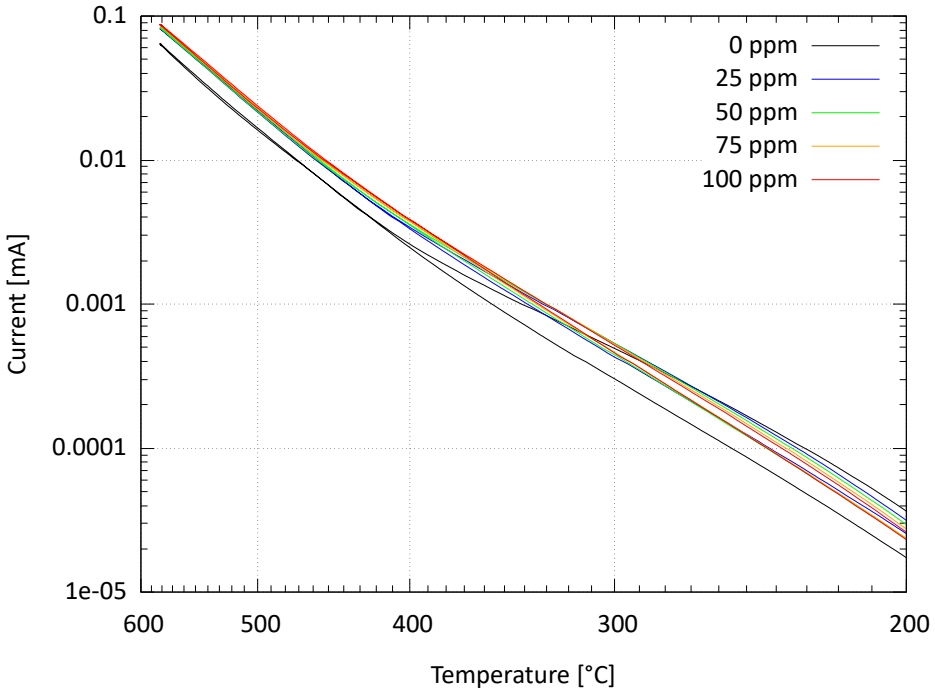


Figure 3.19: Current-temperature characteristic of the $SnO_2$ sensor at 1 V at different $CO$ concentrations.

### 3.6.6 Comparison with standard instrumentation

To evaluate the measuring circuit described in section 3.7, the system has been compared with a standard setup used to characterize semiconductors devices to evaluate the measuring circuit described in the section. This setup consists of four *Keithley 238* connected to a prober through a switching matrix *Keithley 707*, equipped with *7072* and *7174* semiconductor cards. To validate the circuit, the I-V characteristics of eight resistors with values ranging from $10^2$ Ω to $10^8$ Ω have been recorded using the equipment cited above as reference. A linear fit has extrapolated the resistance value on the current-voltage characteristic to estimate the agreement between the measurements.

In Figure 3.20, the I-V characteristics acquired with both setups are reported: solid red lines are acquired using the presented equipment, and dashed blue lines are acquired using the certified instrumentation.

The measurements show good agreement across the entire dynamic range, and fitted values are comparable under one part in a hundred. A little deviation from linearity is measured for the highest resistance with negative applied voltages.
To evaluate the performance of the measuring setup also in a real use case, the current through an $SnO_2$ sensor at 1 $V$, heated to 300 °C, has been simultaneously recorded using

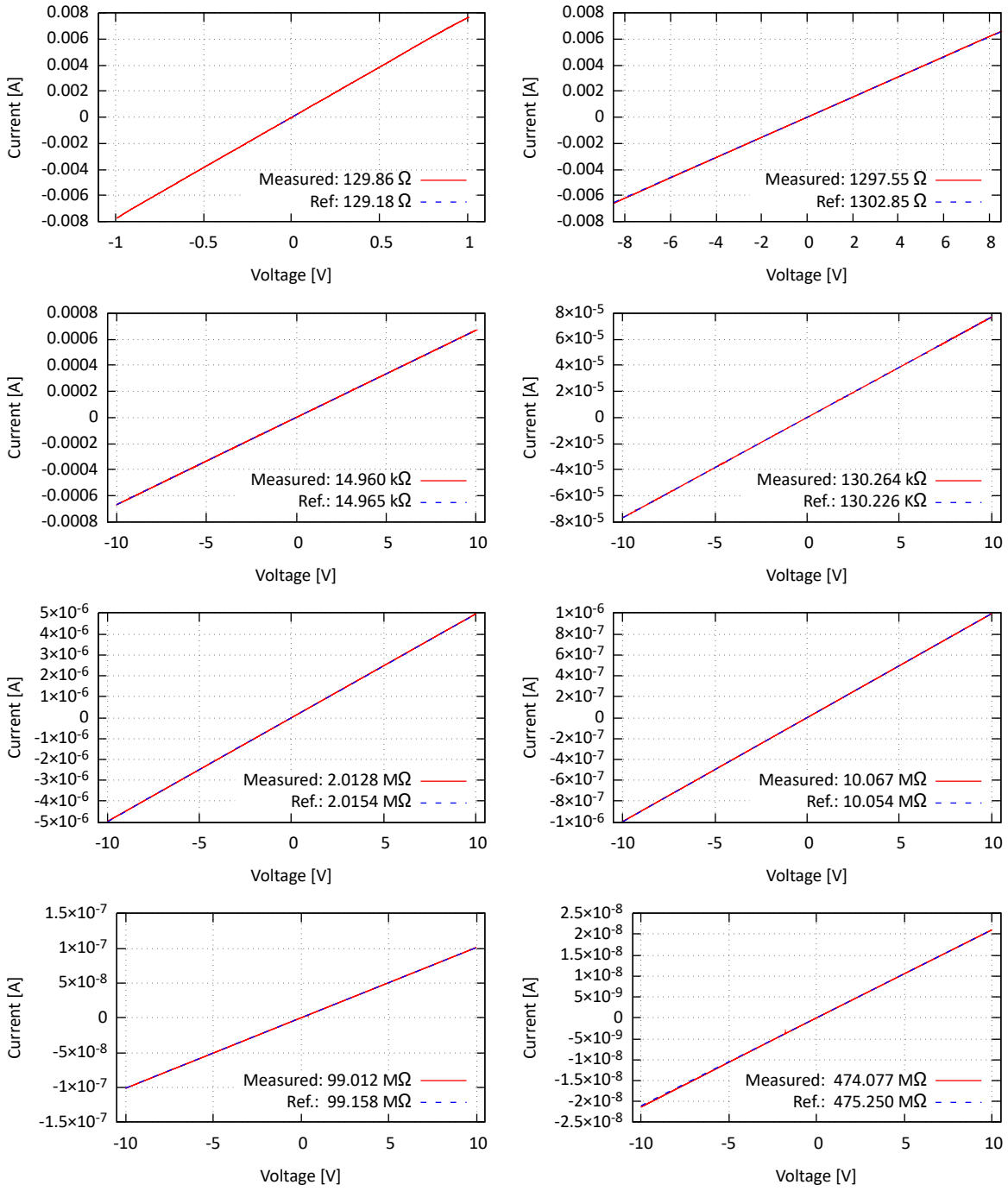


Figure 3.20: I-V characteristics of eight resistors: solid red lines are measured with the presented setup, and dashed blue lines are measured with the above reference system. Every curve goes from $-10$ to 10 $V$, except for $A$ and $B$, to limit the maximum voltage through the multiplexer *MUX1* in Figure (3.7).

| Name | Resistance Measured Ω | Resistance Reference Ω | Percent Error % |
|---|---|---|---|
| R1 | 129.86 | 129.18 | 0.53 |
| R2 | 1294.91 | 1302.82 | 0.41 |
| R3 | $14.960 \cdot 10^3$ | $14.965 \cdot 10^3$ | 0.04 |
| R4 | $130.264 \cdot 10^3$ | $130.226 \cdot 10^3$ | 0.03 |
| R5 | $2.0128 \cdot 10^6$ | $2.0154 \cdot 10^6$ | 0.14 |
| R6 | $10.067 \cdot 10^6$ | $10054 \cdot 10^6$ | 0.13 |
| R7 | $99.012 \cdot 10^6$ | $99.158 \cdot 10^6$ | 0.15 |
| R8 | $474.077 \cdot 10^6$ | $475.250 \cdot 10^6$ | 0.25 |

Table 3.1: Resistance values extrapolated from the I-V characteristics reported in Figure 3.20. The error committed is under the percent over the entire dynamic range.

the proposed setup and a Keithley 2400 Source Meter Unit (SMU) during injection of 50 *ppm* of $CO_2$ in dry air. The sensor's electrode connected to the ground was connected to the SMU through a virtual ground to perform this measurement. By doing so, the voltage difference on the sensor was the same set by the circuit in Figure 3.7, but the current circulating through the sensor was measured both by the tested circuit and by the SMU. Figure 3.21 reports the current measured by the system proposed in this work (*Measured*) and by the SMU (*Reference*).

The current measured by the system and the current recorded using the SMU are almost superimposed, with an average relative error of 0.2%.

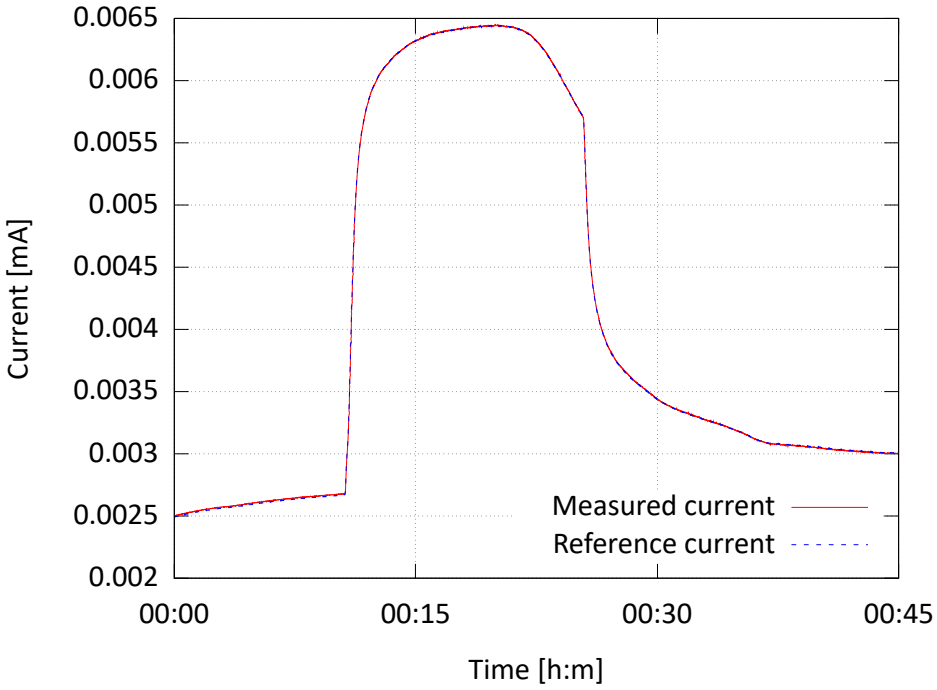


Figure 3.21: Monitor of current through an $SnO_2$ sensor at 1 $V$, heated to 300 °C, simultaneously recorded using the proposed setup (solid red line) and a Keithley 2400 (dashed blue line) during injection of 50 *ppm* of $CO_2$ in dry air. The two curves are almost superimposed.

### 3.6.7 Conclusions

In this section we discussed the development of the instrumentation for the electrical and thermal characterization of chemiresistive gas sensors exposed to a controlled atmosphere used in the *operando* DRIFT setup. We presented the hardware that composes the instrumentation, describing the modules to heat the sensor, to measure the electrical properties, and to set the operating atmosphere. It was also developed a dedicated software, written in Java, to easily acquire every significant data: voltage drop and current through the sensing film, the resistance of the sensing film, the sensor's temperature, power consumption, atmosphere temperature, and relative humidity. These are necessary to characterize a chemiresistive gas sensor. Furthermore, the acquisition of the current-voltage and the current-temperature characteristics was automated as a function of the working conditions.
To evaluate the instrumentation, it was reported the characterization of a sensor based on $SnO_2$, exposed to different concentrations of carbon monoxide diluted in dry air. The results agree with the data reported in the literature, showing a decrease in the resistance of the sensing film associated with the increase of the $CO$ concentration.
The I-V characteristic showed the non-linearity of the $SnO_2$ sensors for temperatures lower than 200 °C, highlighting the importance of the applied potential for the usage of a chemiresistive gas sensor. Moreover, it was also observed that the voltage applied to the sensing film changed the sensor performance considerably, decreasing the measurement reliability and accuracy for potentials higher than 6 $V$. Both the measure of the I-V characteristic and the monitor of the behavior of the sensor at different gas concentrations proved that the potential applied to the sensing film has a decisive role in the operation of a chemiresistive gas sensor. Therefore, an instrumentation that allows tuning the applied potential is fundamental during the test of new materials.
The measurement of the I-T characteristic for the tested sensor highlighted the typical behavior of an intrinsic semiconductor, extrapolating an activation energy $E_a$ that ranges from 0.6 $eV$ to 0.8 $eV$, depending on the measuring condition, that is comparable with values reported in the literature. It was also observed hysteresis in the passing current during the heating and cooling process for temperatures lower than 400 °C that is probably correlated with the absorption/desorption of chemical species from the sensing film.
Both from the measurement of the I-V and the I-T characteristic, it was possible to extract information about the electrical and the thermal behavior of a sensor, therefore it is emphasized that a systematic measurement of these quantities is critical in the characterization of new materials for chemiresistive gas sensors and dedicated instrumentation, as the one presented, becomes necessary. Moreover, the automation of the measurement procedures used to monitor the I-V and I-T curves is a key feature for dedicated instrumentation since it allows to acquire the evolution of the properties of a sensor during long periods of time and in different working conditions.
In conclusion, with the presented instrumentation, we have described a piece of equip-

ment capable to systematically characterize the operation of a chemiresistive gas sensor in different working conditions, and we trust that it will help the understanding of the working principles of new materials used in gas sensing.

## 3.7 Measuring protocol

Since the system for carrying out DRIFT measurements on *operando* gas sensors requires the synchronization of different software and hardware, it was defined a basic protocol for a reproducible use of the system as a whole. Some relevant problems in the use of the system concern the focusing and the alignment of the sensing film with respect to the infrared beam, the re-calibration of the detector with respect to the working temperature, and the choice of the background spectrum to be used.

### 3.7.1 Focus alignment assisted by the heater

A practical issue in carrying out DRIFT measurements on restricted areas such as the sensing film of a gas sensor concerns the focusing of the infrared beam. Indeed, although it is possible to use the infrared detector to verify the centering of the sensor to the optics, the eye-view cannot be used to verify that the beam is centered on the sensing film and not on other parts of the sensor since the infrared radiation is invisible. Therefore to set the position of the sensor correctly, it is necessary to use another type of approach. Eventually, the problem was solved by exploiting the sensor itself. Indeed, if it is positioned correctly, the sensor is completely illuminated by the infrared beam, increasing its temperature. Even though small ($\sim 1-2$ °C), this variation can be easily detected using the built-in substrate heater that works like a thermometer. Therefore, acting directly via software, it was possible to create a routine dedicated to the precise monitor of the heater resistance, allowing to reach a relative error of a few cents of *Ohm* by averaging. Indeed this measurement is very precise but not accurate. However, since we are interested in a relative variation to center the sensor, averaging is legit. Ultimately, using the positioning system on the three axes, moving the measuring chamber with respect to the DRIFT accessory makes it possible to center the infrared beam on the sensing film by directly monitoring the sensor's temperature to its displacement.

### 3.7.2 Compensation of the MCT detector with respect to the sensor temperature

A rather relevant problem in using a mercury-cadmium-telluride (MCT) photoconductive detector as a detector for DRIFT spectroscopic measurements on hot gas sensors is due to the decrease in the detector signal due to infrared radiation coming from the sample under test.

To understand how to solve this problem, one can first explain what causes the decrease of the signal in an MCT detector when the intensity of the ambient radiation increases. We report in Figure 3.22 the simplified circuit diagram used for monitoring the resistance of the photoconductive detector, which in first approximation is a simple resistive divider. In a real MCT detector, very sophisticated control circuits are used to reduce low-frequency noise (pink noise). However, the signal degradation mechanism due to ambient radiation can be introduced already by making this simplification.

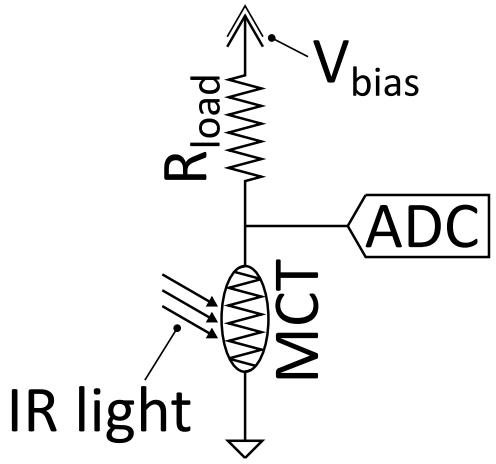


Figure 3.22: Simplified circuit for monitoring the resistance of a photoconductive MCT sensor.

Since we want to monitor the variations of the detector resistance with respect to the dark conditions (source off), the signal to be maximized is the potential variation measured by the ADC in Figure 3.22 with respect to the resistance $R_{load}$.
A variation in the resistance $\Delta R$ of the detector corresponds to a variation in the potential on the ADC:

$$\Delta V = -V \frac{R_{load} \cdot R_{detector}}{(R_{detector} + R_{load})^2} \cdot \Delta R_{detector} \tag{3.12}$$

This expression is maximized when the load resistance is equal to the resistance of the detector (dark), consequently $R_{load}$ is basically chosen to be equal to the resistance of the detector with the source off.
In the case of an incandescent sample, however, the detector is irradiated by the light coming from the sample itself, this means that the resistance with the source off is much lower than the value set in the factory that is calibrated at room temperature. Consequently, the variations in resistance due to the light coming from the source are much smaller, explaining why, from the point of view of the acquisition electronics, working at high temperature the signal acquired by the detector abruptly decreases. To

partially compensate for this effect, it is possible to modify the value of the excitation voltage $V_{Bias}$, to obtain a sufficiently high signal on the ADC. The adjustment of $V_{bias}$ when working at high temperature is therefore always necessary to partially compensate the decrease in resistance of the detector when the source is off.
Although the increase in the bias current on the detector does not physically change the system's electronics, it also causes an increase in the noise. At the same time, the light radiated by the sample decreases the detector's sensitivity due to the non-linearity of the response as a function of the intensity of the incident light. For these reasons, it is important to underline that it is better to work at low temperatures when possible , to maximize the performance of the detector and its associated electronics.
Summarizing, from a practical point of view, the set protocol of the MCT detector for measurements on temperature-resistant chemiresistive gas sensors precedes the following steps:

- The sensor to be characterized is brought to the working temperature.
- The FTIR source is switched off.
- The bias potential is modified so that the infrared emission of the sensor is partially compensated.
- It returns to the standard measurement configuration.

### 3.7.3 Background and spectra processing

In infrared spectroscopy, the spectrum of a substance is always referring to a reference spectrum, called background. The background allows making a spectrum independent of the constant parameters of the system used, including the intensity of the light source, the spectral response of the detector, and the absorption of the various elements along the system's optical path. In a DRIFT setup, however, choosing a proper background is very tricky compared to other configurations because the intensity and the spectrum of the scattered light depend on diverse parameters, such as the particle size of the powder under test and the refractive indices involved [70].
During a standard DRIFT powder measurement, the sample to be characterized is generally diluted in an IR transparent medium (e.g., $KBr$). In this way, a proper background is the spectrum of the diluting powder without the sample. However, on the sensing film of a gas sensor, it is not possible to follow the same approach, since the sensor itself would be destroyed.
The problem can be faced by following two different paths, each with advantages and disadvantages. The first way is to use an opaque metal surface (e.g., gold) as a reference to diffuse the light coming from the source in an anisotropic way. This approach has the advantage of obtaining a spectrum linked only to the components of the instrument,

however, it has proved some issues to be reproduced systematically. In fact, a metal surface adsorbs over time gases present in the atmosphere (e.g., water vapor and oxygen) and therefore compromises very precise measurements. The second mode is focused on the spectrum variations with respect to a reference state, in this case, due to the adsorption of certain chemical species on the surface. According to this approach, the spectrum before exposing the surface to gas is used as a background, highlighting in the subsequent spectra only the formation of the bonds due to the gas/film interaction. The main disadvantage of this approach is that it does not extract information concerning the bonds that make up the sensible film itself since these are generally invariant to a change of atmosphere. However, a considerable advantage of the second mode is that no physical removal of the sample from the measurement chamber is required between background and subsequent measurements, avoiding the exposure to the uncontrolled atmosphere of the laboratory and, therefore, to possible contamination. For this reason, this approach was preferred to perform DRIFT measurements on chemiresistive gas sensors.
Once defined a background to describes the system at a reference state, the spectrum of a sample can be processed in different ways, depending on the characteristics to highlight (i.e., light transmitted, absorbed or diffused). The most frequent representations are [33, 71]:

- Transmission: $T(\lambda) = \frac{I_{sample}(\lambda)}{I_{background}(\lambda)}$
- Absorption: $k(\lambda) = \log_{10} T(\lambda) = \log_{10} \frac{I_{sample}(\lambda)}{I_{background}(\lambda)}$
- *Kubelka-Munk*: $\frac{k(\lambda)}{s(\lambda)} = \frac{(1-R_\infty(\lambda))^2}{2 \cdot R_\infty(\lambda)} = \frac{(1-\frac{I_{sample}(\lambda)}{I_{background}(\lambda)})^2}{2 \cdot \frac{I_{sample}(\lambda)}{I_{background}(\lambda)}}$

where $I_{sample}(\lambda)$ and $I_{background}(\lambda)$ are the spectra of the sample and the background at a given wavelength $\lambda$, and $k(\lambda)$ and $s(\lambda)$ are the absorption coefficient, and the scattering coefficient, respectively. A representation is simply a transformation on the spectra. The right representation to use depends on the theoretical context in which a specific experiment is framed.
The absorption spectrum, for example, is used when the IR beam completely crosses a sample and, according to the *Beer-Lambert* approximation, allows quantification of the composition of an unknown sample.
In a standard DRIFT measurement, the spectrum of a sample is usually represented using the *Kubelka-Munk* transformation. The *Kubelka-Munk* theory associates the relative intensity of light scatted from a powder $R_\infty(\lambda)$ to the ratio between the absorption coefficient $k(\lambda)$ and the scattering coefficient $s(\lambda)$. If the scattering coefficient is independent on $\lambda$, *Kubelka-Munk*'s theory leads back to the *Beer-Lambert* approximation, and therefore allows a raw quantification.

However, to exploit *Kubelka-Munk*'s theory, some experimental conditions must be met, such as the thickness of the sample that has to be large compared to the depth of penetration of the incident light.
The sensing film of a chemiresistive gas sensor does not meet this condition, since it is very thin compared to the penetration depth of the infrared light, for this reason the *Kubelka-Munk* transformation could be misleading to represent the spectra in our *operando* DRIFT setup.
Therefore, we have chosen not to use *Kubelka-Munk* transformation. Instead, we have chosen a representation that is analytically equivalent to absorption, in which $I_{sample}$ is substituted by the diffused light $R_{sample}(\lambda)$. Clearly, the spectrum represented in this form is not related to *Beer-Lambert* approximation. However, though qualitatively, it allows highlighting the formation or breaking of chemical bonds similarly, that is, by the formation of peaks or valleys at a given wavelength.

## 3.8 Validation of the setup

### 3.8.1 Fluid dynamic and residence time distribution

To evaluate the gas flow dynamics within the *operando* chamber, a CFD modeling study was performed as described in section 3.4.1. The results in Figure 3.23 show flow velocity vectors when the gas is injected in the reaction chamber above the sensing film.

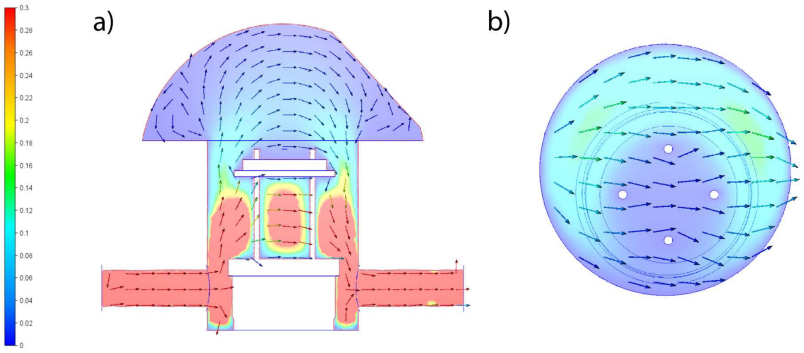


Figure 3.23: (a) Side and (b) top view of the velocity magnitude obtained via CFD simulation (in $\frac{cm}{s}$). Conditions: Air carrier, 25 °C with a constant flow of 100 *sccm*.

At 100 *sccm* of inlet flow rate, the average velocity magnitude is fairly constant and relatively low in the volume above the sensing film. Figure 3.23 (a) and (b) show that the flow path is distributed over the entire sensing film, which guarantees a relatively uniform sample surface coverage during spectroscopic evaluation. Following the CFD simulation at RT of the reaction cell, the system could be considered an ideal Laminar

Flow Reactor (LFR). The choice of the laminar flow model is justified by the assessment of the Reynolds number, which is equal to $Re = 29.87$ for a flow rate of 100 *sccm* and therefore much lower than the critical Reynolds number for ideal laminar flow of 2000 [47]. To further gain information about the fluid dynamics of the designed chamber, it is useful to estimate the mean residence time (MRT). Data obtained from CFD simulation highlighted an MRT of 2.58 *seconds* for the ideal reactor. Indeed, the experimental $E(t)$ (see section 3.4.1) function of a water vapor stepped response at room temperature (RT) and 300 °C were fitted and compared to several ideal models, including a laminar flow reactor (LFR), a Continuous-flow Stirred-Tank Reactor (CSTR), and a combined CSTR+LFR (Figure 3.24) [54].

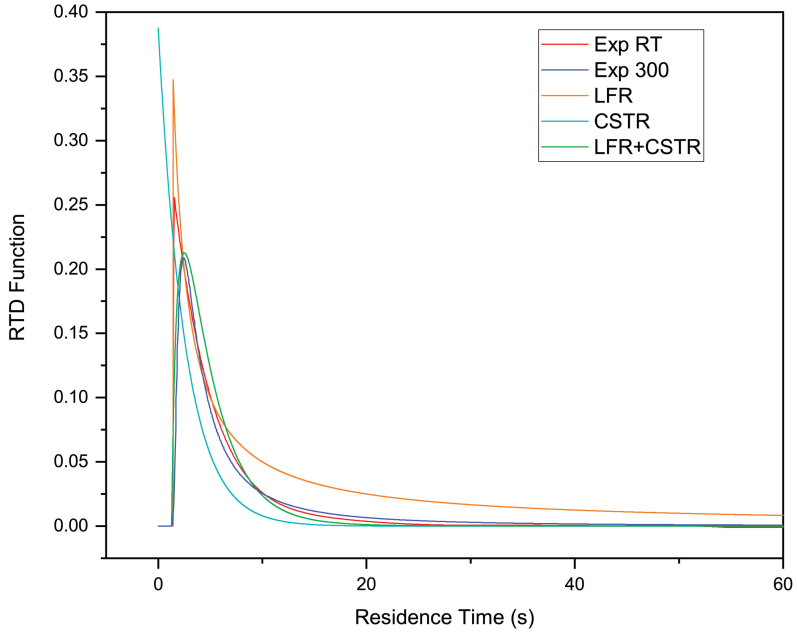


Figure 3.24: RTD profiles of water vapor stepped response through the reaction cell, and corresponding fitted RTD reactor models, LFR in orange, CSTR in light blue, and combined CSTR+LFR in green. Experimental residence time distribution data at RT in red and at 300 °C in blue, respectively. Conditions: 1 *atm*, dry air carrier flow of 100 *sccm*.

The results demonstrate, as expected that an LFR model could describe the RTD function at RT. However, at a working temperature of 300 °C, the $E(t)$ function is better defined by a combined CSTR+LFR, suggesting that the *operando* chamber fluid dynamics has a more complex flow distribution.

### 3.8.2 Temperature gradient measurements

An insight into temperature gradient in a reaction cell used for transmission FTIR analysis was previously reported in the literature, recalling that understanding the thermal properties of a catalytic chamber is of great importance [72]. The temperatures in the chamber were monitored via two systems: the first one on the sensor via the calibrated $Pt$ heater, and the second one monitored at the base of the chamber via a Sensirion SHT3X temperature/RH sensor. Temperature differences can exist inside reaction chambers and are accentuated by heat losses via conductive, radiative, and convective transport [73]. Figure 3.25 shows the correlation between the sensing film and the measurement chamber temperatures, where it can be noted that nitrogen ($C_pN_2 = 1.040Jg^{-1} \cdot K^{-1}$) gas flow, which possesses a higher heat capacity than air ($C_pAir = 1.012J \cdot g^{-1} \cdot K^{-1}$), tends to facilitate heat transport and losses. However, heat transport is efficient under applied gas-flowing conditions and the sensing chamber performed well over a wide range of temperatures for most gas sensing-related applications.

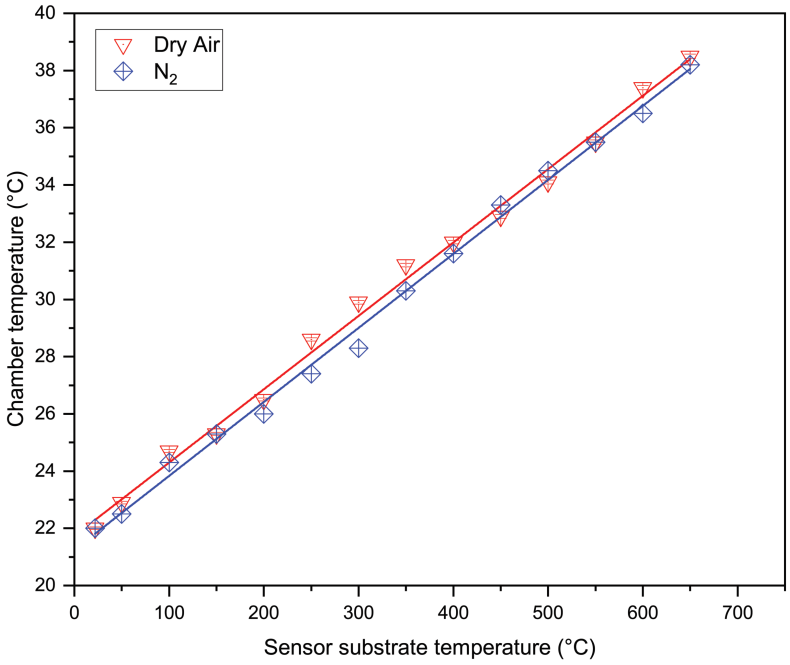


Figure 3.25: Relation between the temperature of the sensor substrate and temperature of the atmosphere inside the reaction cell under 100 *sccm* both dry air and nitrogen flow.

### 3.8.3 Operando DRIFT experiment

Figure 3.26 shows the resistance change of the sensor with marked time intervals, in which the reference (background) and sample spectrum were acquired.

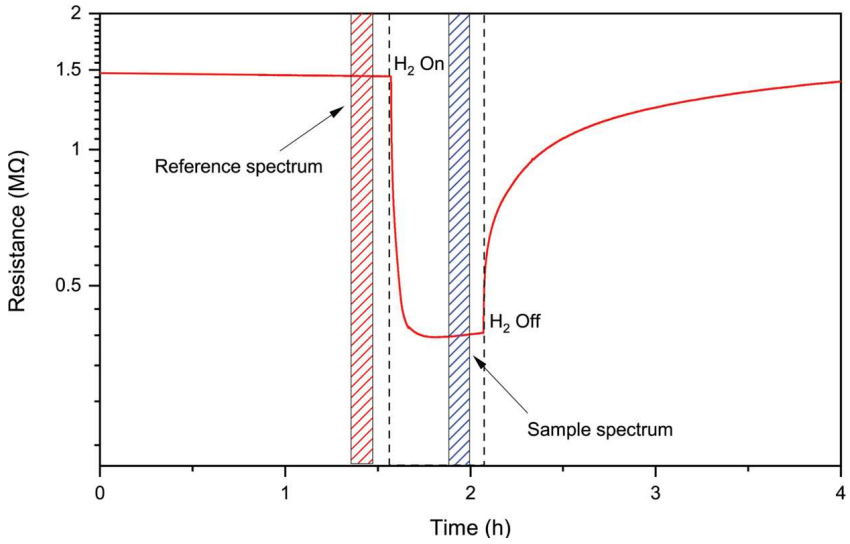


Figure 3.26: Measurement scheme, resistance change of the $SnO_2$ gas sensor exposed to 500 *ppm* of $H_2$ in dry air at 300 °C with marked time intervals for the FTIR spectrum sampling

Figure 3.27 shows the single-channel spectrum of the sensor operated in dry air at 300 °C, that is, the direct spectrum obtained by the FTIR (without background normalization).

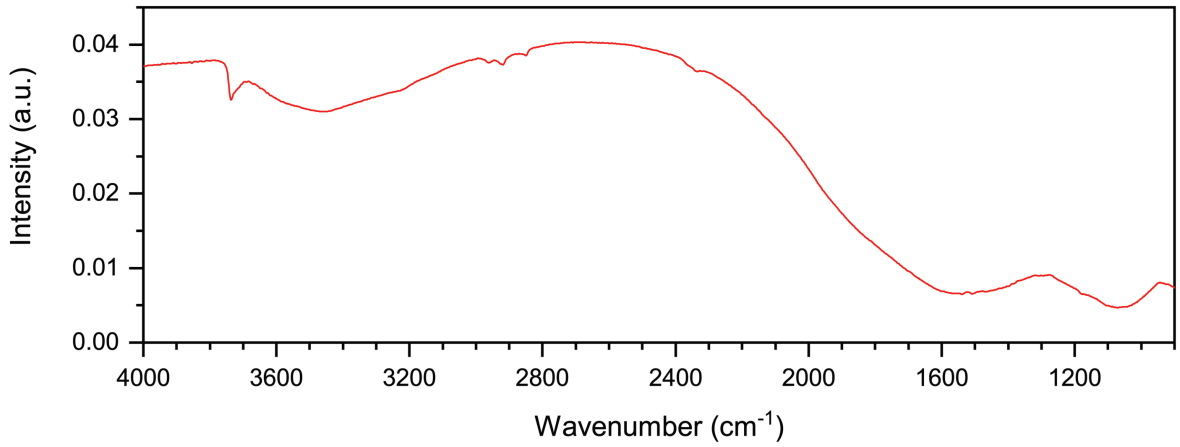


Figure 3.27: Single-channel spectrum of a $SnO_2$ gas sensor.

This spectrum overlaps information from the instrument and from the sample, however, assuming a smooth shape of the spectrum without the sample, it is possible to extract some qualitative features about the sample spectrum. As expected, the sample exhibits distinctive characteristics of $SnO_2$ surface. Indeed, the existence of isolated hydroxyl groups at the material's surface is suggested by the presence of a sharp band at 3737 $cm^{-1}$, while bridged (interacting) hydroxyls can be assigned to the typical broad bands between 3600 and 3000 $cm^{-1}$ [74]. The three bands between 3000 and 2800 $cm^{-1}$ are due to hydrocarbon impurities of the optical system and canceled when calculating the absorbance spectrum [75]. The bands between 1600 and 1000 $cm^{-1}$ are assigned to hydroxyl deformation vibrations and $SnO$ lattice vibrations overtones. Besides, some peaks appear between 1000 and 900 $cm^{-1}$, and they can be assigned to hydroxyl deformation vibrations. The overall shape of single-channel spectrum measured on $SnO_2$ exposed to dry air is composed by the absorption caused by functional groups of species adsorbed on the surface and the $SnO_2$ material itself, which, together with the diverse individual parameters that compose the spectrometer (optical component, light source emission, and detector non-linearity) affect the overall shape of the single-channel IR spectrum [76]. In line with the well-known surface reaction mechanism, the reception of $H_2$ occurs by the oxidation of $H_2$ to $H_2O$ via a *Mars-van-Krevelen-like* mechanism, creating oxygen vacancies, which act as electron donors [77]. According to these findings, one would expect various interactions in oxygen-related bands, namely changes in the hydroxyl groups and $Sn - O$ vibration bands and their overtones. Figure 3.28 shows DRIFT spectrum recorded during the exposure of $H_2$ in dry conditions that demonstrates, as predicted, a decrease of the hydroxyl and lattice oxygen species-related bands (3737 and 3715 $cm^{-1}$).

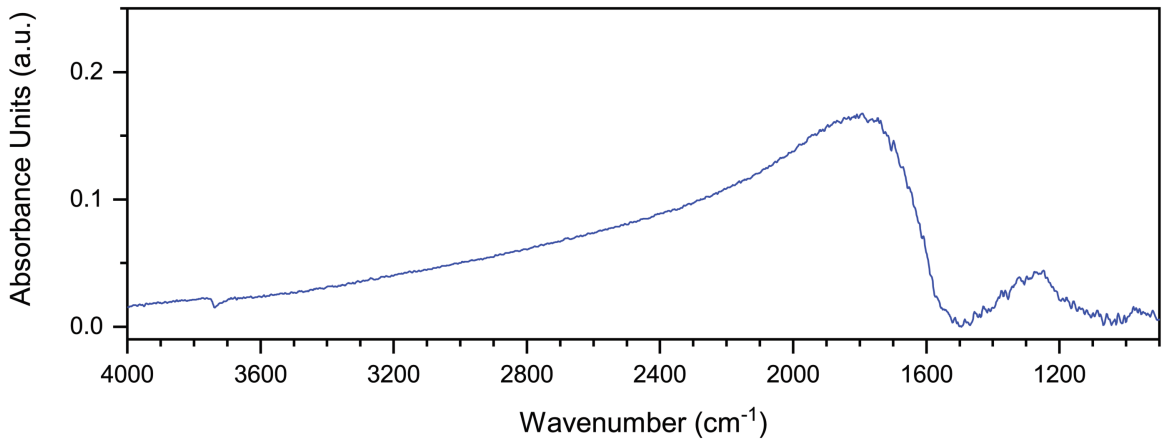


Figure 3.28: Absorbance spectrum of a $SnO_2$ gas sensor exposed to 500 *ppm* of $H_2$ in dry air.

The decrease of the hydroxyl concentration during test gas exposure is elucidated by the equilibrium between surface oxygen and hydroxyl groups with inevitable residual water vapor background (even in dry air). The overall shape of the spectrum is dictated by the absorption of free charge carriers, which are dramatically changed during $H_2$ exposure [74]. This shows a strong rise in absorbance below 2300 $cm^{-1}$ region. In addition, $SnO_2$ exposure to reducing gases like $H_2$ leads to a decrease in intensity of a series of bands between 1500 and 1000 $cm^{-1}$. The identification of these bands is not well-defined since $Sn - O$ overtones and hydroxyl deformation vibrations arise in ì this region. In order to differentiate between those bands, isotopic exchange studies need to be performed. However, the aforementioned experiments and a detailed description of this observation are out of the scope of this section.

## 3.9 Conclusions

This chapter discussed the developed and characterized a new chamber for *operando* DRIFT studies on chemiresistive gas sensing films. The chamber is compatible with Harrick Scientific's diffuse reflectance accessory, and it could be adapted for use with UV-visible and Raman spectroscopy setups by changing dome or windows material. It was demonstrated by residence time distribution stepped experiments and CFD simulation that the reaction cell flow dynamics possesses elements of laminar flow at RT and LFR+CSTR behavior when the sensor is heated at its proper working temperature. The reaction cell presented mean residence times of about 2.58 seconds at a gas flow rate of 100 *sccm*. Finally, we validated *operando* DRIFT measurements confirming the already well-known sensing mechanism of $SnO_2$ vs. 500 *ppm* of $H_2$ in dry conditions. In summary, the main advantages of the present design concerning other available setups rely on:

- 3-axes alignment system that allows obtaining a precise positioning of the gas sensor, even in the presence of small devices,
- possibly perform DRIFT measurements on solid-state gas sensors with an active area of 1 $mm^2$,
- development of a custom-made acquisition system with temperature and humidity monitoring inside the reaction cell,
- the capability of obtaining a reliable spectrum at high operating temperature due to the use of a small substrate and careful calibration of the MCT detector.

Overall, we believe that this study can play a supporting role for the sensors community by introducing a reliable characterization tool that can be easily reproduced,

implemented, and adapted for several types of substrates, such as $Al_2O_3$, Micro-Electro-Mechanical Systems (MEMS), and quartz substrate, that can help discriminate surface species for numerous gas–solid-phase reactions.

# Chapter 4

# $SO_2$ sensing mechanism of nanostructured $SiC - SiOC$ core shell: an *operando* DRIFT investigation

## 4.1 Introduction

The monitoring of greenhouse and polluting gases has recently granted increasing importance in the field of sensors [28]. Indeed, the ability to monitor the composition of the atmosphere by using low-cost and straightforward systems has become fundamental in many application fields, from checking the compliance with safety conditions in the industrial workplace, to indoor air quality monitoring [78, 3, 79, 80, 1]. Chemiresistive gas sensors have gained great attention to these applications, exploiting the resistivity changes of a sensing material when exposed to different concentrations of gases [26]. The majority of employed materials for producing chemiresistive gas sensors are metal oxides (i.e., tin oxide, zinc oxide, tungsten oxide, etc.) [26, 81]. However, different types of semiconductors have been studied, both pristine or decorated with catalysts (i.e., noble metals), used to improve specific properties [26, 27].
Despite the progress made in the synthesis of innovative sensing materials, the majority of chemiresistive gas sensors still show a series of drawbacks, such as the lack of selectivity and long-term stability, compromising the reliability of the devices. In this scenario, the silicon carbide ($SiC$) employed in the form of nanoparticles as a functional material for the manufacturing of chemiresistive gas sensors has shown some peculiar properties. In particular, silicon carbide was proved to be selective in the detection of sulfur dioxide and reliable in wet (relative humidity $RH\% > 0$) environments [21]. In the broad palette of harmful gases, particular interest is covered by those of anthropogenic origin,

and sulfur dioxide ($SO_2$) holds an important position [82, 83]. Indeed, it is dangerous for humans, with a threshold limit value/short-term exposure (TLV/STEL) of 1 *ppm* [84] and is responsible for acid rains. Therefore, the monitoring of $SO_2$ is fundamental in many areas [85, 86].
The interest to detect sulfur dioxide and the unique properties of silicon carbide in being selective to this gas has increased the attention in chemiresistive gas sensors based on silicon carbide, even if good performances were obtained only at high working temperature for standard gas sensors (i.e. 650 °C).
Indeed, in our previous work, it was observed that at operating temperature up to 650 °C, the $SiC$ nanoparticles oxidized, covering the surface with an amorphous shell of $SiO_xC$ [21, 87]. However, the role of oxidation in the operation of the sensors has not been extensively investigated, simply assuming a relationship between the amount of oxide and the sensing performance. Then, this work seeks to investigate the role of the oxide in the silicon carbide sensing mechanism.
To achieve this goal, it was developed a method to fabricate uncontaminated sensing film of $SiC$ nanoparticle to be used as a gas sensor. Subsequently, the electrical properties of the sensors, before and after the oxidation of $SiC$ nanoparticles, were studied through the current-voltage curves (I-V characteristic) and the current-temperature curves (I-T characteristic). It is also reported the energy dispersion x-ray spectrum (EDX) analysis of the powder before and after the oxidation to verify the composition of the sensing film during the measurements. To investigate the mechanism of the oxide formation on $SiC$ nanoparticles, *operando* diffuse reflectance infrared Fourier transform (DRIFT) spectroscopy was acquired at increasing temperature. Finally, the same technique was used to characterize the sensor during the exposure to $SO_2$ at different working conditions, highlighting differences in the sensing mechanism between the dry and wet atmosphere. Based on the results obtained from these measurements, a physico-chemical model is proposed to interpret the sensing mechanism of an oxidized film of silicon carbide nanoparticles.

## 4.2 Materials and Methods

The experiment was organized in three parts which were performed consecutively:

1. *Operando* DRIFT analysis of the sensing film of a $SiC$ gas sensor as the temperature increases in synthetic dry air environment (*in situ* oxidation of $SiC$ nanoparticles).

2. Electric and thermoelectric characterization of the $SiC$ sensing film, before and after oxidation, in dry condition.

3. Response to $SO_2$ in dry and wet environments with *operando* DRIFT analysis.

Every reported measurement refers to a single device to avoid slight differences between similar sensors. However, all the devices tested showed identical behavior.

### 4.2.1 Preparation and characterization of silicon carbide nanoparticles

Commercially available $SiC$ nanopowder from PlasmaChem was used for this study. According to specifications, the average size of the particles was $20 \pm 7$ $nm$ with a purity $> 98\%$. Declared contaminations were principally due to oxygen ($< 1.25$ %) and chlorine (0.25 %) [88]. Since one of the goals of this study concerns the oxidation of the silicon carbide nanoparticles, to exclude the presence of any oxide on the starting samples, the powder as received was treated in diluted (10%) hydrofluoric acid for about five hours, to remove any trace of silica on the nanoparticles. Subsequently, the treated powder was cleaned with repeated washing in demineralized water and vacuum filtered. Finally, the powder was dried on a hot plate for one night at a temperature of 100 °C and collected in a vial for sensor fabrication. The morphology and the composition of the treated powder were measured using a ZEISS Evo LS10 scanning electron microscope (SEM) equipped with a Bruker Quantax 200 energy dispersive x-ray (EDX) spectrometer [89]. Other analyses reporting the structural characterization of the same powder are reported in our previous work [21].

### 4.2.2 Sensor manufacturing

The treated powder was used to manufacture the sensors, composed of a sensing film 10 $\mu m$ thick, deposited on the top of an alumina substrate [24].
The substrates are made of a square die of a side of 2.5 $mm$, with a thickness of 150 $\mu m$ and are structured to perform the double function of both electrically connecting the sensing film and setting the temperature of the sensor. The sensing film contacts are made by using two interdigitated gold electrodes embedded inside the top of the substrate. At the same time, the operating temperature is set using a heater built on the

rear side of the substrate. The heater is a platinum serpentine with a nominal electrical resistance about 12 Ω at room temperature, which is used both to supply power to the sensor and measure its temperature, exploiting the relationship that links the temperature to the electrical resistance [61].
The sensing film is obtained through a combined technique of spray and spin coating. Using this method, a liquid mixture containing the silicon carbide nanoparticles is sprayed (spray coating) on a substrate spinning at high speed (spin coating). Figure 4.1a shows the structure of a mounted sensor, and Figure 4.1b shows the setup used to spray/spin coat the silicon carbide films.

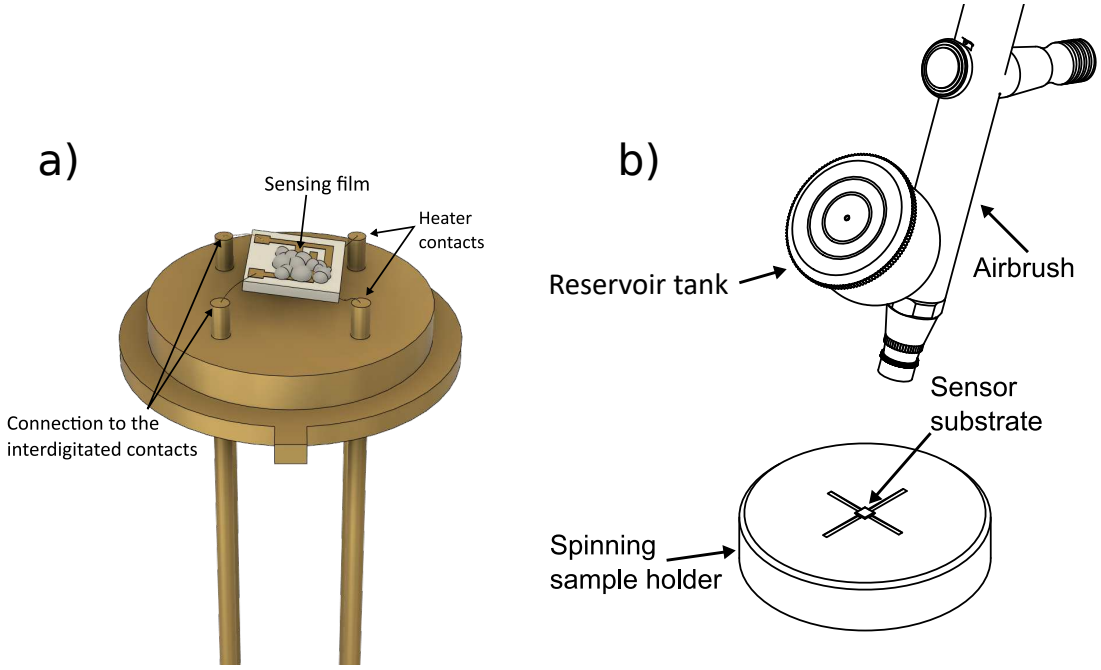


Figure 4.1: (a) Structure of a mounted sensor. (b) The spin/spray setup used for the deposition of the sensing film of silicon carbide nanoparticles. The setup is composed of a manual airbrush coupled with a spin-coater equipped with a custom 3D printed substrate holder.

The combination of these two techniques allows increasing the uniformity of the obtained films. Indeed the spray coating allows to uniformly disperse the nanoparticles while the rotation at high speed avoids the formation of unwanted aggregates.
For the deposition of the $SiC$ nanoparticles, the best results were obtained by using a dispersed solution of isopropyl alcohol with a 5 $\frac{g}{l}$ ratio. The mixture was placed in an ultrasonic bath for about one hour before the deposition to better suspend the particles. To avoid contamination that could compromise subsequent measurements, no binder, neither organic nor inorganic, were used.

Both the working pressure of the spray and the speed of the spin coater significantly influence the quality of the films obtained. In the setup used, the air pressure was set at 2 $atm$, while the spin coater speed was set at 4500 $rpm$, for approximately 5 minutes. Figure 4.2 shows the silicon carbide film of the sensors manufactured with this technique under the optical microscope.

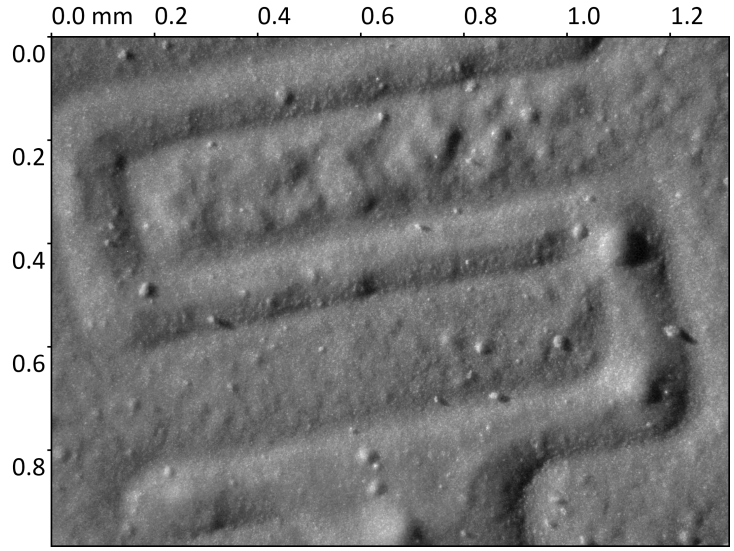


Figure 4.2: Optical picture of the $SiC$ sensing film deposited with the described spin-spray coating setup.

The final devices are formed by sensing film and substrate and are mounted suspended on a standard TO-39 package using four 50 $\mu m$ diameter gold wires, which electrically and mechanically connect the sensors, as shown in Figure 4.1a.

### 4.2.3 Electrical characterization of chemiresistive gas sensors

The electrical behavior of the $SiC$-based sensor was studied with respect to the voltage (I-V characteristic) and the working temperature (I-T characteristic), both with increasing and decreasing steps. The device was characterized both before and after the oxidation ramp. During the measurements, the sensors were kept in an inert nitrogen atmosphere to avoid the uncontrolled oxidation as the temperature increases. The measurement of the I-V characteristic was acquired with increasing steps of 0.1 V per second, while the measurement of the I-T characteristic was acquired with increasing steps of 1 °C every 10 seconds. The increase rate was chosen to minimize the error due to the stabilization times.
The electrical activity of the oxidized SiC-based sensor was evaluated after retaining the device at 700 °C for a week under a 100 sccm flow of dry air and an applied voltage

between the electrodes of 5 $V$. After this further thermal process, necessary to obtain a sufficiently stable electrical signal for reproducible sensing measurements the EDX spectrum of the sensor was measured. Aftwer that, the response of the sensor was acquired at a 650 °C, waiting a few hours for the baseline to reach the equilibrium, testing both in dry ($\sim$ 0% $RH$) and in wet conditions ($\sim$ 8% $RH$) in a flow of 100 $sccm$ of synthetic air with a $SO_2$ concentration of 25 $ppm$. The humidity inside the chamber was controlled by bubbling a part of the synthetic air into bubbler filled with demineralized water. The relative humidity of 8% corresponds to the maximum value that was possible to obtain, in fact the sensor at 650 °C heats the measuring chamber up to 60 °C and this limits the maximum humidity achievable using this the setup.
The response is defined as the relative variation of an appropriate physical quantity (e.g., resistance, conductance, circulating current, etc.) *vs.* the exposure to an analyte (i.e., tested gas) [32]. Indicating this physical quantity as $X$, the response can be defined by the formula:

$$Response = \left| \frac{(X_{Air} - X)}{X_{Air}} \right| \tag{4.1}$$

where $X$ and $X_{Air}$ are the monitored quantity when the sensor is exposed or not to the analyte, respectively. In this work, the response of the sensors was calculated by replacing $X$ with the current circulating through the sensing film at a fixed potential so that the eq. 4.1 becomes:

$$Response = \left| \frac{(I_{Air} - I)}{I_{Air}} \right| \tag{4.2}$$

where $I$ and $I_{Air}$ are the current at a fixed potential with and without the analyte, respectively. We decided to use the current instead of the resistance to calculate the response since a non-linear current-voltage characteristic was measured. In this way, the response is made explicitly dependent on the applied potential [90].

### 4.2.4 *Operando* DRIFT characterization setup

In order to observe the evolution of the chemical bonds on the surface of the sensing film, a modified DRIFT setup was employed, which allows driving the sensor and simultaneously acquire the DRIFT spectrum of its sensing film [55]. *Operando* experiments were done using Bruker Vertex v70 FTIR spectrometer, equipped with a DRIFT accessory (Praying Mantis, Harrick Scientific Products Inc.). The spectra were acquired using a liquid nitrogen-cooled mercury cadmium tellurium (MCT) mid-band detector, whose spectral range is from 850 $cm^{-1}$ to 5000 $cm^{-1}$.
Each spectrum is an average of 20 minutes of acquisition, with a spectral resolution of 4 $cm^{-1}$. Absorbance spectra were calculated as apparent absorbance using the spectra recorded in reference conditions:

$$A(\lambda) = \log_{10} \frac{I_{sample}(\lambda)}{I_{background}(\lambda)} \tag{4.3}$$

where $I_{sample(\lambda)}$ and $I_{background}(\lambda)$ are the spectra of the sample and the background at a given wavelength $\lambda$. Each reference spectrum was recorded directly prior to gas/vapor exposure, as reported in [55]. It is important to highlight that in a standard DRIFT measurement, the spectrum of a sample is usually represented using the Kubelka-Munk transformation [71]. However, in the case of a chemiresistive gas sensor the experimental conditions required by Kubelka-Munk theory are not fully accomplished since the scattering of incident light is not isotropic and the light distribution does not show a purely diffusive character within the layer when multiple scattering processes occurs.
The electrical properties of the sensing film were monitored using a custom instrumentation that integrates also the electronics necessary to drive the temperature of the sensor. Four mass-flow controllers (MFC) from Brooks are used to set the working atmosphere, each of which controls the flow of various gas in the measurement chamber. A detailed description of this equipment, both regarding the specifications and its implementation, is described in [90].

## 4.3 Results

### 4.3.1 SiC-nps morphology and composition

Figure 4.3 reports the SEM image (a) and the EDX spectrum (b) of the $SiC$ treated powder after the washing process described in Section 4.2.1. Within the detection limit of the instrumentation, the treated powder is almost free from oxide, as the peak associated with oxygen ($K_\alpha = 0.525\ keV$) is negligible compared to the other peaks.
In the SEM image (Figure 4.3a), the treated particles appear as irregular grains of average size comparable to the size reported by PlasmaChem.

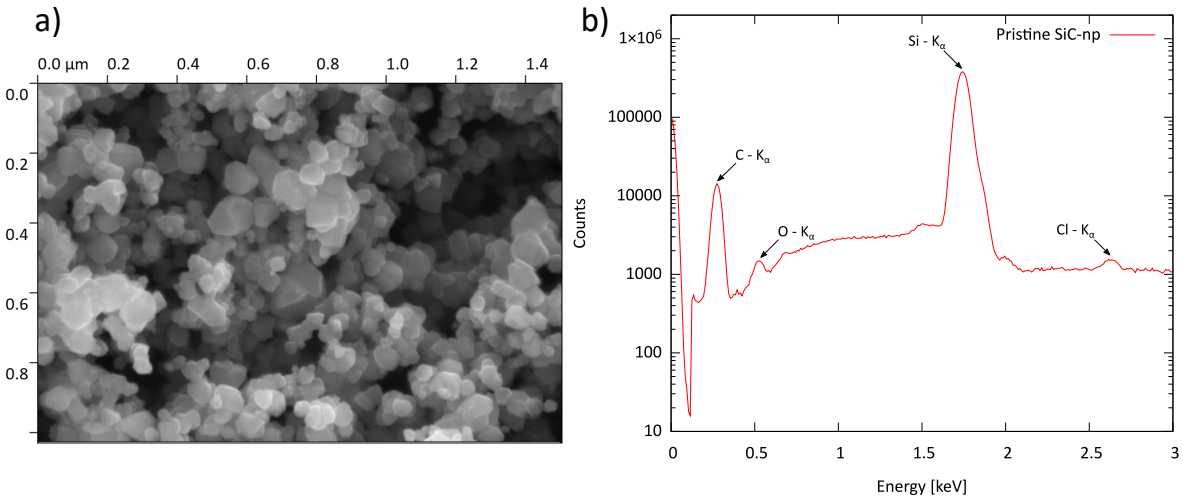


Figure 4.3: SEM (a) and EDX spectra (b) of the silicon carbide powder after washing in hydrofluoric acid 10%. Some impurities of oxygen and chlorine are present within the detection limit of the instrument ($< 1\%$).

### 4.3.2 *In situ* oxidation of SiC-nps

$SiC$-based sensor performance are supposed to be related with the quantity of oxide covering the particles, so it becomes fundamental to find the condition for which the oxidation on the sensors starts. Indeed this allows to tune the best procedure to obtain reliable sensors.
At high temperature, the $SiC$ oxidation, occurs spontaneously in the presence of gaseous oxygen and, depending on the thermodynamic conditions, this reaction can be defined as active or passive. Active oxidation produces only gaseous oxides, which are carbon monoxide and volatile sub-oxide silica, respectively, while passive oxidation forms solid silica. Since our previous thermogravimetric analysis demonstrated an increase of weight

during oxidation, we can assume a passive oxidation regime for $SiC$ nanoparticles [91]. In dry environment, the reaction that describes the passive oxidation of silicon carbide is:

$$2SiC(s) + 3O_2(g) \longrightarrow 2SiO_2(s) + 2CO(g) \tag{4.4}$$

This reaction is of great interest for various applications, and for this reason many theoretical models have been developed to describe its kinetics [92, 93], which is mainly mediated by the diffusion speed of the gaseous compounds inside and outside the formed oxide layer.
Using the *operando* DRIFT equipment described in the previous paragraphs, we investigate the oxidation layer of the $SiC$ nps that compose the sensor, gradually increasing the working temperature of the device.
The reaction (4.4) involves different material phases, then an interface exists between the newly formed oxide and the reacting $SiC$. In this state, the oxide layer is composed by a mixture of amorphous, non stoichiometric silicon dioxide, described in general terms according to the formulas $SiO_x/SiO_xC$. It is also expected that some carbon monoxide/dioxide, diffusing out from the oxide/SiC interface, will be present partially physisorbed on the surface.
To avoid unpredictable reactions with gases adsorbed at the surface of the sensing film, this was degassed in nitrogen flow at an operating temperature of 300 °C for one day. The entire degassing procedure was carried out inside the measuring chamber to avoid contamination due to the transfer of the sensors.
During the oxidation process, the measuring chamber was kept in a constant flow of 100 *sccm* of synthetic air (20 % $O_2$, 80 % $N_2$) while temperature of the sensor applied to each spectrum acquisition was maintained for one hour, and gradually increased with steps of 100 °C.
Figure 4.4a shows the evolution of the DRIFT spectrum of the sensor during the increase of the temperature (Figure 4.4b).

The spectra in the Figure 4.4b were acquired after the cooling of the sensor at room temperature. The acquisition of the spectra at a temperature lower than the operating temperature has allowed both to avoid the saturation of the detector due to the infrared emission of the sensor itself and to reduce the thermal noise. This experimental procedure allows to reach a steady state condition at room temperature since the kinetics of the reaction (4.4) is inhibited. The background used for the calculation of the relative IR absorption was acquired before the beginning of the oxidation reaction, named *background* step in Figure 4.4. This background allows to highlight the formation or the breaking of chemical bonds during the increase of the temperature, by the formation of peaks or valleys in the spectrum, respectively.
From a phenomenological point of view, starting from low temperatures, the formation of a series of peaks and valley in the wavelength range between 1000 $cm^{-1}$ 800 $cm^{-1}$ can

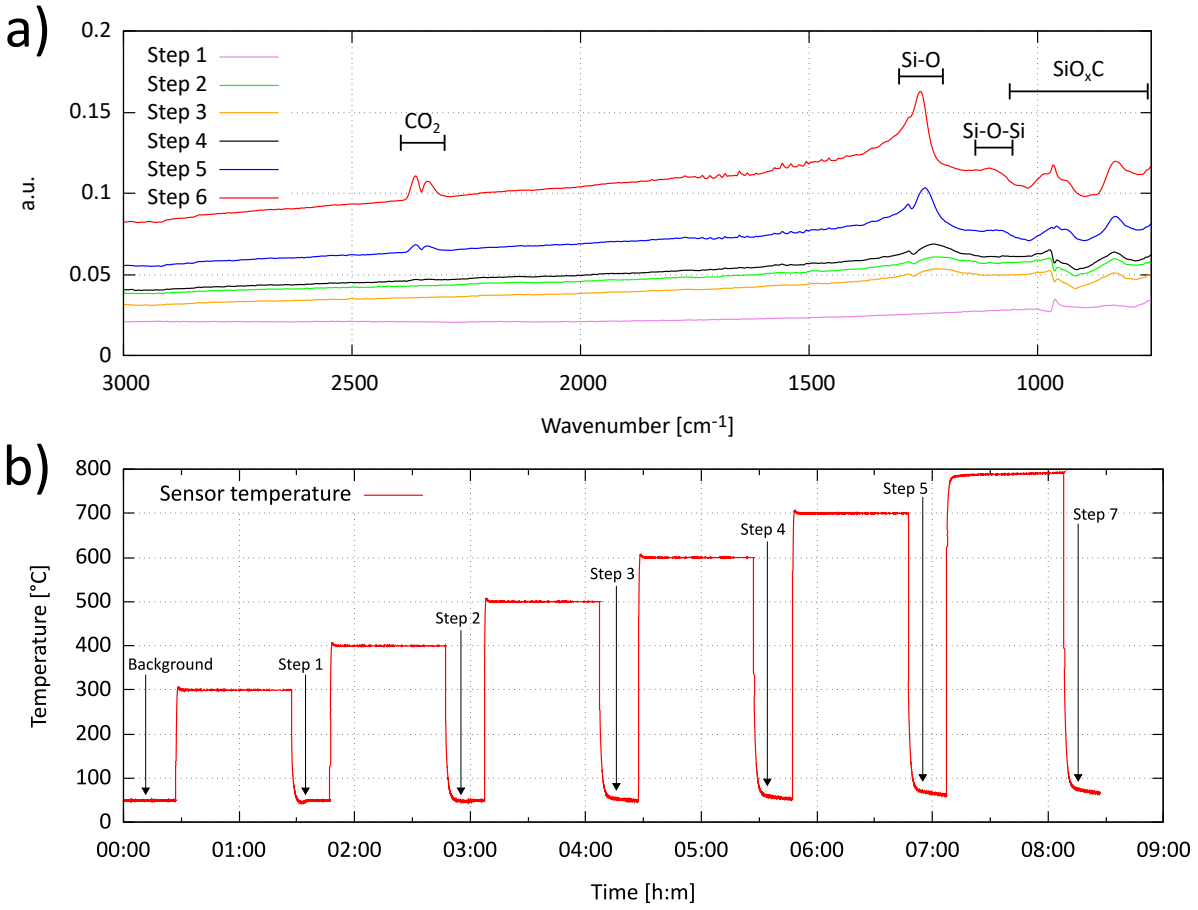


Figure 4.4: The figure on the top reports the evolution of the DRIFT spectrum during the increase of the temperature of a pristine silicon carbide based sensor. The figure on the bottom shows the corresponding time and temperature at which a spectrum is acquired.

be observed, while the formation of four peaks at 1260 $cm^{-1}$, 1110 $cm^{-1}$ and a doublet at $2330 - 2360$ $cm^{-1}$ can be seen as the temperature increases.
The peaks between 1000 $cm^{-1}$ and 800 $cm^{-1}$ are generally associated with the formation of $SiO - C$, $Si - OC$ bonds [94] and this is consistent with the formation of a $SiO_xC$ layer over the $SiC$ $nps$. The peaks observed with increasing temperatures, at 1260 $cm^{-1}$ and 1110 $cm^{-1}$, respectively, are instead associated with the silicon oxide [94, 95, 21], while the doublet at $2330 - 2360$ $cm^{-1}$ is due to the formation of $CO_2$ [96], that is a product of the reaction of the $CO$ generated by the the oxidation of the silicon carbide. In conclusion, from the spectra reported in Figure 4.4 we can assume that the oxidation of the silicon carbide nanoparticle starts in the form of a $SiO_xC$ layer for temperatures lower than 500 °C, but at higher temperature the percentage of $SiO_x$, visible as $Si - O$,

becomes predominant. The oxidation of *SiC-nps* can be also monitored through conductivity of the sensing film as the temperature increases, this measure is reported in the supporting information, showing a dramatic decrease of the conductance after $\sim$ 500 °C.

Figure 4.5 shows the current through the sensing film during the oxidation cycle shown in Figure 4.4b.

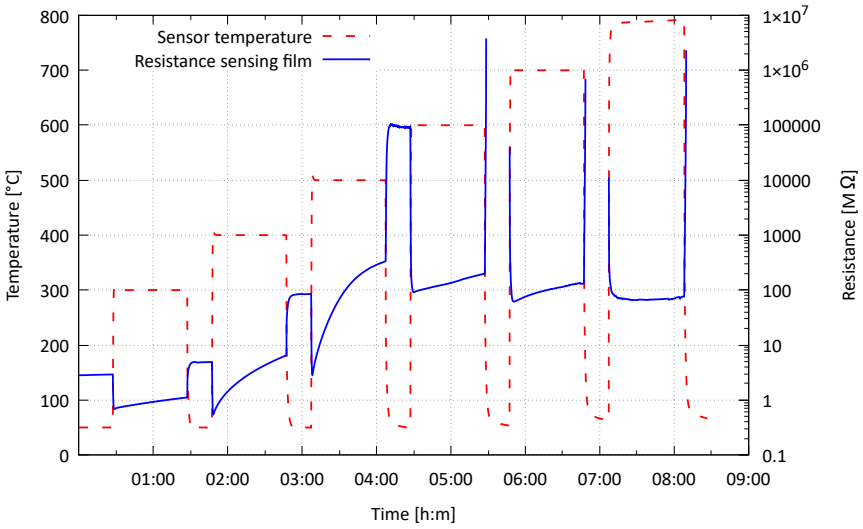


Figure 4.5: Current through the sensing film (solid blue line) at increasing temperature (dashed red line). After the step at 500 °C, the resistance increases drastically.

Excluding the intervals in which the temperature is lowered to room temperature, necessary to optimize the DRIFT measurement, a drastic increase in the resistance is visible after 500 °C , confirming DRIFT measurements shown in Figure 4.4.

### 4.3.3 Electrical properties: I-V and I-T characteristics

Figure 4.6 shows the I-V characteristic before and after the oxidation of the $SiC - nps$.

The I-V characteristic of not-oxidized SiC-based sensor has been acquired at room temperature, while the I-V characteristic of the oxidized sensor, since the current measured at ambient temperature is below the reliability threshold of the instrumentation ($\sim$ 100 $pA$ ), has been acquired at working temperature of 350 °C.

The non-oxidized sensor (Figure 4.6a) presents a linear characteristic between +10 and $-10$ $V$, with a film resistance of 540 $k\Omega$ at room temperature. The oxidized sensor, reported in Figure 4.6b, has different characteristics. In particular a dramatic increase in the resistance of the sensor can be observed, reaching an average value of 6.8 $G\Omega$ at 350 °C in the range from +10 to $-10$ $V$. One can also observe the non-linear trend with respect to the applied potential and the presence of a hysteresis depending on the

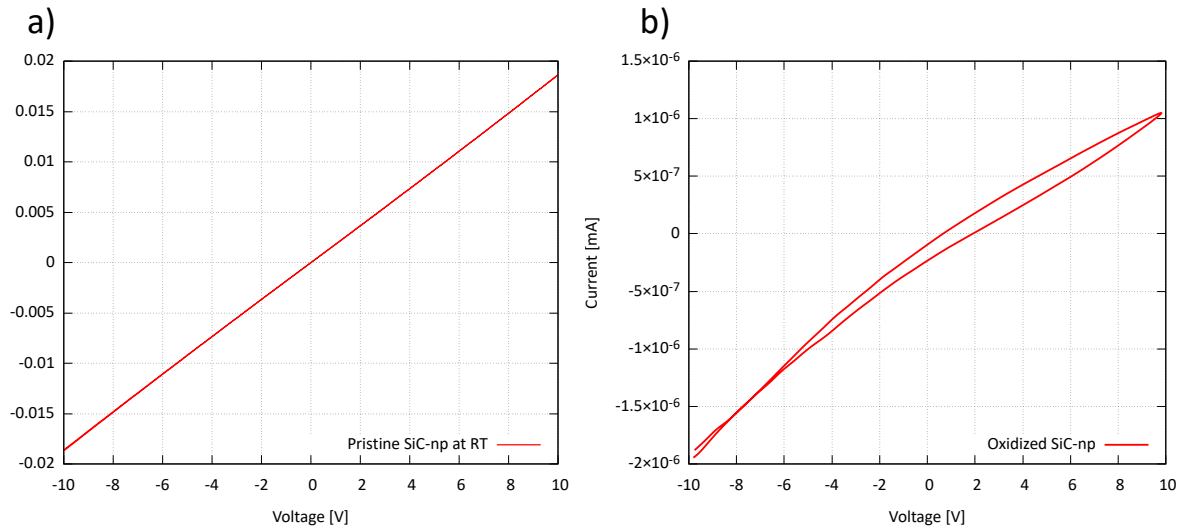


Figure 4.6: I-V characteristic on (a) pristine *SiC-nps* and (b) after the oxidation ramp reported in Figure 4.4. After the oxidation the shape and the average value of the curves are drastically changed.

direction of the following potential.
Figure 4.7 shows the I-T characteristic before and after the oxidation, at a potential of 1 and 5 V respectively.

The curve is represented in *Arrhenius* coordinates, in this way the equation $I \propto \exp\left\{\frac{-E_a}{k_B T}\right\}$ is linearized, where $E_a$ is the activation energy and $k$ is the Boltzmann constant. In the case of the non-oxidized film, the temperature range was limited to $[0, 300]$ °C, in order to avoid any reaction of the film with residual oxygen inside the measuring chamber.
The non-oxidized film (Figure 4.7a) reveals a weak dependence on temperature, with an estimated activation energy of $E_a = 0.08\ eV$. The oxidized device, reported in Figure 4.7b shows a strong dependence on the temperature, with an estimated activation energy that goes from $E_a = 0.41\ eV$ to $E_a = 0.85\ eV$ for low and high temperature, respectively. In both cases there is no significant hysteresis between sensor heating and cooling.
The electrical measurements in the case of the non-oxidized sensor has many analogies with a metallic behavior, which in the case of silicon carbide is obtained with a heavy doping. This is evidenced both by the linearity of the I-V characteristic and by the weak dependence of the current with respect to the temperature. In fact, in a heavily doped semiconductor, the charge carriers are due to ionized shallow levels already ionized at room temperature. In this way the temperature increase does not considerably influence the total number of carriers and therefore the current. On the other hand, the oxidized sensor presents an I-T characteristic similar to an intrinsic semiconductor, however the

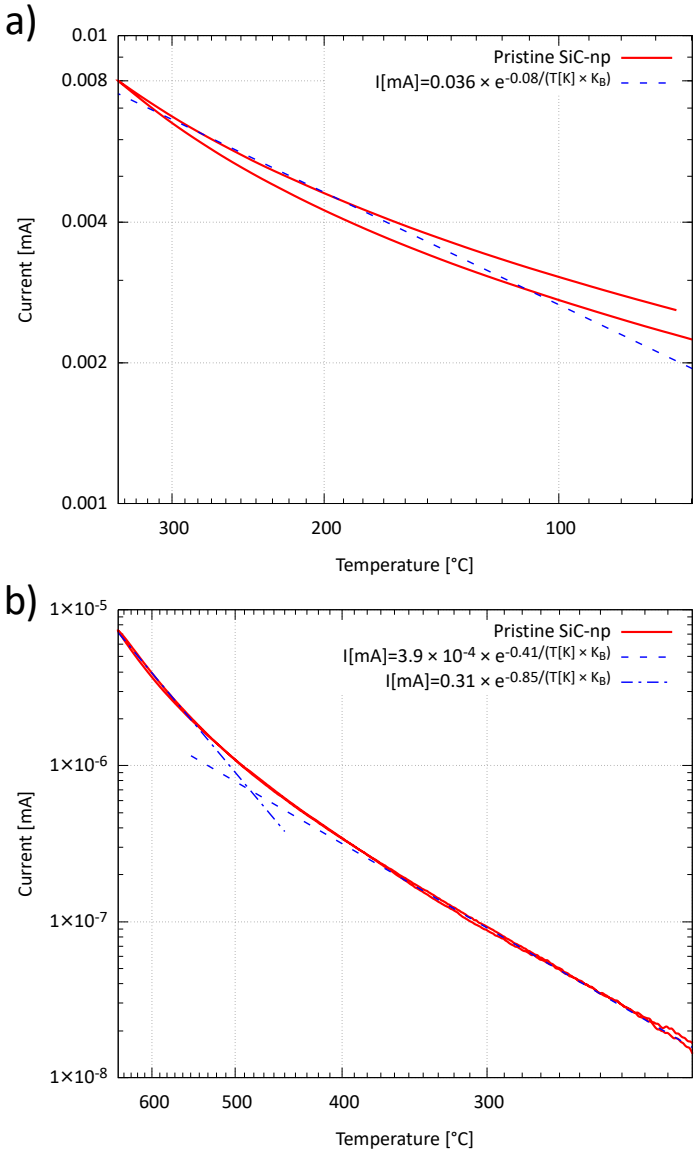


Figure 4.7: I-T characteristic on (a) the pristine $SiC$ nps and (b) after the oxidation ramp reported in Figure 4.4. After the oxidation the dependence of the current on the temperature is predominant, with and activation energy that goes from 0.08 $eV$ for the pristine $SiC$ to 0.85 $eV$ for the oxidized $SiC$.

I-V characteristic shows also some analogies with an electrolyte. In particular, the presence of a hysteresis in the I-V characteristic is generally attributable to reactions at the electrodes, suggesting that the electrical transport is for same extension of ionic nature.

### 4.3.4 Electrical response to $SO_2$ in a dry and wet environment

Figure 4.8 reports the EDX spectrum of the sensing film of the sensor after the further thermal process necessary to stabilize the electrical signal of the sensor. The spectra highlight the increase of the oxygen peak compared to the spectra of the unoxidized powder (dotted line).

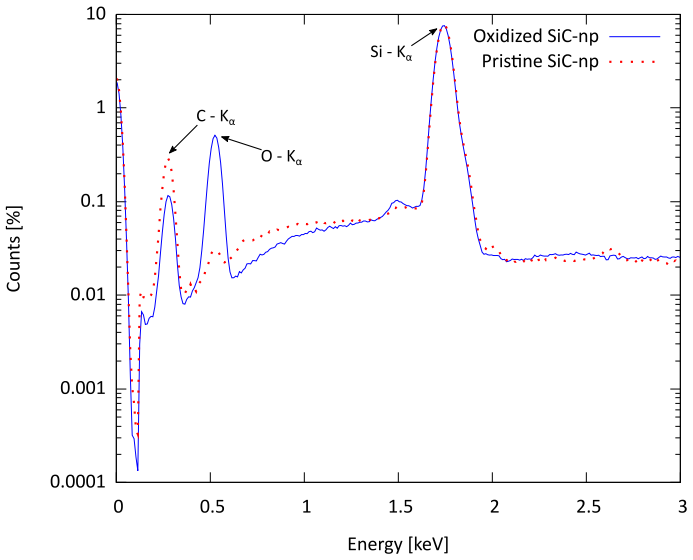


Figure 4.8: EDX spectrum of the pristine silicon carbide powder (dotted red line) and the oxidized particles (solid blue line). The silicon peak is approximately unchanged, while the oxygen peak is strongly visible only in the oxidized one.

Figure 4.9 shows the current through the sensor (a) and the relative response (b) during the inlet of $SO_2$ in dry and wet conditions (0% $RH$ and 8% $RH$).

Both in dry and wet conditions an increase in current through the oxidized $SiC$ film is observed in presence of $SO_2$, however, the response to the analyte in wet conditions is significantly greater that in the dry conditions. Comparing the current curves in Figure 4.9a, we observe that in the wet case the current is significantly larger than in the dry case. During the sensing measurements the DRIFT spectrum of the sensing film was acquired. Figure 4.10 shows the DRIFT spectra acquired in dry conditions (a), and in wet conditions (b), acquired during the intervals labelled in Figure 4.9b.

The reported adsorption spectra is calculated as described in paragraph 4.2.4, using the spectra acquired before the $SO_2$ inlet as background. From the spectra in dry conditions one can observe a slight modification in the portion of the spectrum corresponding to the $SiO - C$ $Si - OC$ bonds with the exposition to the analyte, however the high thermal noise does not allow to highlight any significant changes. In wet conditions, on the other hand, the formation of a peak clearly distinguishable from the thermal noise

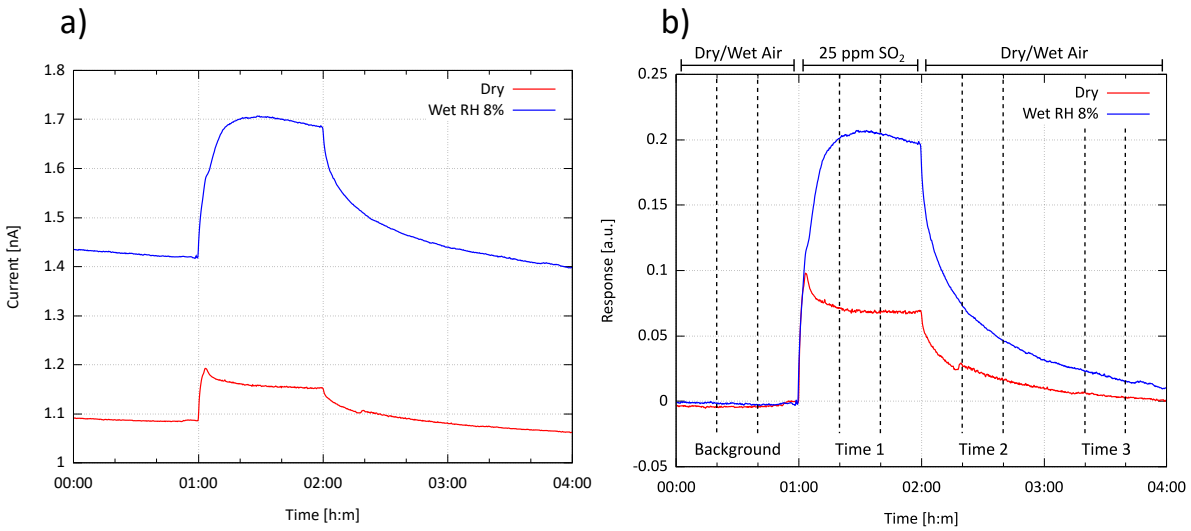


Figure 4.9: The current (a) and the response (b) through the oxidized SiC-nps-based sensor during the inlet of 25 *ppm* of $SO_2$ mixed with synthetic air. The red curve corresponds to the measurements in dry condition, while the blue curve corresponds to the measurements in wet condition ($RH\% = 8$ %). On Figure (b), the labelled intervals corresponds to the acquisition periods of the spectra reported in Figure 4.10. During the measurements the sensors is kept at a working temperature of 650 °C.

is observed. Comparing the spectra in wet condition in Figure 4.10 to the spectra measured during the oxidation of the silicon carbide nanoparticles (Figure 4.4), it is possible to associate the peak at 1250 $cm^{-1}$ to an increase of $Si - O$ bonds and therefore to an increase in the quantity of silicon oxide covering the sensing film of silicon carbide. Moreover, since the height of the absorption peaks is stable after the inlet of $SO_2$, it can be assumed that the $SO_2$ acts as an irreversible accelerator of the oxidation of the layer of SiC nps.

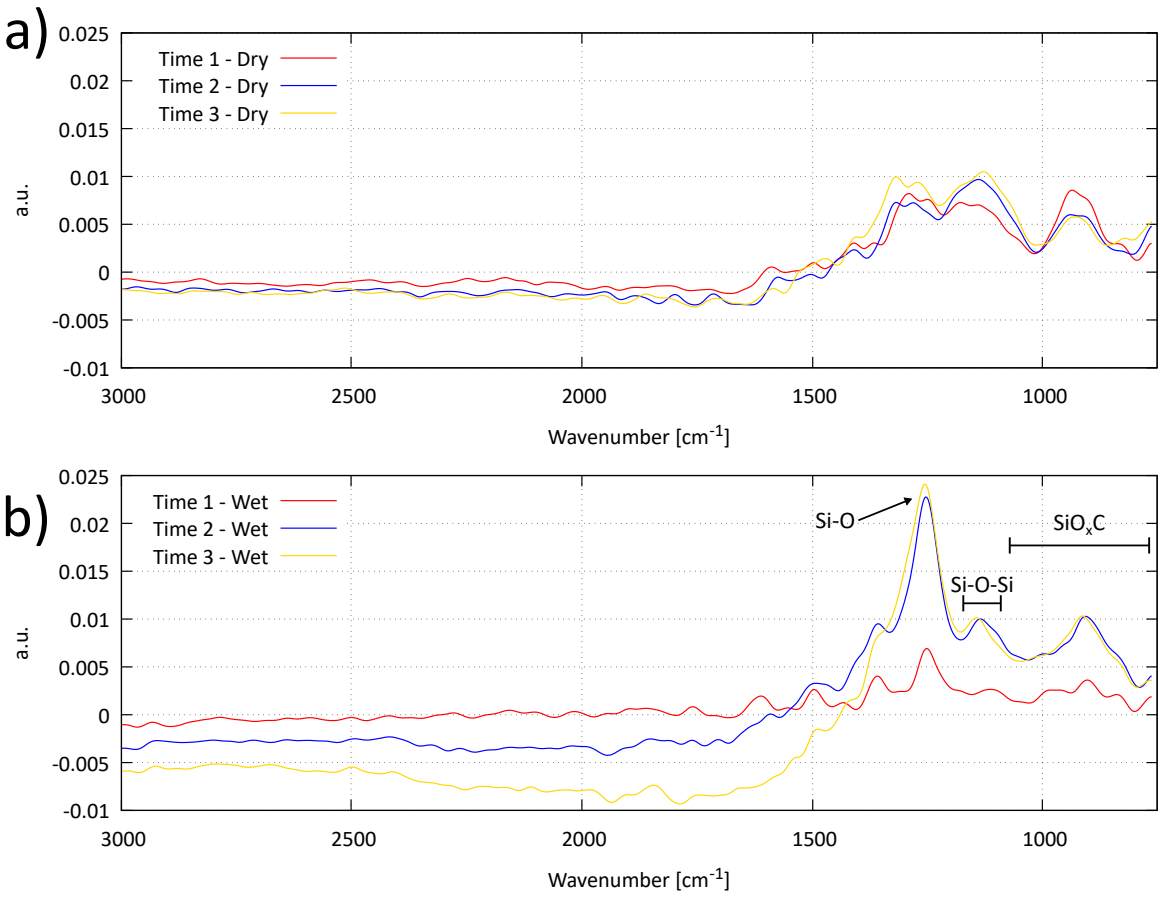


Figure 4.10: Spectra acquired during the inlet of $SO_2$ in dry (a) and wet (b conditions. In dry conditions the thermal noise hide any significant changes, while in wet condition the peaks corresponding to the oxidation of the sensing film are improved by the inlet of $SO_2$.

## 4.4 Proposed sensing mechanism

The reported measurements allow formulating some hypotheses about the working mechanism of $SiC$ as chemiresistive sensing material.
At first, the oxide formation has been demonstrated starting from 500 °C. Over this temperature, the formation of a thin layer of amorphous silica is inevitable. Then the conduction mechanism through the silica layer that covers the nanoparticles needs to be considered. Silicon dioxide is an excellent insulator and, even at high temperatures, shows negligible electrons mobility. However, since a non-zero current is measured through the oxidized silicon carbide, some charge carriers with non-zero mobility must be present to allow a current flow. These carriers are assumed to be ions bound on the surface, with a concentration that depends on the gas composition to which the sensor is exposed.
The hypothesis that the conduction can be of ionic nature is supported both by conductivity measurements made on porous silica [97, 98], and by the presence of a significant hysteresis in the I-V characteristic of the sensors, in analogy with the behavior of an electrolyte.
To distinguish the types of ions on the surface of the nanoparticles, one can consider the dry and wet environmental conditions separately in the presence and absence of sulfur dioxide.

### 4.4.1 Conduction in dry condition

Silicon atoms on the newly formed silica surface exhibit a series of incomplete bonds known as dangling bonds. These active sites have the tendency to passivate in the presence of oxygen, binding an oxygen atom every two silicon atoms. Since the $SiC$ nps are covered with a layer of silica, a similar structure is expected to be present on the surface in the absence of humidity. In this condition, at room temperature, there are no charge carriers. However, with the increase in temperature, the situation changes. Thermal agitation increases the probability that some oxygen atoms become ionized by capturing an electron from a silicon atom.
This situation is described in Figure 4.11, where the mechanism of formation of an oxygen anion on the silica surface is shown.

At high temperatures and in the presence of an electric field, a current is therefore established on the surface of the nanoparticles due to the diffusion of oxygen ions from one electrode to another. The addition of sulfur dioxide causes an increase in the current through the sensing film due to the interaction of the sulfur dioxide molecule with the surface of the silicon oxide. The interaction of sulfur dioxide is hypothesized to occur in conjunction with forming an oxygen ion on the surface of the oxide. According to this mechanism, the surface is partially passivated by sulfur dioxide, represented on the left in Figure 4.12.

The hypothesized structure of silicon oxide with sulfur dioxide is neutral and there-

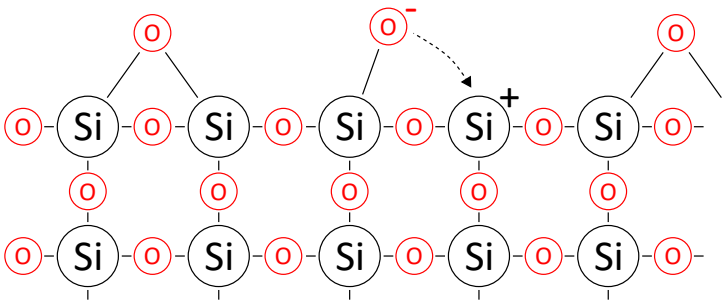


Figure 4.11: Ionization mechanism of the oxygen dry condition. The the silica surface forms an oxygen anion by trapping a positive charge.

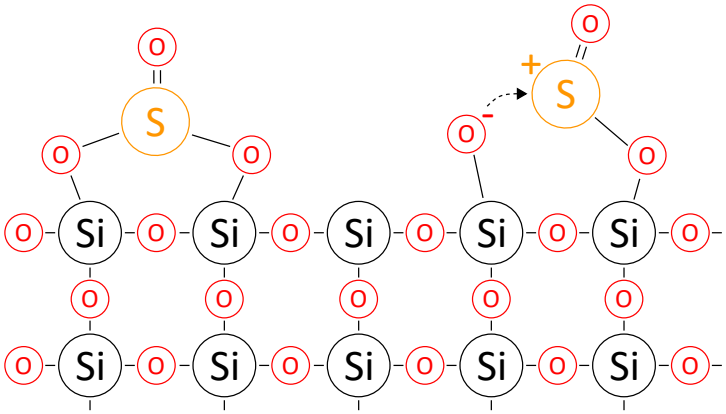


Figure 4.12: Proposed mechanism used by $SO_2$ to passivate the surface of silicon dioxide and the corresponding ionization mechanism.

fore does not contribute to charge transport. However it allows another mechanism of formation of an oxygen ion through the breaking of a sulfur-oxygen bond. The latter is less stable than the oxygen-silicon bond, and therefore, with increasing temperature, it is more likely to decompose. In conclusion, this mechanism increases the number of mobile charges by the ionization of the $SO_2$ molecules that passivate the surface, consequently increasing the conductivity of the sensing film.

### 4.4.2 Conduction in wet conditions

In the presence of humidity, the surface of silicon dioxide is mainly passivated by $OH$ groups [99]. In this configuration, with respect to the previous dry case, the electrical conduction occurs according to an additional mechanism. In fact, the $OH$ groups tend to partially dissociate, allowing the conduction through proton hopping on adjacent $OH$ groups. This mechanism, first described by Grotthuss [100] to explain the electrical conductivity of deionized water, is generally promoted over diffusion transport, explaining

the higher current measured in the presence of humidity with respect to the dry case.

The Figure 4.13 represents the predominant conduction mechanism that is hypothesized to occur on the surface of the oxidized silicon carbide in a wet environment.

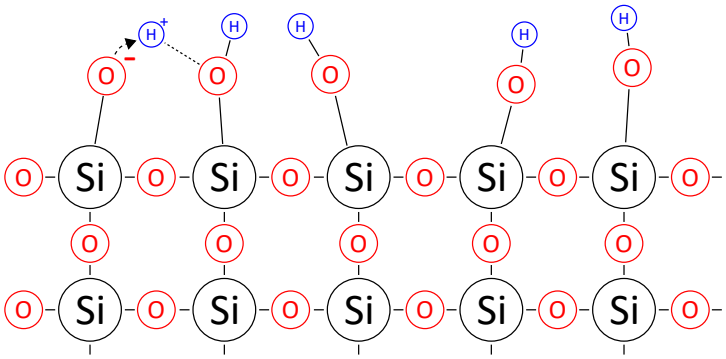

Figure 4.13: In wet conditions, the conduction mechanism is supposed to be related to the proton hopping between adjacent $OH$ groups.

The addition of sulfur dioxide under the same conditions, even in a wet environment, manifests itself experimentally with an increase in the conductivity of the sensing film. The surface of the silica is supposed to interact with the sulfur dioxide in a similar way to the dry case, except that in this case, one of the $SO_2$ oxygens forms an $OH$ bond. This structure, shown on the left in Figure 4.14, can undergo deprotonation.

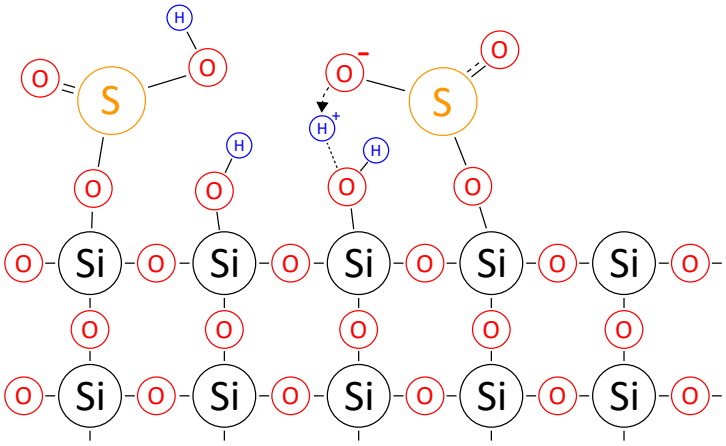

Figure 4.14: Interaction between $SO_2$ and the silicon dioxide in wet conditions. The decomposition of the $OH$ groups on sulfur contributes to the total number of charge carriers.

In this case, the decomposition of the $OH$ group attached to sulfur is favored with respect to the dissociation of the $OH$ groups normally present on the surface in a wet

environment since the remaining negative charge is shared between the two bonded oxygen atoms. This mechanism causes the sulfur dioxide to lead to an increase in the number of charge carriers, which is measured as an increase in the current through the sensing film.

## 4.5 Conclusions

In this work, the oxidation *in situ* at different temperatures of silicon carbide in the form of nanoparticles was studied using DRIFT infrared spectroscopy. The formation of a silicon oxide layer has been demonstrated in air above 500 °C, both through the formation of absorption peaks corresponding to the oxidation products of silicon carbide ($SiO_2$ and $CO_2$), and through the *ex-situ* EDX measurement of the sensing film, before and after the oxidation process.
From the gas sensing measurements on oxidized sensors, the possible use of silicon carbide as a functional material for the manufacture of chemiresistive gas sensors for the detection of $SO_2$, both in dry and in a wet environment ($RH$ 8 %), has been demonstrated. From the *operando* DRIFT measurements, it emerged that exposure to $SO_2$ improves the sensing film's oxidation in a wet environment, which can be evaluated by the increased peaks intensities corresponding to the bonds silicon-oxygen.
From an electrical and thermo-electrical point of view, through I-V and I-T characteristics, the sensing material showed a drastic change in conductivity during the oxidation processes, transitioning from a metallic behavior to a semi-insulating behavior.
From the formation of hysteresis in I-V characteristic as a function of the direction of the applied potential, and in analogy with the conduction mechanism of porous silica, it is hypothesized that the electrical conduction mechanism on oxidized powders is mainly ionic due to the adsorbed species which, at high temperatures, tend to partially ionize. A sensing mechanism of $SO_2$ detection has been proposed in dry and wet conditions. The variation in conductivity is associated with the different ionization energies belongings to different species that passivate the oxide layer over silicon carbide nanoparticles.
In summary, the primary considerations of this work are:

- Under operating conditions (650 °C in air), oxidation is inevitable on a SiC-nps-based sensor.
- The conductivity of the sensing film drops drastically once it is oxidized, passing from a metallic regime to a semi-insulating regime.
- A mechanism to explain the conduction on oxidized SiC powders has been proposed, assuming it is of ionic nature.

The proposed sensing mechanism approximates the sensing layer on the oxidized SiC as composed entirely of silicon oxide. In the same conditions of a sensor manufactured using silica nanoparticles obtained by direct synthesis, a further study should investigate the response. In this way, the role of silicon carbide would be definitively clarified in $SO_2$ detection.

# Conclusions and future developments

The systematic gap in the study of chemiresistive gas sensors is due both to the complexity in modeling the gas-solid interaction and to the lack of techniques and instrumentation suitable for a methodic study of the gas sensing mechanisms. In a chemiresistive gas sensor, these are generally linked to a modification of the surface chemistry of the sensing film, involving both the adsorption of gaseous species and the catalysis of chemical reactions on the surface. To investigate these phenomena, it is necessary to employ instrumentation that directly evaluates the surface chemical changes induced by the interaction of a gas with a sensing material by controlling the working conditions. To study the surface kinetics,the development of a DRIFT setup to characterize a chemiresistive gas sensor *in operando* was presented. The system has been designed to fit *Bruker* FTIR *Vertex V70*, equipped with the *Praying Mantis* DRIFT accessory from *Harrik Scientific*.
In the previous chapters, the overall system and the development of each module have been presented describing, in particular, the mechanics, electronics, and software developed for the setup. The system's mechanics consists of a sealed chamber in stainless steel in which the sensor under test is housed. The chamber is equipped with a 3-axis positioning system, which allows accurate positioning of the sensors with respect to the infrared light beam. A fluid dynamics study of the chamber is presented in different thermodynamic conditions, demonstrating that a laminar flow well describes the gas flow on the sensor.
The electronics were designed to monitor the current through the sensing film within a wide range ($\pm 10^{-10} - 10^{-3}\ A$), allowing at the same time to set the measurement parameters, including the applied potential ($\pm 10\ V$), the working temperature ($RT - 900$ °C), the composition of the atmosphere and the intensity of light on the sensing film (see appendix B). The software, which consists of a firmware and a user interface, allows both the control of the low-level functions (auto range of the acquisition electronics and the monitor of all raw quantities) and the automation of more complex measurements. In particular, the procedures for acquiring the I-V and I-T characteristics have been described, which allow extracting some properties related to the electrical transport of the sensing film that composes a gas sensor, such as the activation energy and the non-

linearity factor in a power law approximation.
To validate the operation of the electronics and the control software, it was presented a study on chemiresistive gas sensors based on tin oxide for the measurement of carbon monoxide in different thermodynamic conditions. The system as a whole, on the other hand, was validated by investigating the changes induced on the surface chemistry during the exposure to gaseous hydrogen.
Therefore, it has been demonstrated that the system as a whole is simultaneously capable of:

- acquiring the electrical characterization of a chemiresistive gas sensor by setting the thermodynamic operating conditions (e.g., working temperature and composition of the atmosphere),
- measuring a change in the surface chemistry, through the acquisition of the DRIFT spectrum.

In this way, the versatility in understanding the fundamental sensing mechanisms was emphasize, in particular, device's performance could be improved by following a rational approach, instead of a mere empirical strategies.
Exploiting the potential of the presented system, it is reported a study on the sensing and conduction mechanism of a sensor based on silicon carbide nanoparticles, used for the selective detection of $SO_2$ in the *ppm* range, diluted in air.
This study has demonstrated a further application of the setup, which involves investigation on *in situ* thermoactivated chemical reactions. In particular, the oxidation reaction of silicon carbide through the *in situ* monitoring of the infrared absorption peaks at increasing temperatures has been reported, highlighting the formation of a layer of silica covering the nanoparticles of silicon carbide. Finally, from the analysis of the electrical and thermoelectric characteristics on oxidized $SiC - nps$ films, it was possible to make some hypotheses regarding the conduction and sensing mechanism of sensors based on oxidized $SiC$, suggesting a mainly ionic electric conduction.
The presented system can synchronize an electrical with a spectroscopic characterization, and at the current stage of development, it already allows to correlate information from two different fields to obtain experimental confirmations on the sensing models hypothesized on diverse materials. However, many improvements are being implemented, dedicated to extending the potential of the setup. These improvements can be divided into three distinct areas:

- Instrumental, which allow to advance the quality of the acquired measure.
- Data analysis, in particular the elaboration of DRIFT spectra.
- Extensions to the system, which add new features to the setup.

On an instrumental level, a series of improvements can be made both on the FTIR setup and on the electrical characterization setup. From the point of view of spectroscopic measurements, the upgrades are dedicated to optimizing the acquired signal, which can be done either by increasing the brightness of the light source or by improving the sensitivity of the detector used. In particular, as described in paragraph 3.7.2, it has been shown that the efficiency of the MCT detector can be improved via hardware considering the infrared emission of a chemiresistive gas sensor *in operando*, which is kept at a high temperature (up to 650 °C) contributes to the deterioration of the quality of the acquired signal.
Regarding the electrical characterization system, a future improvement could focused on the addition of some reference gas sensors on the exhaust of the measurement chamber, including a $CO_2$ sensor and an oxygen sensor, to collect a feedback, although qualitative, on the outgoing gases or identify any reactions catalyzed by the sensor during use.
Regarding the processing of the DRIFT spectra, an upgrade under development concerns the creation of software that analyzes and represents the absorption spectra' temporal evolution to identify how and which features of a spectrum change during operation.
In addition to the improvements mentioned above, some extensions are currently under development to increase the possible applications of the presented system. Among these, the construction of two accessories is reported in the appendix (B).
The first one concerns the development of a heated sample holder with the same form factor of a TO-39, to be used to directly characterize the powders in temperature without requiring to manufacture a gas sensor.
The second accessory concerns the creation of a setup to add the possibility of illuminating (e.g., with ultraviolet light) a sample during *operando* DRIFT measurements, adding the option of photoactivating a sensor during the measurements (see appendix B).

In conclusion, the presented system allows to electrically characterize a sensor at different thermodynamic conditions, simultaneously studying its surface chemistry through the acquisition of the infrared absorption spectrum. In the field of gas sensors, the *operando* approach is still under development, and the scientific community is becoming aware of the possibilities of this type of instrumentation. By developing a systematic protocol for the analysis of the gas/solid interaction, we believe that this system can contribute to a more exhaustive understanding of the sensing mechanisms involved in different of chemiresistive gas sensors.

# Appendices

# Appendix A

# 3D printing

The mechanical design of the chamber used for *operando* DRIFT measurements described in the chapter 3, had a series of design limits imposed by the geometries of the components to which it had to fit, such as the sample chamber of the *FTIR vertex V70* (*Brucker*) and the optics of the DRIFT *Praying Mantis* accessory.
Since the computer-aided design (CAD) digital models of these components were not available for a precise digital design, the development of the system mechanics was done through the iterative construction of prototypes produced by 3D printing.
In this context 3D printing, it has made it possible to speed up and simplify the development of the system. In fact, despite the system being made of stainless steel, the accuracy of the geometries has been verified on plastic 3D printed parts to reduce the possibility of errors on the final parts.
Two printing technologies were used for this project: Fused deposition modeling (FDM)[101], and Stereolithography 3D printing (SLA)[102]. These two technologies complement the other, as the first allows to create three-dimensional objects very quickly and at a low cost but with a poor quality finish, while the second allows to create the same with a much higher level of finish but at a higher cost and generally taking longer.
In the following sections, these two printing techniques will be briefly introduced. Finally, the possibility of using printed parts not only as a geometric verification tool but also as a technology for functional prototyping of custom experimental setups will be briefly discussed, which motivated the setting up of a 3D printing laboratory at the CNR-IMM of Bologna.

## A.1 Fused deposition modeling: filament 3D printer

Fused deposition modeling (FDM) indicates the 3D printing technology on which all filament printers are based, which uses consecutive layers of fused plastic to fabricate a tridimensional object [103]. Conceptually, the operating principle of a filament FDM

printer is quite simple and summarized in the Figure A.1:

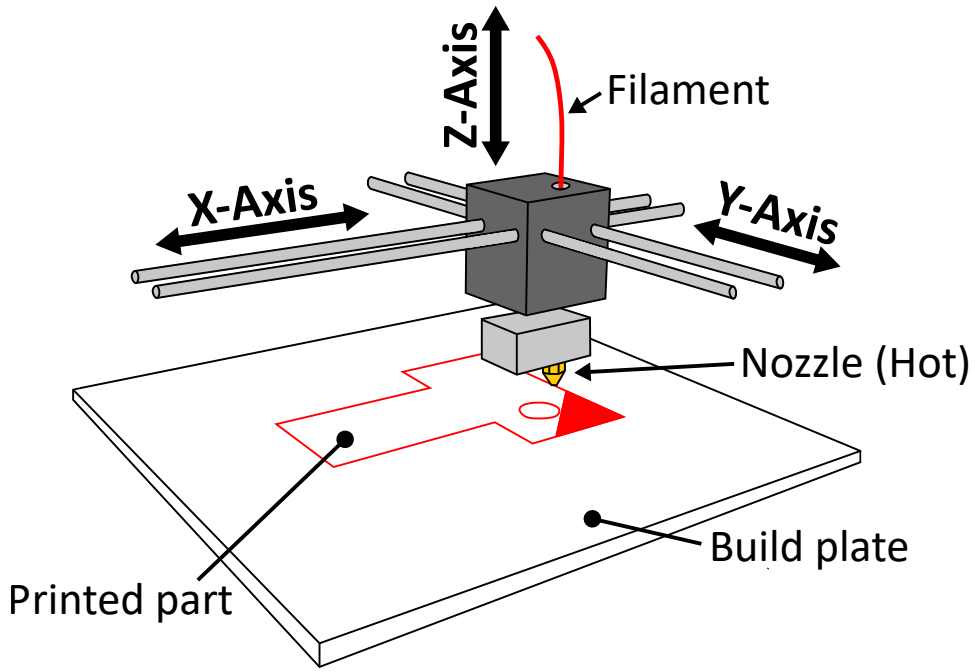


Figure A.1: Operation diagram of an FDM printer. A filament made of a thermoplastic polymer is pushed through a nozzle, which creates a three-dimensional object layer by layer.

In an FDM printer, a plastic filament is fused and pushed through a nozzle, which locally deposits the material that will compose an object layer by layer, exploiting a numerically controlled three-axes system (Figure A.1). Compared to the pellets used in the first printers, using a filament allows reducing the number of mechanical components involved. In fact, in a filament printer, the pressure inside the extruder, which allows the controlled release of the molten material, is given by the filament itself. Indeed, inside the extruder, the thermal gradient causes the solid part of the wire (cold) to push the viscous part (hot), and in this way the use of complicated linear extruders to control the material deposition is avoided.
The size of the nozzle and the type of material processed defines the maximum resolution obtainable by a filament printer ranging from 0.5 to 0.1 $mm$. However, it is important to underline that the piece's geometry is ultimately a crucial parameter to define the maximum resolution obtainable compared to other printing techniques.
FDM printers allow for the processing of almost all thermoplastic polymers in a fast and economical way, and this has determined their success in the field of rapid prototyping. Indeed, depending on the applications, there are materials with different functional properties, such as mechanical, thermal, or chemical resistance.

For the manufacture of the parts developed in this work, we used polymers that allow obtaining the maximum dimensional accuracy at the expense of functional properties (e.g., Polylactic acid (PLA) and polyethylene terephthalate glycol-modified (PETG)). However, to update and expand the systems developed without involving traditional processing techniques, more exotic materials such as PPS (Polyphenylene sulfide) and PEEK (Polyether ether ketone) were tested, which offer performance comparable to metal machined parts.

## A.2 Stereolithography (SLA): resin 3D printer

In a stereolithographic printer (SLA), the punctual deposition of the material is made using an ultraviolet laser beam that locally photopolymerizes (hardens) a liquid resin [102].
The operating principle of an SLA printer is summarized in Figure A.2:

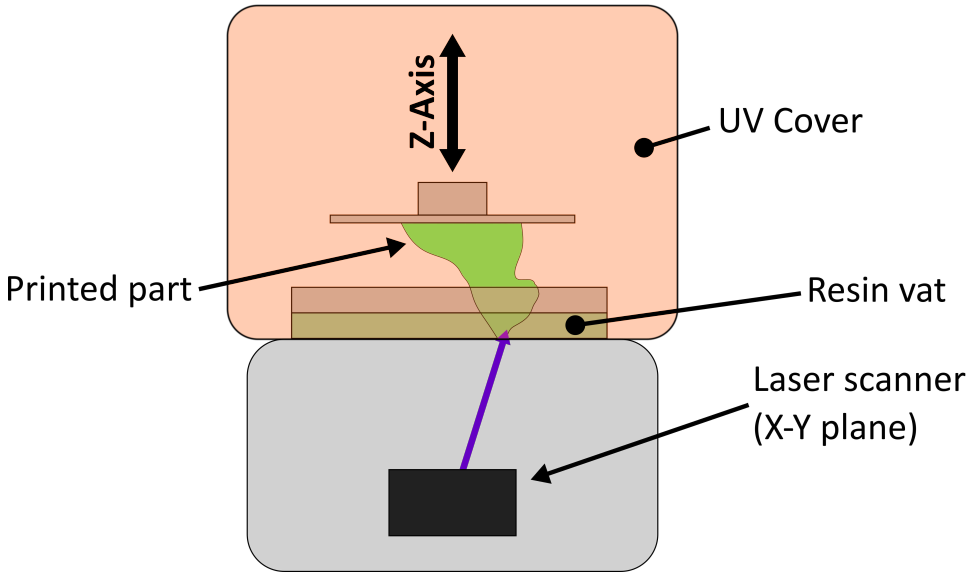


Figure A.2: Operation diagram of an SLA printer. A photo-curing resin is precisely hardened by an ultraviolet laser which is scanned to form a three-dimensional object, layer by layer.

Unlike FDM technology, where the nozzle is physically positioned where the polymer is deposited, in an SLA printer a laser beam hardens the single layer of material. In this way, it is not necessary to physically move the laser, but the scanning is done by exploiting a system of optical galvanometers, allowing a very fast scanning speed of the entire printing area. However, as the single layer is usually very thin ($\sim$ 50 $\mu m$) compared to an FDM printer, the printing process is globally slower.

We also note that objects are printed upside down on the build plate. In this way the amount of resin needed to make a part does not depend on the object's size since the resin vat is filled with a constant quantity of liquid resin.
A part printed in resin, compared to a piece printed in filament, is not directly usable but requires a series of post-processing. In particular, it is necessary to remove the residues of uncured resin using an isopropyl bath and finish the hardening process through ultraviolet curing and/or high-temperature annealing ($\sim 160 - 200$ °C for two hours).
A resin-printed part generally has a resolution of less than 0.1 $mm$, which gives it a smooth finish. Also, compared to FDM printing, geometry does not significantly affect the final quality of a part. However, depending on the type of material processed, the final accuracy is generally lower than the maximum achievable resolution, and it is about a tenth of a millimeter.
The materials available for this type of technology, although more limited than the FDM technology, cover a wide range of mechanical, thermal, and chemical properties that allow the realization of functional parts.

## A.3 Conclusion

3D printing technologies have become a fundamental tool for rapid prototyping of custom experimental setups. Furthermore, the availability of functional materials for both filament printers and resin printers makes it possible to replace in many circumstances the need to use traditional processing techniques for the production of mechanical parts. As part of the realization of the DRIFT setup for measurements on *operando* chemiresistive gas sensors, 3D printing has made it possible to iterative and rapid development of all the necessary mechanical parts to avoid design errors on the final metal parts.

# Appendix B

# In operando DRIFT setup extensions

The DRIFT system described in chapter 3 allows to correlate the electrical and thermal behavior of a chemiresistive gas sensor with its infrared absorption spectrum.
However, there are situations in which a change in the infrared spectrum is observed also with respect to stimuli other than temperature or exposure to a specific working atmosphere. Indeed, in the field of chemiresistive sensors it is known that some materials, if exposed to specific radiation (e.g., UV light), show an improvement in gas sensing performance, caused by a modification of the surface reactivity of the sensing film [104, 11].
These variations can be related to surface adsorption or desorption and therefore, when present, they can be qualitatively measured through DRIFT spectroscopy.
One goal is therefore to observe photo-assisted surface reactions on the sensing film of a gas sensor, simultaneously acquiring both the electrical response and the DRIFT spectrum.
Another goal is the possibility of expanding the field of use of the system to samples that are not strictly chemiresistive gas sensors mounted on TO-39 package. Indeed, as described in chapter 3, the gas sensor itself is implicitly part of the setup. The heating of the sensing material is done by exploiting the substrate itself, which, being very small in size, does not require special trick for heat dissipation. However, the preparation of a gas sensor is a dispensable procedure and there are situations in which it is not possible or not necessary to manufacture a sensor, such as for the study of heat-activated reactions or in the case of a quick characterization of a powder. Therefore it would be advisable to have a heating system independent from the fabrication of a gas sensor. Furthermore, the characterizable area of a gas sensor is rather limited ($\sim 2x2\ mm$) limiting the maximum usable intensity of the source.
In this section it is described the design of two accessories, designed to be compatible with the setup described in chapter 3.

1. Setup for carrying out DRIFT measurements on photoactivated *operando* gas sensors.

2. Accessory for carrying out DRIFT measurements on powders in temperature.

The two accessories have been developed to be compatible with each other and therefore can be used simultaneously.

## B.1 Setup for *operando* photoactivated measurements

The ability to catalyze photoassisted chemical reactions has been observed in different fields. In the field of chemical gas sensors it is known that some materials (e.g., $ZnO$) show an improvement in gas sensing performance if photoactivated at specific wavelengths [104, 11].
These materials can generally be used both in thermo-activation and in photo-activation, however, depending on the mode of use, a different behavior can be observed. If the properties of a photoactivated sensor are due to adsorption, or the desorption of surface species, then it is possible to qualitatively measure the changes through DRIFT spectroscopy.
These considerations motivated the design of an accessory that allows to illuminate the sensible film of a gas sensor by simultaneously carrying out the measurements described in chapter 3.
The accessory is divided into three parts:

- An external light source (e.g., a diode).
- An hardware/software interface that controls the intensity of the light source.
- A mechanical/optical support that direct the light on the surface of the sensor.

In Figure B.1 is schematically represented the *operando* DRIFT setup interfaced with the accessory to make measurements in photo-activation.

Currently a near ultraviolet LED (395 $nm$) is used, coupled to a high vacuum optical fiber of 100 $\mu m$ in diameter, however both the fiber and the other optical components have been chosen to be usable in a wide range of wavelengths.

### B.1.1 Mechanical design

The light inside the measurement chamber is carried using an optical fiber, coupled directly to a power LED, placed outside the measurement chamber of the FTIR setup.

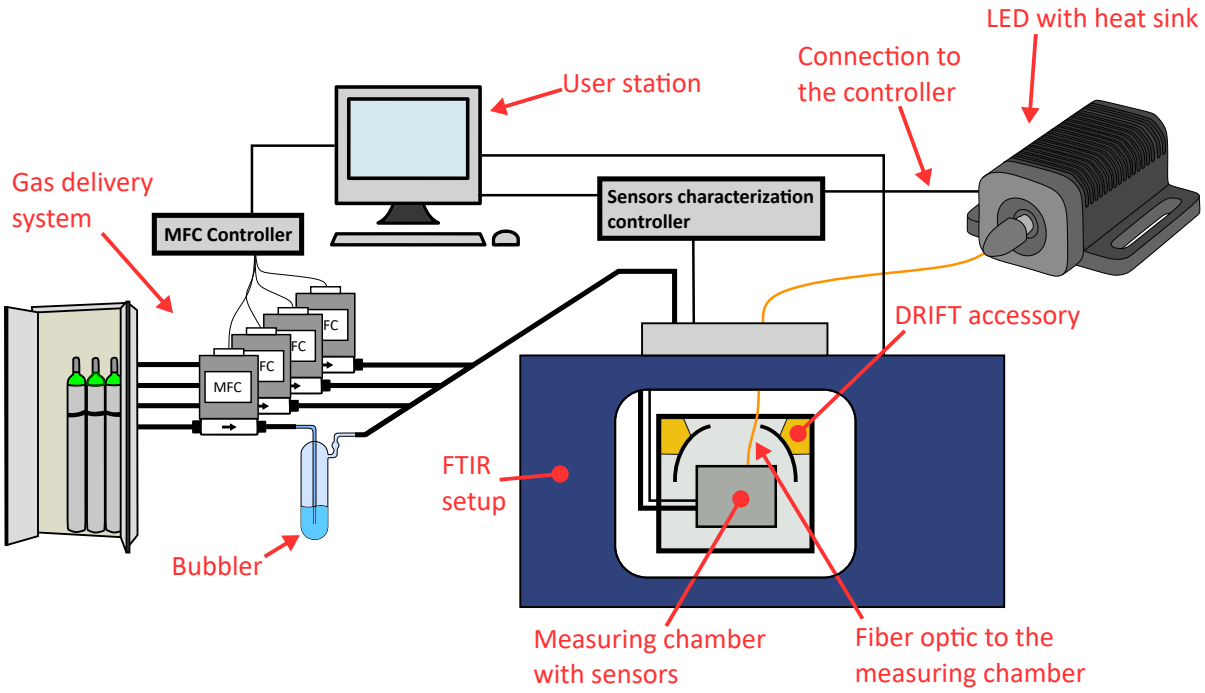


Figure B.1: The figure shows the entire DRIFT setup described in chapter 3 integrated with the accessory to make measurements in photactivation. The wavelength of the activation light is set by the type of LED used, placed outside the measurement chamber of the FTIR and controlled by software. The LED is directly coupled with a vacuum fiber optic that takes the light inside the chamber.

The fiber is brought inside the chamber using a special vacuum connector and is positioned so as to center the light on the sensing film of the gas sensor under test. To avoid modifying the measurement chamber, the light is brought inside the dome through the fused quartz window used for the visual positioning of the sensor.
From the mechanical point of view, the problem is summarized in designing a support capable of positioning the optical fiber correctly, respecting the constraints imposed by others elements inside the FTIR measurement chamber and maximizing the light on the surface of the gas sensor. The setup has been developed so that it can be easily applied and removed without compromising the use of the chamber without accessories.
The figure B.1 shows the section and the exploded view of the measurement chamber with the photo-activation accessory mounted.

The fiber support has been 3D printed in resin (see appendix A) and is positioned to align the fiber with the center of the sensor. The whole is fixed with two screws, of which the longer one replaces one of the locking knobs in the figure 3.4.
The light is not focused or collimated on the sensor surface at the exit from the fiber, both to limit the total volume of the accessory and to avoid the addition of a beam

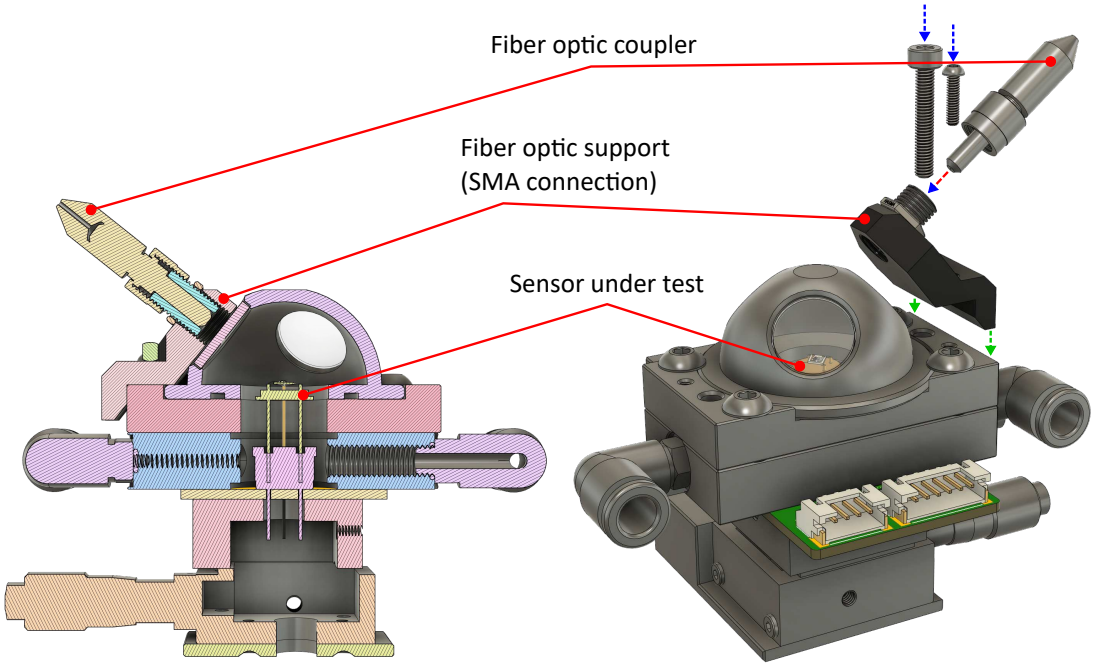


Figure B.2: The figure shows the section of the measuring chamber with the mounted accessory (left) and the project exploded (right). The support is 3D printed in standard resin using SLA technology.

positioning system.

### B.1.2 Control system

The accessory for photo-activation measurements is interfaced using the same software and hardware described in the 3.6.3 section, in this way the management of the acquisition parameters (e.g., voltage on sensing film, temperatures, etc.) and the control of the intensity of the light is done through a single interface. The intensity of the light is modulated via hardware using a transimpedance amplifier that sets the current through a LED collimated to an optical fiber, in this way a fine control is obtained on the emitted power being the potential drop on the LED roughly constant.
From a software point of view, the light emitted can be controlled both manually or using automatic acquisition procedures (*routine*, see section 3.6.3), which correlate the current through the sensing film with the intensity of the light provided. The calibration between the current supplied to the LED and the specific intensity on a sensor is done using a photodiode mounted on a TO-39 package.

## B.2 Heater design for DRIFT measurements on heated powders

An inherent limitation of the DRIFT setup for measurements on *operando* chemiresistive gas sensors is the need to use a gas sensor as a sample. The setup structure is indeed designed to use a specific package (TO-39). Furthermore, the substrate of a sensor beahves as a part of the system itself, allowing the temperature control using the integrated platinum heater.
However the preparation of a gas sensor is an expensive procedure and in some cases it is either not necessary or impossibile to be used, therefore, in order to expand the veratility of the system a different solution is needed. For this reason a heated sample holder has been designed with the same form factor as a gas sensor mounted on TO-39 package.
Conceptually, the system is a micro hotplate, 11 $mm$ in diameter and 6 $mm$ in thickness that allows to heat a sample of powders up to a maximum temperature of 350 °C.
From a software point of view, the temperature control is done using the same interface (hardware and software) used by the gas sensor control system.

### B.2.1 Mechanical design

The main design limitation of this accessory is the size, having to replicate the structure of a chemiresisitive gas sensor mounted on TO-39 as closely as possible.

The figure B.3 shows the section and the explosion view of the accessory, which is divided into four main parts:

- a removable crucible, in which is physically housed the powder/sample to be characterized,
- a metal support, placed in contact through a thermal bridge (thermoconductive paste) with a ceramic heater,
- a ceramic heater, which for convenience is a substrate of a sensor, of which the platinum serpentine is exploited,
- a modified TO-39, with a side pocket that allows the assembly of the whole accessory.

All parts of the system (apart from the heater) are made of stainless steel, CNC machined and the part in contact with the powders has been designed so that it is removable. In this way it can be easily cleaned without risking damaging the rest of the accessory or cross contaminate subsequent samples.
In addition to the crucible (part 1), sample holders with different geometries have been

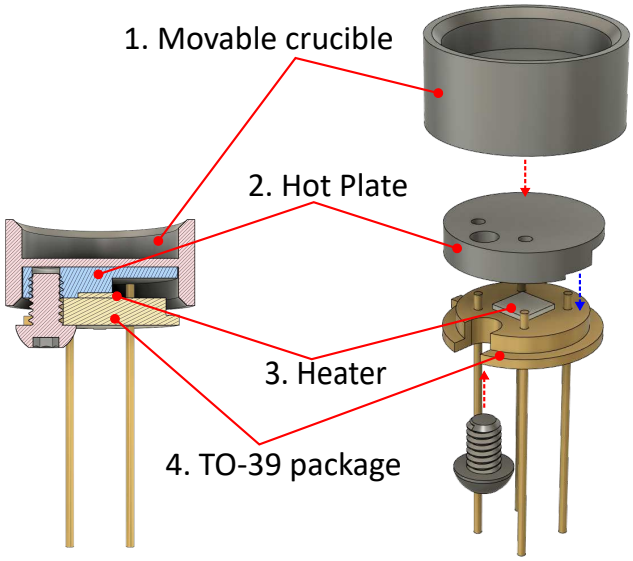


Figure B.3: The figure shows the structure of the micro hotplate in section (left) and the exploded view of the project (right). The dimensions are based on a TO-39 package. The ceramic heater used (3) is a substrate of a sensor, of which the platinum heater is exploited.

designed, which allow to mount different types of samples, such as films deposited on silicon wafers.

## B.3 Conclusion

In this appendix two accessories have been presented that allow to expand the capabilities of the system described in chapter 3. In particular, the possibility of performing DRIFT measurements on *operando* chemiresisitive gas sensors photoactivated has been added and the applications of the entire setup have been extended on samples not necessarily in the form of gas sensors.
These two accessories, despite their semplicity, increase the types of experiments that can be carried out with the DRIFT setup presented, demonstrating at the same time its versatility and expandability towards different research fields.

# Appendix C

# Mechanical drawings

In this appendix are reported the drawings of the mechanical parts designed for the realization of the measuring chamber described in chapter 3 and the mini hot-plate described in appendix B.

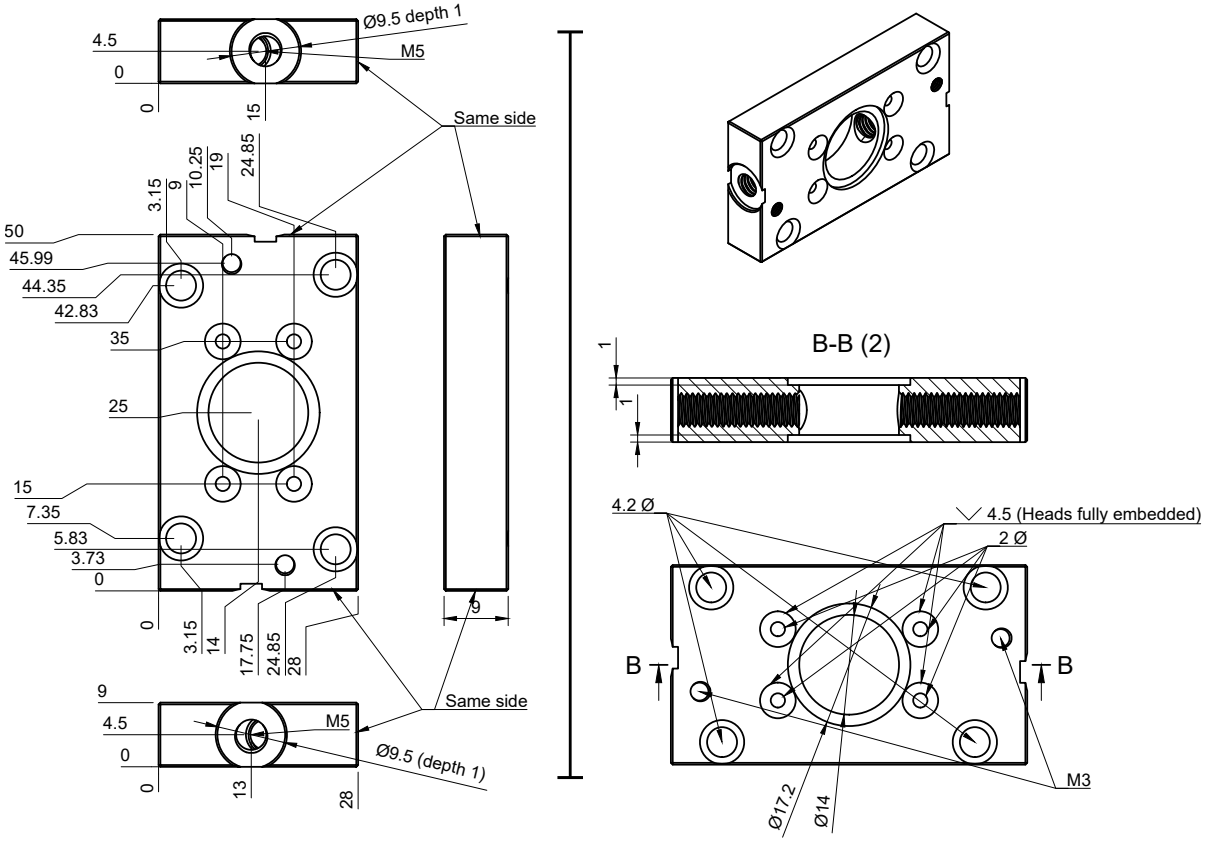


Figure C.1: Adapter for the dome.

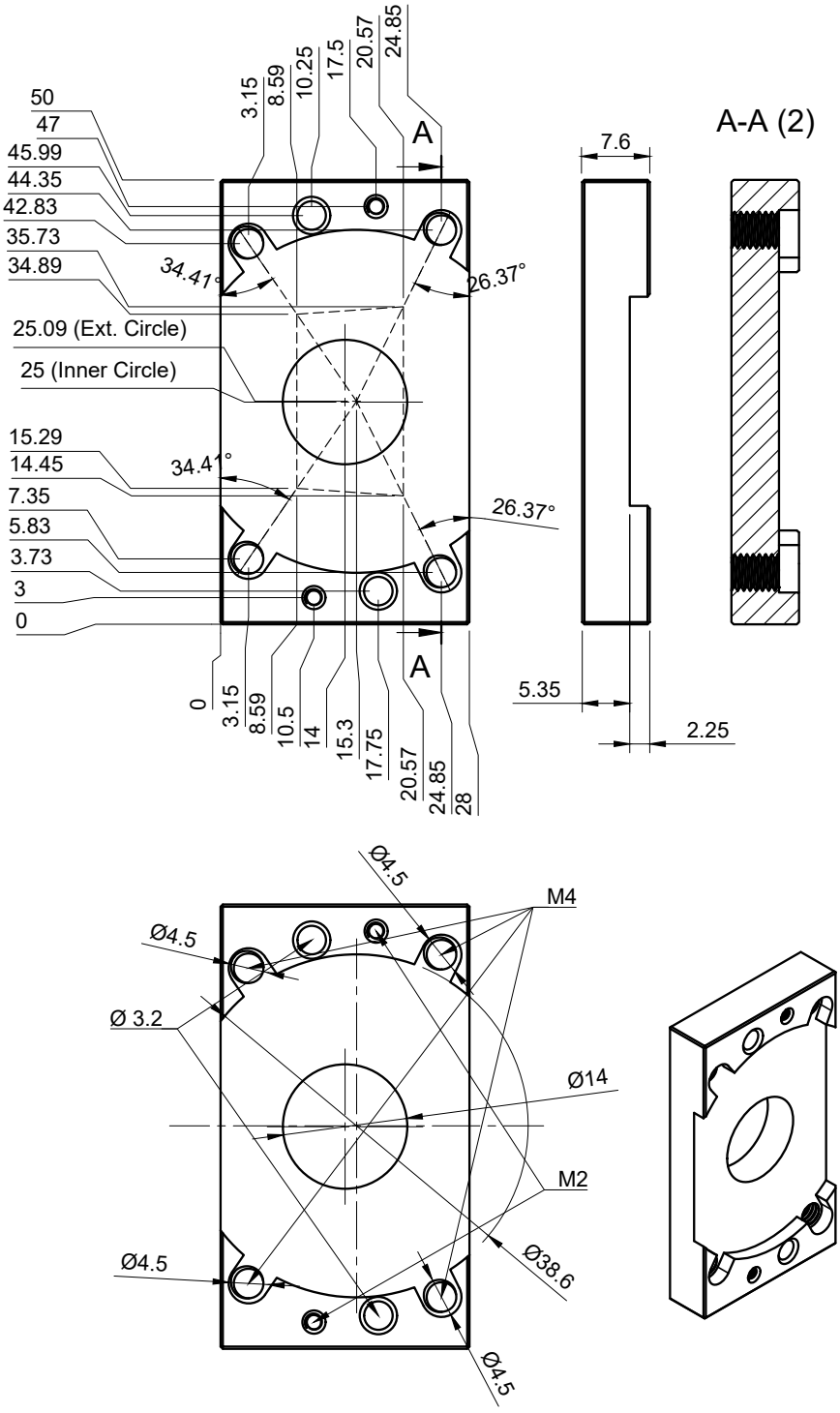


Figure C.2: Body chamber.

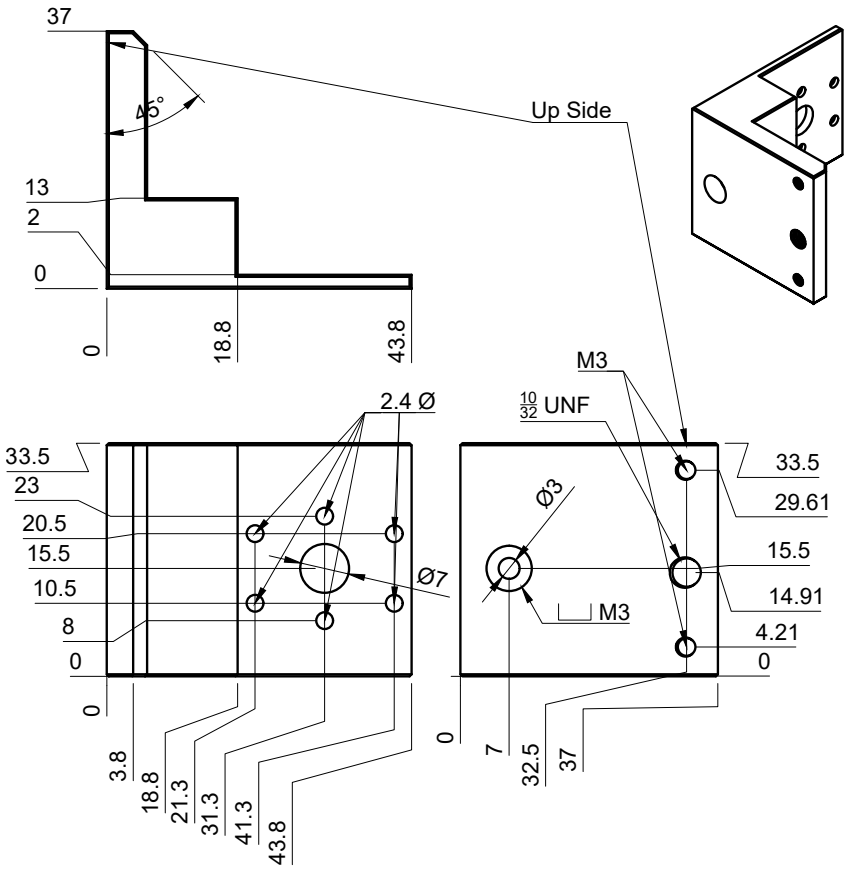


Figure C.3: Bracket to DRIFT Z-axis.

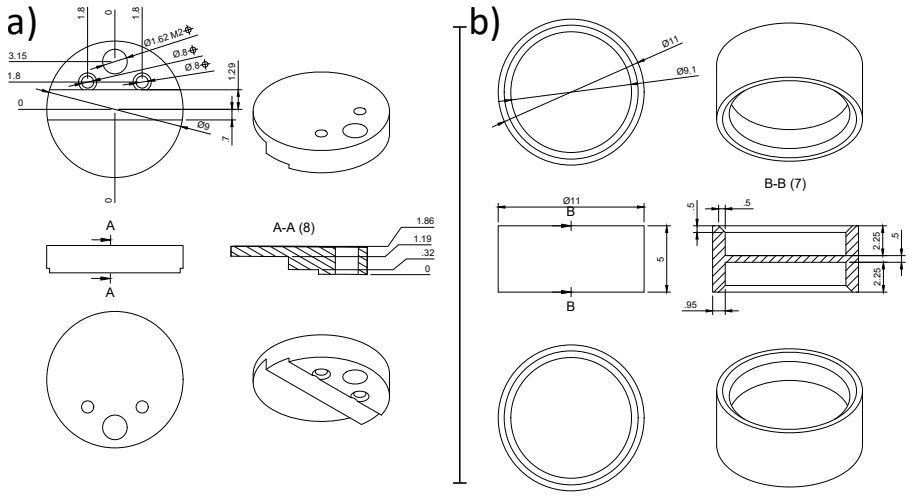


Figure C.4: (a) Mini-hot plate for DRIFT measurements and (b) removable powders holder.

# Bibliography


[1] R. Binions and A.J.T. Naik. 13 - metal oxide semiconductor gas sensors in environmental monitoring. In Raivo Jaaniso and Ooi Kiang Tan, editors, *Semiconductor Gas Sensors*, Woodhead Publishing Series in Electronic and Optical Materials, pages 433 – 466. Woodhead Publishing, 2013.

[2] Puligundla P. et al. Meng X., Kim S. Carbon dioxide and oxygen gas sensors-possible application for monitoring quality, freshness, and safety of agricultural and food products with emphasis on importance of analytical signals and their transformation. *Journal of the Korean Society for Applied Biological Chemistry*, 57:723–733, 2014.

[3] B. Fabbri, M. Valt, C. Parretta, S. Gherardi, A. Gaiardo, C. Malagù, F. Mantovani, V. Strati, and V. Guidi. Correlation of gaseous emissions to water stress in tomato and maize crops: From field to laboratory and back. *Sensors and Actuators B: Chemical*, 303:127227, 2020.

[4] S Ehrmann, J Jüngst, J Goschnick, and D Everhard. Application of a gas sensor microarray to human breath analysis. *Sensors and Actuators B: Chemical*, 65(1):247–249, 2000.

[5] Cesare Malagù, Barbara Fabbri, Sandro Gherardi, Alessio Giberti, Vincenzo Guidi, Nicolò Landini, and Giulia Zonta. Chemoresistive gas sensors for the detection of colorectal cancer biomarkers. *Sensors*, 14(10):18982–18992, 2014.

[6] Jane Hodgkinson and Ralph P Tatam. Optical gas sensing: a review. 24(1):012004, nov 2012.

[7] S. Zampolli, I. Elmi, F. Mancarella, P. Betti, E. Dalcanale, G.C. Cardinali, and M. Severi. Real-time monitoring of sub-ppb concentrations of aromatic volatiles with a mems-enabled miniaturized gas-chromatograph. *Sensors and Actuators B: Chemical*, 141(1):322–328, 2009.

[8] Minglei Shan, Li Xiang, Zhu Changping, and Zhang Jiahua. Gas concentration detection using ultrasonic based on wireless sensor networks. *2nd International*

*Conference on Information Science and Engineering, ICISE2010 - Proceedings*, 12 2010.

[9] Eric Bakker and Martin Telting-Diaz. Electrochemical sensors. *Analytical Chemistry*, 74(12):2781–2800, 2002. PMID: 12090665.

[10] Alvise Bagolini, Andrea Gaiardo, Michele Crivellari, Evgeny Demenev, Ruben Bartali, Antonino Picciotto, Matteo Valt, Francesco Ficorella, Vincenzo Guidi, and Pierluigi Bellutti. Development of mems mos gas sensors with cmos compatible pecvd inter-metal passivation. *Sensors and Actuators B: Chemical*, 292:225–232, 2019.

[11] Ehsan Espid and Fariborz Taghipour. Uv-led photo-activated chemical gas sensors: A review. *Critical Reviews in Solid State and Materials Sciences*, 42(5):416–432, 2017.

[12] Aditya Sharma and Chandra Sekhar Rout. Advances in understanding the gas sensing mechanisms by in situ and operando spectroscopy. *J. Mater. Chem. A*, 9:18175–18207, 2021.

[13] Giovanni Neri. First fifty years of chemoresistive gas sensors. *Chemosensors*, 3(1):1–20, 2015.

[14] Figaro usa, inc. https://www.figarosensor.com/.

[15] Sensirion. https://www.sensirion.com/en/.

[16] Simonetta Capone, Angiola Forleo, Luca Francioso, Roberto Rella, Pietro Siciliano, Jolanda Spadavecchia, D. S. Presicce, Antonella M. Taurino, and Dennis A Forleo. Solid state gas sensors: State of the art and future activities. *ChemInform*, 35, 2003.

[17] Dinesh K Aswal and Shiv K Gupta. *Science and technology of chemiresistor gas sensors*. Nova Publishers, 2007.

[18] G. Korotcenkov, I. Blinov, V. Brinzari, and J.R. Stetter. Effect of air humidity on gas response of sno2 thin film ozone sensors. *Sensors and Actuators B: Chemical*, 122(2):519–526, 2007.

[19] Shih-Wen Chiu and Kea-Tiong Tang. Towards a chemiresistive sensor-integrated electronic nose: A review. *Sensors*, 13(10):14214–14247, 2013.

[20] Andrea Gaiardo, Barbara Fabbri, Vincenzo Guidi, Pierluigi Bellutti, Alessio Giberti, Sandro Gherardi, Lia Vanzetti, Cesare Malagù, and Giulia Zonta. Metal sulfides as sensing materials for chemoresistive gas sensors. *Sensors*, 16(3), 2016.

[21] A. Gaiardo, B. Fabbri, A. Giberti, M. Valt, S. Gherardi, V. Guidi, C. Malagù, P. Bellutti, G. Pepponi, D. Casotti, G. Cruciani, G. Zonta, N. Landini, M. Barozzi, S. Morandi, L. Vanzetti, R. Canteri, M. Della Ciana, A. Migliori, and E. Demenev. Tunable formation of nanostructured sic/sioc core-shell for selective detection of $SO_2$. *Sensors and Actuators B: Chemical*, 305:127485, 2020.

[22] M Valt, B Fabbri, A Gaiardo, S Gherardi, D Casotti, G Cruciani, G Pepponi, L Vanzetti, E Iacob, C Malagù, P Bellutti, and V Guidi. Aza-crown-ether functionalized graphene oxide for gas sensing and cation trapping applications. 6(7):075603, apr 2019.

[23] Matteo Valt, Maria Caporali, Barbara Fabbri, Andrea Gaiardo, Soufiane Krik, Erica Iacob, Lia Vanzetti, Cesare Malagù, Martina Banchelli, Cristiano D'Andrea, Manuel Serrano-Ruiz, Matteo Vanni, Maurizio Peruzzini, and Vincenzo Guidi. Air stable nickel-decorated black phosphorus and its room-temperature chemiresistive gas sensor capabilities. *ACS Applied Materials & Interfaces*, 13(37):44711–44722, 2021.

[24] V. Guidi, C. Malagù, Maria Carotta, and B. Vendemiati. *Printed semiconducting gas sensors*, pages 278–334. 12 2012.

[25] D. Briand, S. Colin, J. Courbat, S. Raible, J. Kappler, and N.F. de Rooij. Integration of mox gas sensors on polyimide hotplates. *Sensors and Actuators B: Chemical*, 130(1):430 – 435, 2008. Proceedings of the Eleventh International Meeting on Chemical Sensors IMCS-11.

[26] N. Barsan, D. Koziej, and U. Weimar. Metal oxide-based gas sensor research: How to? *Sensors and Actuators B: Chemical*, 121(1):18 – 35, 2007. Special Issue: 25th Anniversary of Sensors and Actuators B: Chemical.

[27] Nicolae Barsan and Udo Weimar. Conduction model of metal oxide gas sensors. *Journal of Electroceramics*, 7(3):143–167, Dec 2001.

[28] Marc J. Madou and S. Roy Morrison. 13 - application of solid-state chemical sensors. In Marc J. Madou and S. Roy Morrison, editors, *Chemical Sensing with Solid State Devices*, pages 517 – 546. Academic Press, San Diego, 1989.

[29] Soumen Das and V. Jayaraman. Sno2: A comprehensive review on structures and gas sensors. *Progress in Materials Science*, 66:112–255, 2014.

[30] A. V. Nikam, B. L. V. Prasad, and A. A. Kulkarni. Wet chemical synthesis of metal oxide nanoparticles: a review. *CrystEngComm*, 20:5091–5107, 2018.

[31] Raivo Jaaniso and Ooi Kiang Tan. *Semiconductor gas sensors*. Elsevier, 2013.

[32] M Valt, B Fabbri, A Gaiardo, S Gherardi, D Casotti, G Cruciani, G Pepponi, L Vanzetti, E Iacob, C Malagù, P Bellutti, and V Guidi. Aza-crown-ether functionalized graphene oxide for gas sensing and cation trapping applications. *Materials Research Express*, 6(7):075603, apr 2019.

[33] Barbara H Stuart. *Infrared spectroscopy: fundamentals and applications*. John Wiley & Sons, 2004.

[34] M. Olga Guerrero-Pérez and Gregory S. Patience. Experimental methods in chemical engineering: Fourier transform infrared spectroscopy—ftir. *The Canadian Journal of Chemical Engineering*, 98(1):25–33, 2020.

[35] Janusz Ryczkowski. Ir spectroscopy in catalysis. *Catalysis Today*, 68(4):263–381, 2001. IR Spectroscopy in Catalysis.

[36] Frank C Hawthorne. *Spectroscopic methods in mineralogy and geology*, volume 18. Walter de Gruyter GmbH & Co KG, 2018.

[37] Nati Salvadó, Salvador Butí, Mark J. Tobin, Emmanuel Pantos, A. John N. W. Prag, and Trinitat Pradell. Advantages of the use of sr-ft-ir microspectroscopy: applications to cultural heritage. *Analytical Chemistry*, 77(11):3444–3451, 2005.

[38] Nelson L Alpert, William E Keiser, and Herman A Szymanski. *IR: theory and practice of infrared spectroscopy*. Springer Science & Business Media, 2012.

[39] John Michael Hollas. *Basic atomic and molecular spectroscopy*, volume 11. Royal Society of Chemistry, 2002.

[40] John Coates. Interpretation of infrared spectra, a practical approach, 2000.

[41] Robert Bell. *Introductory Fourier transform spectroscopy*. Elsevier, 2012.

[42] P Jacquinot. New developments in interference spectroscopy. 23(1):267–312, jan 1960.

[43] P. B. Fellgett. On the ultimate sensitivity and practical performance of radiation detectors. *J. Opt. Soc. Am.*, 39(11):970–976, Nov 1949.

[44] Janine Connes and Pierre Connes. Near-infrared planetary spectra by fourier spectroscopy. i. instruments and results. *J. Opt. Soc. Am.*, 56(7):896–910, Jul 1966.

[45] Donald F Swinehart. The beer-lambert law. *Journal of chemical education*, 39(7):333, 1962.

[46] Marie-Isabelle Baraton and Lhadi Merhari. Investigation of the gas detection mechanism in semiconductor chemical sensors by ftir spectroscopy. *Synthesis and Reactivity in Inorganic, Metal-Organic, and Nano-Metal Chemistry*, 35(10):733–742, 2005.

[47] Fatima-Ezahra Annanouch, Gilles Bouchet, Pierre Perrier, Nicolas Morati, Christelle Reynard-Carette, Khalifa Aguir, Virginie Martini-Laithier, and Marc Bendahan. Hydrodynamic evaluation of gas testing chamber: Simulation, experiment. *Sensors and Actuators B: Chemical*, 290:598–606, 2019.

[48] Hae-Ryong Kim, Alexander Haensch, Il-Doo Kim, Nicolae Barsan, Udo Weimar, and Jong-Heun Lee. The role of nio doping in reducing the impact of humidity on the performance of sno2-based gas sensors: Synthesis strategies, and phenomenological and spectroscopic studies. *Advanced Functional Materials*, 21(23):4456–4463, 2011.

[49] Ann-Kathrin Elger and Christian Hess. Elucidating the mechanism of working sno2 gas sensors using combined operando uv/vis, raman, and ir spectroscopy. *Angewandte Chemie International Edition*, 58(42):15057–15061, 2019.

[50] Peirong Chen, Simon Schönebaum, Thomas Simons, Dieter Rauch, Markus Dietrich, Ralf Moos, and Ulrich Simon. Correlating the integral sensing properties of zeolites with molecular processes by combining broadband impedance and drift spectroscopy—a new approach for bridging the scales. *Sensors*, 15(11):28915–28941, 2015.

[51] Roman G. Pavelko, Joong-Ki Choi, Atsushi Urakawa, Masayoshi Yuasa, Tetsuya Kida, and Kengo Shimanoe. H2o/d2o exchange on sno2 materials in the presence of co: Operando spectroscopic and electric resistance measurements. *The Journal of Physical Chemistry C*, 118(5):2554–2563, 2014.

[52] R Byron Bird, Warren E Stewart, and Edwin N Lightfoot. *Transport phenomena*, volume 1. John Wiley & Sons, 2006.

[53] Salvador García-Muñoz, Adam Butterbaugh, Ian Leavesley, Leo Francis Manley, David Slade, and Sean Bermingham. A flowsheet model for the development of a continuous process for pharmaceutical tablets: An industrial perspective. *AIChE Journal*, 64(2):511–525, 2018.

[54] Octave Levenspiel. *Chemical reaction engineering*. John wiley & sons, 1998.

[55] Matteo Valt, Michele Della Ciana, Barbara Fabbri, Diego Sali, Andrea Gaiardo, and Vincenzo Guidi. Design and validation of a novel operando spectroscopy reaction chamber for chemoresistive gas sensors. *Sensors and Actuators B: Chemical*, 341:130012, 2021.

[56] Meti Megayanti, Camellia Panatarani, and I Made Joni. Development of microheaters for gas sensor with an at-mega 8535 temperature controller using a pwm (pulse width modulation) method. In *AIP Conference Proceedings*, volume 1719, page 030046. AIP Publishing LLC, 2016.

[57] Tzu-Sen Yang and Jin-Chern Chiou. A high-efficiency driver circuit for a gas-sensor microheater based on a switch-mode dc-to-dc converter. *Sensors*, 20(18), 2020.

[58] P. P. Capra, F. Galliana, M. Latino, A. Bonavita, N. Donato, and G. Neri. A high-resistance measurement setup for mox sensing materials characterization. In Corrado Di Natale, Vittorio Ferrari, Andrea Ponzoni, Giorgio Sberveglieri, and Marco Ferrari, editors, *Sensors and Microsystems*, pages 149–154, Cham, 2014. Springer International Publishing.

[59] J Kneer, A Eberhardt, P Walden, A Ortiz Pérez, J Wöllenstein, and S Palzer. Apparatus to characterize gas sensor response under real-world conditions in the lab. *The Review of scientific instruments*, 85(5):055006, May 2014.

[60] Jun-gu Kang, Joon-Shik Park, Kwang-Bum Park, Junho Shin, Eung-An Lee, Sang-soo Noh, and Hoo-Jeong Lee. Temperature control of micro heater using pt thin film temperature sensor embedded in micro gas sensor. *Micro and Nano Systems Letters*, 5(1):26, Sep 2017.

[61] M. S. Van Dusen. Platinum-resistance thermometry at low temperatures. *Journal of the American Chemical Society*, 47(2):326–332, 1925.

[62] Makoto Egashira, Yasuhiro Shimizu, Yuji Takao, and Shuichi Sako. Variations in i–v characteristics of oxide semiconductors induced by oxidizing gases. *Sensors and Actuators B: Chemical*, 35(1):62–67, 1996. Proceedings of the Sixth International Meeting on Chemical Sensors.

[63] S. A. Pianaro, P. R. Bueno, P. Olivi, E. Longo, and J. A. Varela. Electrical properties of the $SnO_2$-based varistor. *Journal of Materials Science: Materials in Electronics*, 9(2):159–165, Mar 1998.

[64] Patrycja Suchorska-Woźniak, Olga Rac, Marta Fiedot, and Helena Teterycz. Analysis of $SnO_2$—$W_O3$ heterocontact properties during the detection of hydrogen sulphide. *Sensors (Basel, Switzerland)*, 14(11):20480–20499, Oct 2014.

[65] Bart Van Zeghbroeck. *Principles of semiconductor devices*, volume 34. 2004.

[66] Susanne Wicker, Mathilde Guiltat, Udo Weimar, Anne Hémeryck, and Nicolae Barsan. Ambient humidity influence on co detection with $SnO_2$ gas sensing materials. a combined drifts/dft investigation. *The Journal of Physical Chemistry C*, 121(45):25064–25073, 2017.

[67] Andrea Gaiardo, Barbara Fabbri, Vincenzo Guidi, Pierluigi Bellutti, Alessio Giberti, Sandro Gherardi, Lia Vanzetti, Cesare Malagù, and Giulia Zonta. Metal sulfides as sensing materials for chemoresistive gas sensors. *Sensors*, 16(3), 2016.

[68] R Einzinger. Metal oxide varistors. *Annual Review of Materials Science*, 17(1):299–321, 1987.

[69] F. Schipani, C. M. Aldao, and M. A. Ponce. Schottky barriers measurements through arrhenius plots in gas sensors based on semiconductor films. *AIP Advances*, 2(3):032138, 2012.

[70] Tanya L. Myers, Carolyn S. Brauer, Yin-Fong Su, Thomas A. Blake, Russell G. Tonkyn, Alyssa B. Ertel, Timothy J. Johnson, and Robert L. Richardson. Quantitative reflectance spectra of solid powders as a function of particle size. *Appl. Opt.*, 54(15):4863–4875, May 2015.

[71] R Alcaraz de la Osa, I Iparragirre, D Ortiz, and JM Saiz. The extended kubelka-munk theory and its application to spectroscopy. *ChemTexts*, 6(1):1–14, 2020.

[72] Yong Yang, R. S. Disselkamp, J. Szanyi, C. H. F. Peden, C. T. Campbell, and J. G. Goodwin. Design and operating characteristics of a transient kinetic analysis catalysis reactor system employing in situ transmission fourier transform infrared. *Review of Scientific Instruments*, 77(9):094104, 2006.

[73] Bhagyesha S. Patil, Priya D. Srinivasan, Ed Atchison, Hongda Zhu, and Juan J. Bravo-Suárez. Design, modelling, and application of a low void-volume in situ diffuse reflectance spectroscopic reaction cell for transient catalytic studies. *React. Chem. Eng.*, 4:667–678, 2019.

[74] Katharina Grossmann, Roman G. Pavelko, Nicolae Barsan, and Udo Weimar. Interplay of h2, water vapor and oxygenat the surface of sno2 based gas sensors – an operando investigation utilizing deuterated gases. *Sensors and Actuators B: Chemical*, 166-167:787–793, 2012.

[75] Roman G. Pavelko, Helen Daly, Michael Hübner, Christopher Hardacre, and Eduard Llobet. Time-resolved drifts, ms, and resistance study of sno2 materials: The role of surface hydroxyl groups in formation of donor states. *The Journal of Physical Chemistry C*, 117(8):4158–4167, 2013.

[76] David Degler, Susanne Wicker, Udo Weimar, and Nicolae Barsan. Identifying the active oxygen species in sno2 based gas sensing materials: An operando ir spectrsocopy study. *The Journal of Physical Chemistry C*, 119(21):11792–11799, 2015.

[77] Matthias Batzill and Ulrike Diebold. The surface and materials science of tin oxide. *Progress in Surface Science*, 79(2):47–154, 2005.

[78] V. Guidi, M.C. Carotta, B. Fabbri, S. Gherardi, A. Giberti, and C. Malagù. Array of sensors for detection of gaseous malodors in organic decomposition products. *Sensors and Actuators B: Chemical*, 174:349 – 354, 2012.

[79] Andrea Gaiardo, Giulia Zonta, Sandro Gherardi, Cesare Malagù, Barbara Fabbri, Matteo Valt, Lia Vanzetti, Nicolò Landini, Davide Casotti, Giuseppe Cruciani, Michele Della Ciana, and Vincenzo Guidi. Nanostructured smfeo3 gas sensors: Investigation of the gas sensing performance reproducibility for colorectal cancer screening. *Sensors*, 20(20), 2020.

[80] Andrzej Bieganowski, Katarzyna Jaromin-Glen, UKASZ Guz, Grzegorz Lagod, Grzegorz Jozefaciuk, Wojciech Franus, Zbigniew Suchorab, and Henryk Sobczuk. Evaluating soil moisture status using an e-nose. *Sensors*, 16:886, 2016.

[81] Marc J. Madou and S. Roy Morrison. 12 - gas sensors based on semiconductor powders. In Marc J. Madou and S. Roy Morrison, editors, *Chemical Sensing with Solid State Devices*, pages 479 – 516. Academic Press, San Diego, 1989.

[82] Gerhard Gschwandtner, Karin Gschwandtner, Kevin Eldridge, Charles Mann, and David Mobley. Historic emissions of sulfur and nitrogen oxides in the united states from 1900 to 1980. *Journal of the Air Pollution Control Association*, 36(2):139–149, 1986.

[83] Z Klimont, S J Smith, and J Cofala. The last decade of global anthropogenic sulfur dioxide: 2000–2011 emissions. 8(1):014003, jan 2013.

[84] European Chemical Agency. https://echa.europa.eu/it/registration-dossier/-/registered-dossier/15352/7/11/1.

[85] Nicolas Theys, Pascal Hedelt, Isabelle De Smedt, Christophe Lerot, Huan Yu, Jonas Vlietinck, Mattia Pedergnana, Santiago Arellano, B Galle, D Fernandez, et al. Global monitoring of volcanic so 2 degassing with unprecedented resolution from tropomi onboard sentinel-5 precursor. *Scientific reports*, 9(1):1–10, 2019.

[86] Mohammad Ghanbari Ghozikali, Behzad Heibati, Kazem Naddafi, Itai Kloog, Gea Oliveri Conti, Riccardo Polosa, and Margherita Ferrante. Evaluation of chronic obstructive pulmonary disease (copd) attributed to atmospheric o3, no2, and so2 using air q model (2011–2012 year). *Environmental Research*, 144:99–105, 2016.

[87] A. Gaiardo, P. Bellutti, B. Fabbri, S. Gherardi, A. Giberti, V. Guidi, N. Landini, C. Malagù, G. Pepponi, M. Valt, and G. Zonta. Chemoresistive gas sensor based on

sic thick film: Possible distinctive sensing properties between h2s and so2. *Procedia Engineering*, 168:276–279, 2016. Proceedings of the 30th anniversary Eurosensors Conference – Eurosensors 2016, 4-7. Sepember 2016, Budapest, Hungary.

[88] PlasmaChem. http://www.plasmachem.com/shop/en/172-sic-nanopowder-207-n.

[89] Bologna IMM-CNR. https://www.bo.imm.cnr.it/unit/articles/structural-characterization-facilities.

[90] M. Della Ciana, M. Valt, B. Fabbri, P. Bernardoni, V. Guidi, and V. Morandi. Development of a dedicated instrumentation for electrical and thermal characterization of chemiresistive gas sensors. *Review of Scientific Instruments*, 92(7):074702, 2021.

[91] Nicolas Biscay, Lucile Henry, Tadafumi Adschiri, Masahiro Yoshimura, and Cyril Aymonier. Behavior of silicon carbide materials under dry to hydrothermal conditions. *Nanomaterials*, 11(5), 2021.

[92] JOHN A. COSTELLO and RICHARD E. TRESSLER. Oxidation kinetics of silicon carbide crystals and ceramics: I, in dry oxygen. *Journal of the American Ceramic Society*, 69(9):674–681, 1986.

[93] B. E. Deal and A. S. Grove. General relationship for the thermal oxidation of silicon. *Journal of Applied Physics*, 36(12):3770–3778, 1965.

[94] Teresa Oh. Comparison between sioc thin film by plasma enhance chemical vapor deposition and sio2 thin film by fourier transform infrared spectroscopy. *Journal of The Korean Physical Society - J KOREAN PHYS SOC*, 56, 04 2010.

[95] Marta Klanjšek Gunde. Vibrational modes in amorphous silicon dioxide. *Physica B: Condensed Matter*, 292(3):286–295, 2000.

[96] NIST. https://webbook.nist.gov/cgi/cbook.cgi?ID=C124389&Type=IR-SPEC&Index=1.

[97] James Hunter Anderson and George A. Parks. Electrical conductivity of silica gel in the presence of adsorbed water. *The Journal of Physical Chemistry*, 72(10):3662–3668, 1968.

[98] Masayuki Nogami, Ritsuko Nagao, and Cong Wong. Proton conduction in porous silica glasses with high water content. *The Journal of Physical Chemistry B*, 102(30):5772–5775, 1998.

[99] L.T. Zhuravlev. The surface chemistry of amorphous silica. zhuravlev model. *Colloids and Surfaces A: Physicochemical and Engineering Aspects*, 173(1):1–38, 2000.

[100] Noam Agmon. The grotthuss mechanism. *Chemical Physics Letters*, 244(5):456–462, 1995.

[101] Sachini Wickramasinghe, Truong Do, and Phuong Tran. Fdm-based 3d printing of polymer and associated composite: A review on mechanical properties, defects and treatments. *Polymers*, 12(7), 2020.

[102] Marek Pagac, Jiri Hajnys, Quoc-Phu Ma, Lukas Jancar, Jan Jansa, Petr Stefek, and Jakub Mesicek. A review of vat photopolymerization technology: Materials, applications, challenges, and future trends of 3d printing. *Polymers*, 13(4), 2021.

[103] Ruben Bayu Kristiawan, Fitrian Imaduddin, Dody Ariawan, Ubaidillah, and Zainal Arifin. A review on the fused deposition modeling (fdm) 3d printing: Filament processing, materials, and printing parameters. *Open Engineering*, 11(1):639–649, 2021.

[104] B. Fabbri, A. Gaiardo, A. Giberti, V. Guidi, C. Malagù, A. Martucci, M. Sturaro, G. Zonta, S. Gherardi, and P. Bernardoni. Chemoresistive properties of photo-activated thin and thick zno films. *Sensors and Actuators B: Chemical*, 222:1251–1256, 2016.